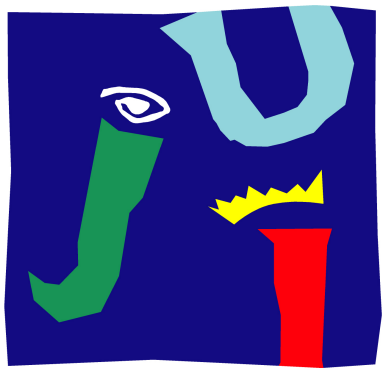

UNIVERSITAT JAUME·I

Single-pixel Computational Imaging: Application to Fluorescence and Diffuse Optical Imaging

Armin Johannes Maxemilian Lenz

Advisors:
Enrique Tajahuerce Romera
&
Vicent Climent Jordà

January, 2024

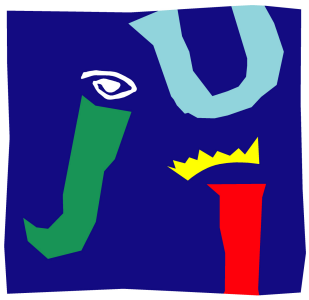

UNIVERSITAT JAUME·I

Programa de Doctorado en Ciencias

Escuela de Doctorado de la Universitat Jaume I

Single-pixel Computational Imaging: Application to Fluorescence and Diffuse Optical Imaging

Memoria presentada por Armin Johannes Maxemilian Lenz para optar al grado de doctor por la Universitat Jaume I

Escrita y realizada por:
Armin Johannes Maxemilian Lenz

Dirigida por:
Enrique Tajahuerce Romera
Vicent Climent Jordà

Castellón de la Plana, 15 de enero de 2024

El autor y los directores agradecen un contrato predoctoral ACIF/2019/019 financiado por la Generalitat Valenciana y el Fondo Social Europeo (FSE), así como una subvención para realizar estancias en centros de investigación BEFPI/2021/046 financiada por la Generalitat Valenciana. También agradecen la ayuda recibida a través del proyecto PID2019-110927RB-I00, financiado por el Ministerio de Ciencia e Innovación y la Agencia Estatal de Investigación (MCIN/AEI/10.13039/501100011033), y los proyectos PROMETEO/2020/029 y MFA/2022/055 financiados por la Generalitat Valenciana.

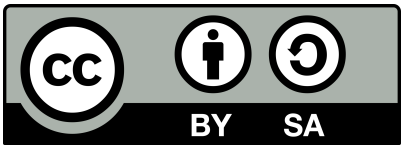

Técnicas de imagen computacional con un solo píxel: aplicación en imagen de fluorescencia e imagen con luz difusa

de

Armin Johannes Maxemilian Lenz

Doctor en Ciencias por la Escuela de Doctorado en Ciencias
Escola Superior de Tecnologia i Ciències Experimentals, ESTCE
Universitat Jaume I

Resumen

En las últimas décadas, la imagen computacional ha surgido como un nuevo paradigma para superar los límites de los sistemas de imagen tradicionales. Este enfoque implica el diseño integrado de hardware y software, en concreto la óptica y el procesamiento de señales posterior a la detección. Y muy recientemente, la cámara de un solo píxel ha ganado una atención significativa entre las técnicas de imagen computacional. La capacidad de utilizar detectores especializados sin resolución espacial y moduladores espaciales de luz rápidos permite obtener imágenes en rangos espectrales exóticos y en condiciones de poca luz, así como construir sistemas de imagen multidimensionales compactos y eficientes.

En esta tesis, demostramos el uso de la cámara de un solo píxel en dos modalidades de imagen, la imagen de fluorescencia resuelta en el tiempo y la imagen óptica difusa, técnicas cruciales en aplicaciones biomédicas que permiten la adquisición no invasiva de información funcional y estructural.

En el ámbito de la imagen de fluorescencia, aplicamos una novedosa técnica basada en fusionado de datos para adquirir hipercubos 4D de varios gigavóxeles midiendo sólo una fracción muy pequeña del conjunto de datos. Los sistemas propuestos combinan cámaras convencionales con cámaras de un solo píxel multiespectrales y de resolución temporal, y se emplea la fusión de datos para combinar las proyecciones 2D y 3D (o incluso 4D de baja resolución espacial) generadas por cada cámara individual en un hipercubo 4D de alta resolución. Este marco se aplica tanto a un sistema óptico de imagen de objetos macroscópicos como a la microscopía e incluso a la imagen de tiempo de vida de fluorescencia.

Por otro lado, una parte de la investigación realizada en esta tesis se centra en el desarrollo de novedosas técnicas de imagen difusa. Los sistemas propuestos utilizan técnicas de imagen de un solo píxel, lo que permite esquemas de detección simplificados utilizando esferas integradoras como detectores, permitiendo la obtención de imágenes de las propiedades de absorción y dispersión de medios turbios. Se proponen dos sistemas, uno que utiliza una configuración experimental con dos esferas integradoras para obtener imágenes de las propiedades ópticas mediante el modelo Kubelka-Munk, y otro que utiliza un sistema de obtención de imágenes espaciales en el dominio de frecuencias espaciales basado en una cámara de un solo píxel y con iluminación estructurada para caracterizar medios turbios en geometría de reflexión.

Single-pixel Computational Imaging: Application to Fluorescence and Diffuse Optical Imaging

by

Armin Johannes Maxemilian Lenz

Doctor of Philosophy by the Science Doctoral School
Escola Superior de Tecnologia i Ciències Experimentals, ESTCE
Universitat Jaume I

Abstract

In recent decades, computational imaging has emerged as a new paradigm for improving and surpassing the limits of traditional imaging systems. This approach involves the integrated design of hardware and software, specifically the optics and post-detection signal processing. Very recently, the single-pixel camera has gained significant attention among computational imaging techniques. The ability to use specialized detectors without spatial resolution and fast spatial light modulators enables imaging in novel spectral ranges and low light conditions, as well as building compact and efficient multidimensional imaging systems.

In this dissertation, we demonstrate the use of single-pixel imaging methods in two imaging modalities, time-resolved fluorescence imaging and diffuse optical imaging, crucial techniques in biomedical applications that enable the non-invasive acquisition of functional and structural information.

In fluorescence imaging we introduce a novel method based on data fusion techniques to acquire giga-voxel 4D hypercubes by measuring only a very small fraction of the dataset. The proposed systems combine conventional cameras with multispectral and time-resolved single-pixel cameras, and data fusion is employed to merge the 2D and 3D (or even low spatial resolution 4D) projections generated by each individual camera into a high-resolution 4D hypercube. This framework is applied to macroscopic imaging as well as microscopy and even fluorescence lifetime imaging.

The second part of this thesis focuses on developing novel methods for performing diffuse optical imaging. The suggested systems utilize single-pixel imaging techniques, which allows for simplified detection schemes utilizing integrating spheres as bucket detectors, enabling the retrieval of images of the absorption and scattering properties of turbid media. Two systems are discussed, one utilizing a double integrating sphere setup to image optical properties via the Kubelka-Munk light transport model, and another utilizing a structured illumination single-pixel spatial frequency domain imaging system to characterize turbid media in reflection geometry.

Contents

Chapter 1

Introduction

Imaging systems allow us to observe, measure and understand the world. In the beginning, we used our eyes to observe the world around us. However, our sight is limited in both range and detail, as we neither can see very far, nor very small objects. To overcome these limitations, humanity started to use optical instruments. In the late 16th and early 17th century, the first optical microscopes and telescopes were built. They consisted of simple combinations of lenses, and allowed us to study both small and distant objects. Whereas the microscope has been a key device for the development of life sciences, telescopes laid the foundation for modern astronomy. However, it was not until the development of photography that these instruments ceased to rely on human vision. In early photography, images were captured by exposing light-sensitive film and paper, which was processed in liquid chemical solutions to develop and stabilize the photograph. This had the disadvantage of limited and expensive editing (post-processing) of film-based images after capture.

Nowadays, the use of digital image sensors replaced the use of photosensitive films to record images. This allowed for an easy post-processing of images, and to make imaging systems faster, cheaper, and smaller. However, digital cameras still suffer from traditional imaging limitations and trade-offs, such as only measuring the light intensity distribution, the necessity of the lenses to form a good quality image, and bottlenecks in data acquisition speed, storage and transmission.

To gather more information for cutting edge applications in modern industry and science, imaging systems started to manipulate the way this information was encoded onto the sensor. This idea of indirectly encoding the information and afterwards computationally decoding it gave raise to the paradigm of computational imaging [1, 2]. In a nutshell, computational imaging is the co-design of hardware and software to improve and overcome the traditional or native limits of imaging systems. By designing algorithms in conjunction with the optics, we can encode the most useful information for a specific task and then use clever algorithms to extract the desired information from our measurements. While traditional cameras are direct imagers (i.e. the image recorded is very close to the desired image and little to no post-processing is required), a computational camera uses hardware to encode information about the imaged scene into the measurements, and usually the measured data has little resemblance to the image reconstructed with computational

algorithms.

The paradigm shift of computational imaging has led to many advances and techniques, such as super-resolution microscopy (e.g., Fourier ptychography [3, 4], structured illumination microscopy (SIM) [5], stimulated emission depletion (STED) microscopy [6], etc.), multidimensional imaging (including phase imaging [7], multispectral imaging [8–10], polarization imaging [11], temporal information [12], and light-field, 3D and tomography [13–16]), imaging through turbid media [17–20], non-line-of-sight imaging [21], and lensless imaging [22–24].

An important challenge of computational imaging is the inverse problem, i.e. how to reconstruct the unknown image from our encoded measurement. Often, the encoding performed by computational cameras is not invertible, and the problem of recovering the image may be ill-posed or underdetermined, posing the challenge of finding a unique solution. Typically, these image inverse problems are solved using optimization techniques that minimize a data fidelity term and a term based on prior knowledge about the image to enforce the uniqueness of the solution.

The single-pixel camera (SPC) is one such computational imaging device that can provide a competitive advantage over conventional cameras in some scenarios [25,26]. Single-pixel imaging (SPI) is characterized by the use of detectors without spatial information (i.e., detectors with only one pixel, also called bucket detectors). To obtain spatial information, typical SPCs use spatial light modulators (SLMs) to generate structured light patterns that are projected onto the scene. The light coming from the scene is then measured by the bucket detector. Finally, the image is computationally reconstructed from this measured signal by solving the corresponding inverse problem.

It is precisely in the simplicity of the detector that the strength of the SPI technique lies. This single-pixel detector may provide improved performance, such as a better efficiency, lower dark count, or faster timing response; or it can allow the use of specialized detectors to build cameras sensitive to spectral, temporal, polarization, 3D, or phase information. In addition, the SPC is able to compress data directly at the acquisition step (known as compressive sensing, CS) to reduce data storage and transfer requirements.

1.1 Contribution

The SPC and inverse problems are the core of all contributions in this dissertation. These techniques were applied to two distinct imaging modalities.

On one hand, time-resolved multispectral fluorescence imaging has been performed. SPCs can be easily specialized to obtain multidimensional images, such as multispectral or time-resolved images, but they usually suffer from low spatial resolution, whereas traditional cameras provide high-resolution images, but normally lack the sensitivity to that extra dimensions. In this contribution, multispectral and time-resolved SPCs are merged with a conventional camera in order to obtain high spatial resolution, time-resolved and multispectral images of fluorescence. The merging of the different cameras is performed with a data fusion (DF) algorithm formulated as an inverse problem.

On the other hand, the SPC architecture has been applied to diffuse optical imaging (DOI). The goal of DOI is to generate spatial maps or images of the distribution of optical properties, namely absorption and scattering, of turbid media. DOI techniques themselves can be classified as computational imaging, since these techniques require the use of sophisticated hardware to interrogate the sample, and images of the optical properties are recovered using inversion methods that incorporate not only the measurements but also models of light propagation in turbid media.

By applying the SPI technique we were able to develop new simpler imaging systems by using integrating spheres (which integrate diffuse reflected or transmitted light) as bucket detectors instead of pixelated sensors. One of the developed systems makes use of a simple light propagation model (the Kubelka-Munk mode), which originally does not allow for a spatially resolved characterization because the model is not transversal spatially resolved, and due to the experimental requirements of using integrating spheres to measure total diffuse reflected and transmitted light. But imaging capabilities were enabled by using SPI techniques. The second developed system is implemented in reflection geometry only, and measurements are performed by interrogating the sample in the spatial frequency domain (imaging in this domain is referred to as spatial frequency domain imaging, or SFDI) by projecting sinusoidal light patterns onto the sample. Usually these SFDI systems use conventional cameras, but once again the SPI technique is used to dispense of the pixelated sensor.

1.2 Publications

The results of the work related to this dissertation have been presented to the scientific community through several publications in scientific journals and conferences. Below is a list of the main results:

- Journals
  - A. J. M. Lenz, P. Clemente, V. Climent, J. Lancis, and E. Tajahuerce, "Imaging the optical properties of turbid media with single-pixel detection based on the Kubelka–Munk model," Opt. Lett. 44, 4797-4800 (2019). https://doi.org/10.1364/OL.44.004797
  - F. Soldevila, A. J. M. Lenz, A. Ghezzi, A. Farina, C. D'Andrea, and E. Tajahuerce, "Giga-voxel multidimensional fluorescence imaging combining single-pixel detection and data fusion," Opt. Lett. 46, 4312-4315 (2021). https://doi.org/10.1364/OL.434127
  - A. Ghezzi, A. J. M. Lenz, F. Soldevila, E. Tajahuerce, V. Vurro, A. Bassi, G. Valentini, A. Farina, C. D'Andrea, "Computational based time-resolved multispectral fluorescence microscopy," APL Photonics 8 (4), 046110 (2023). https://doi.org/10.1063/5.0135452
- International conferences
  - A. J. M. Lenz, K. Arao, Y. Jauregui-Sánchez, P. Clemente, V. Climent, J. Lancis, and E. Tajahuerce, "Imaging of the optical properties of turbid media with integrated detection based on the Kubelka-Munk

model", Proc. SPIE 11074, Diffuse Optical Spectroscopy and Imaging VII, 110741Z (11 July 2019). https://doi.org/10.1117/12.2526731

– A. J. M. Lenz, P. Clemente, V. Climent, J. Lancis, and E. Tajahuerce, "Imaging the optical properties of turbid media with single-pixel detection", Proc. SPIE 11351, Unconventional Optical Imaging II, 1135109 (30 March 2020). https://doi.org/10.1117/12.2554561

– A. J. M. Lenz, P. Clemente, V. Climent, J. Lancis, and E. Tajahuerce, "Single-pixel spatial frequency domain imaging with integrating detection," in European Conferences on Biomedical Optics 2021 (ECBO), OSA Technical Digest (Optica Publishing Group, 2021), paper ES2B.3.

– F. Soldevila, A. J. M. Lenz, A. Ghezzi, A. Farina, C. D'Andrea, and E. Tajahuerce, "Multispectral Time-Resolved Fluorescence Imaging by Single-Pixel Detection and Data Fusion," in European Conferences on Biomedical Optics 2021 (ECBO), OSA Technical Digest (Optica Publishing Group, 2021), paper ETh3B.3.

– A. J. M. Lenz, P. Clemente, V. Climent, J. Lancis, and E. Tajahuerce, "Spatial frequency domain imaging with a bucket detector," in OSA Imaging and Applied Optics Congress 2021 (3D, COSI, DH, ISA, pcAOP), OSA Technical Digest (Optica Publishing Group, 2021), paper ITh1B.5. https://doi.org/10.1364/ISA.2021.ITh1B.5

– F. Soldevila, A. J. M. Lenz, A. Ghezzi, A. Farina, C. D'Andrea, and E. Tajahuerce, "Multispectral Fluorescence Lifetime Imaging with Single-Pixel Cameras and Data Fusion," in OSA Imaging and Applied Optics Congress 2021 (3D, COSI, DH, ISA, pcAOP), OSA Technical Digest (Optica Publishing Group, 2021), paper CTu4B.7. https://doi.org/10.1364/COSI.2021.CTu4B.7

– A. J. M. Lenz, P. Clemente, V. Climent, J. Lancis, and E. Tajahuerce, "Spatial frequency domain imaging with a bucket detector", Proc. SPIE 12147, Tissue Optics and Photonics II, 121470A (19 May 2022). https://doi.org/10.1117/12.2622116

– A. J. M. Lenz, F. Soldevila, A. Ghezzi, A. Farina, C. D'Andrea, and E. Tajahuerce, "Giga-voxel multispectral time-resolved imaging with single-pixel detection and data fusion", Proc. SPIE 12136, Unconventional Optical Imaging III, 121360D (20 May 2022). https://doi.org/10.1117/12.2621587

– A. J. M. Lenz, F. Soldevila, A. Ghezzi, A. Farina, C. D'Andrea, and E. Tajahuerce, "Multispectral Fluorescence Lifetime Imaging with Single-Pixel Cameras and Data Fusion", Iberic Meeting of Optics Students 2022 (14 June 2022).

– A. J. M. Lenz, F. Soldevila, A. Ghezzi, A. Farina, C. D'Andrea, and E. Tajahuerce, "Multispectral time-resolved fluorescence imaging with single-pixel cameras and data fusion", 25th Congress of the International Commission for optics (ICO) and 16th International Conference on Optics Within Life Sciences (OWLS) (8 September 2022).

  - E. Ipus , A. J. M. Lenz, J. Lancis, A. M. Paniagua-Diaz, P. Artal, and E. Tajahuerce "Single-pixel imaging through turbid media by combining a programmable light source and a DMD", Proc. SPIE 12435, Emerging Digital Micromirror Device Based Systems and Applications XV, 1243505 (15 March 2023). https://doi.org/10.1117/12.2650452

- National conferences
  - A. J. M. Lenz, Er. Ipus, L. Martínez-León, P. Clemente, V. Climent, J. Lancis, and E. Tajahuerce, "Spatial frequency domain imaging with a bucket detector", XIII Reunión Nacional de Óptica (22 November 2021).
  - A. J. M. Lenz, F. Soldevila, A. Ghezzi, A. Farina, C. D'Andrea, and E. Tajahuerce, "Giga-voxel multidimensional imaging by single-pixel detection and data fusion", XIII Reunión Nacional de Óptica (22-23 November 2021).
  - A. J. M. Lenz, "Multidimensional computational imaging with single-pixel detection and data fusion", Reunión Fibras Ópticas y Procesado de Señal 2022 (2 December 2022).

1.3 Outline

The remainder of this dissertation is organized in the following chapters:

Chapter 2: Computational imaging. In this chapter, we introduce a general formulation of computational imaging, and we also discuss different ways to solve imaging inverse problems. Also in this chapter we cover the concept of single-pixel imaging, compressive sensing and data fusion.

Chapter 3: Time-resolved multispectral imaging for fluorescence imaging. This chapter provides a background to fluorescence and fluorescence imaging. Next, we present several works related to multispectral time-resolved fluorescence imaging and microscopy, and fluorescence lifetime imaging; by merging information from SPCs and a conventional camera by using DF.

Chapter 4: Imaging of scattering and absorption. This chapter provides a background to the theory of light propagation in turbid media, including the KM model, the radiative transport theory, the diffusion theory and the Monte-Carlo model. Next we discuss the topic of imaging through the turbid media and imaging the optical properties of turbid media (refereed to as DOI), with a special emphasis on the SFDI technique. Lastly, we present the two developed single-pixel DOI systems, one based on the KM model and the second on the SFDI technique.

Chapter 5: Conclusions. This chapter discusses the themes presented throughout this dissertation and outlines several future directions.

Chapter 2

Computational imaging

This chapter provides a practical background of computational imaging and solving inverse problems. It does not intend to be mathematically rigorous, but rather a practical overview of the different methods and algorithms. Therefore, part of the bibliography cited in this chapter does not come from scientific articles published in scientific journals, but from blog posts, lecture notes, online forums and Q&A sites. In this chapter we will also introduce a special type of computational camera, the single-pixel camera, and discuss the theory of compressive sensing and the framework of data fusion.

2.1 Imaging as an inverse problem

First of all, we have to define how information is recorded by the imaging sensor. This is the so-called forward model of the imaging system or camera, and models the behavior of the optical system (optics, filters, sensor, modulators, etc). The forward model of the imaging system basically describes the measurement process, that is, how information about the image to be reconstructed, $\mathbf{x}$, is encoded into the measurements, $\mathbf{y}$. Namely,

$$\mathbf{y} = \mathcal{A}(\mathbf{x}) + \epsilon, \tag{2.1}$$

where $\mathcal{A}$ represents the forward model operator and ϵ is the noise present in the measurement process. This forward operator includes all operations applied to $\mathbf{x}$, such as any geometric transformation, blurring, downsampling, etc. Here, even if this forward model is a continuous process, it is represented by a discrete approximation, and so are the measurement and the image. In the notation used here bold face variables represent a discretized and vectorized version of the corresponding signal.

In many cases, the forward model is linear, and hence can be described as a linear system of equations, where the measurement is the result of a matrix-vector multiplication of the measurement matrix, $\mathbf{A}$, and the image:

$$\mathbf{y} = \mathbf{A}\mathbf{x} + \epsilon. \tag{2.2}$$

In a conventional camera, where a perfect lens or a set of lenses (with a delta PSF) projects an image of the scene onto the imaging sensor, the measurement matrix becomes the identity operator, $\mathbf{A} = \mathbf{I}$. And in the ideal case of absence of noise the measurement is directly the image, $\mathbf{y} = \mathbf{x}$ (see Fig. 2.1a). Therefore, no further computation is needed for recovering the image.

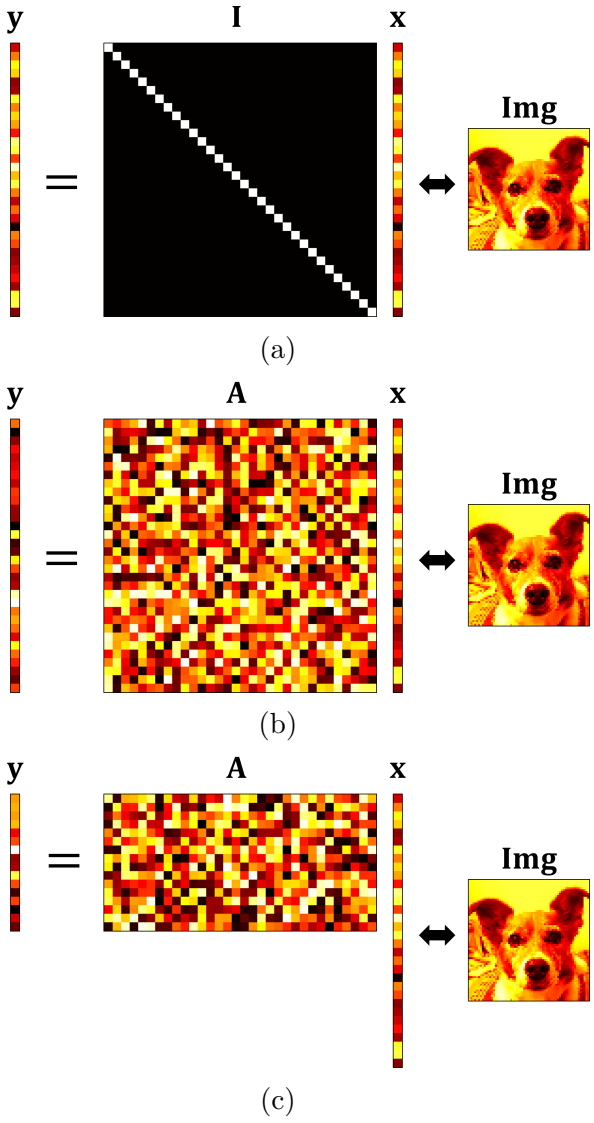

Figure 2.1: Measurement process of an imaging system with (a) identity measurement matrix, the measurement is the image, (b) square and invertible measurement matrix corresponding to a determined imaging process, and (c) non-square measurement matrix describing an underdetermined imaging process. Note that the 2D images are commonly represented as 1D arrays in digital image processing.

For this idealized camera in the presence of noise, the forward model yields: $\mathbf{y} = \mathbf{x} + \epsilon$. In this case, the image is corrupted by noise. The process of removing the noise in order to extract the image is the well-known problem of image denoising [27, 28]. There is controversy over whether this should be considered computational imaging. One argument in favor of this classification is the need of computation. On the contrary, one may argue that image denoising falls into the category of image (post-detection) processing or restoration because the goal is to process already

human-recognizable images to improve the insufficient quality; while the aim of computational imaging is to reconstruct human-recognizable images from measured data which not necessarily is human-recognizable (a discussion about this can be found in the blog entry from Ref. [29]). In any case, it is not my objective to define a criterion to define whether a technique should be considered computational imaging or not.

In the general case, where the measurement matrix is not the identity operator, the naive approach to solve the inverse problem, retrieving $\mathbf{x}$ from $\mathbf{y}$, would be to attempt to invert the measurement matrix $\mathbf{A}$ to find:

$$\hat{\mathbf{x}} = \mathbf{A}^{-1}\mathbf{y}. \tag{2.3}$$

This may be possible in some cases where $\mathbf{A}$ represents a square and invertible matrix corresponding to a determined and well-posed problem and with low noise, like in Fig. 2.1b. Unfortunately, this often does not work very well because of two possible reasons. On one hand, for relatively large images the size of the $\mathbf{A}$ matrix makes the matrix inversion unfeasible due to the extreme computational cost. The solution to this problem is rather simple: instead of explicitly calculating the $\mathbf{A}$ matrix, we can implicitly define the operations associated with $\mathbf{A}$[1]. On the other hand, frequently we acquire an undersampled measurement, or we aim to extract additional information from our measurement, e.g. such as extra dimensional information from an encoded lower dimensional measurement. This measurement process entails a dimension reduction, given that the size of our measurement vector, $\mathbf{y}$, is lower than the size of the image, $\mathbf{x}$. In this case, we must solve an underdetermined system in which the number of unknowns, elements of $\mathbf{x}$, is greater than the number of measurements. This results in a non-square $\mathbf{A}$ matrix, with less rows than columns (see Fig. 2.1c), which cannot be simply inverted. The problem now is ill-posed since there are infinite possible solutions for the underdetermined system. To solve it we need additional constraints.

To solve ill-posed or underdetermined inverse problems in imaging, often an optimization problem of the following form is formulated:

$$\hat{\mathbf{x}} = \arg\min \mathcal{D}(\mathbf{x};\mathbf{y}) + \alpha\mathcal{P}(\mathbf{x}), \tag{2.4}$$

where $\mathcal{D}(\mathbf{x};\mathbf{y})$ is the data fidelity term, $\mathcal{P}(\mathbf{x})$ is the prior term, and α is the hyperparameter that regulates the contribution of the prior. The former ensures that our image guess is consistent with the measurements through our forward model, and the latter adds additional constraints by introducing *a priori* information of our image [2]. The function to be minimized, that is, the sum of the data fidelity and the prior term, is often called the objective function denoted by $F(\mathbf{x})$. For the data fidelity term, a common approach is to minimize the least squares error between the measurement and the estimated measurement given by applying the forward model to the image guess. The optimization problem now reads as

$$\hat{\mathbf{x}} = \arg\min \frac{1}{2}\|\mathbf{y} - \mathbf{A}\mathbf{x}\|_2^2 + \alpha\mathcal{P}(\mathbf{x}), \tag{2.5}$$

[1]For example, if the $\mathbf{A}$ operator samples the scene in spatial frequency or Fourier space, then instead of computing the entire base change matrix, we can use the discrete Fourier transform.

[2]Adding a prior term to the optimization problem falls under the category of explicit **regularization**. Regularization is a process that imposes a cost on the objective function to minimize to make the optimal solution unique. Therefore it is often employed with ill-posed problems [30].

where $\|\mathbf{a}\|_2 = \sqrt{\sum_i a[i]^2}$ represents the l_2 norm or Euclidean norm of the vector $\mathbf{a} = (a[1], a[2], ..., a[N])$. The chose of the prior depends on the specific problem. Usually it is hand-picked from these three options: squared l_2 norm $\|\mathbf{x}\|_2^2$, sparsity promoting l_1 norm in some domain $\|\Psi\mathbf{x}\|_1$, or total-variation (TV) norm $\|x\|_{TV}$. The definitions of l_1 and the TV norm, and the discussion of the choice of each prior, can be found at the end of the following section.

2.2 Solving the inverse problem

Once we have formulated the optimization problem in Eq.(2.5), we face the problem of solving it. Although there are plenty of courses, notes and books about optimization [31–35] (I recommend, for example, Simon R. Arridge's notes [36]), here we will give a brief look at the subject. Computational optimization is often done with iterative methods that converge to the desired solution. One may recall from their basic courses that to find the minimum value of a single-variable function, one has to go in the opposite direction of the derivative at the starting point. The same holds for multivariable functions, such as the objective functions of images, but where the desired direction is given by the negative gradient. This gives raise to the gradient descent algorithms.

In a nutshell, gradient descent is a way to minimize an objective function $F(\mathbf{x})$ parameterized by some variables $\mathbf{x}$ by updating them in the opposite direction of the gradient of the objective function with reference to the variables, that is, in direction of $-\nabla F(\mathbf{x})$. The process is illustrated in Fig. 2.2. In this example, the objective function is defined as a surface because the variable $\mathbf{x}$ is a two-dimensional vector. The curves indicate the isolines, that is, the lines where $F(\mathbf{x})$ is constant. And the arrows originating at each position show the direction of the negative gradients. Following the opposite direction of the gradient at each position leads us to follow the direction of the slope of the surface created by $F(\mathbf{x})$ downhill until we reach a valley.

Let us consider the minimization of an objective function composed only by the previous quadratic data fidelity term:

$$F(\mathbf{x}) = \mathcal{D}(\mathbf{x}; \mathbf{y}) = \frac{1}{2}\|\mathbf{A}\mathbf{x} - \mathbf{y}\|_2^2. \tag{2.6}$$

Note that we first consider the linear forward operator and no prior term. The nonlinear case and the prior will be discussed latter. The gradient of Eq. (2.6) is

$$\nabla F(\mathbf{x}) = \mathbf{A}^\mathsf{T}(\mathbf{A}\mathbf{x} - \mathbf{y}), \tag{2.7}$$

where $\mathbf{A}^\mathsf{T}$ is the transpose of operator $\mathbf{A}$. Given an approximation $\mathbf{x}_k$ to the minimum solution, the update

$$\mathbf{x}_{k+1} = \mathbf{x}_k - \tau\nabla F(\mathbf{x}_k), \tag{2.8}$$

will give a smaller value of $F(\mathbf{x})$, and the sequence of variables $(\mathbf{x}_n)$ converges to a minimum. The step size τ determines the size of the updates we make to reach the minimum. Using a step size τ that is to small entails a slow convergence, and

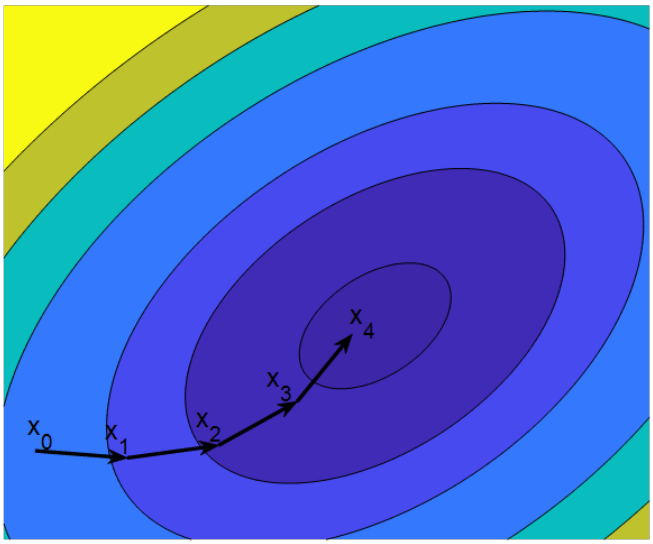

Figure 2.2: Gradient descent with constant step size for minimizing a quadratic function associated with a linear system. The colormap represents the value of the objective function.

a too large τ would lead to divergence. But, how to chose the correct step size? Besides of using a fixed step size, a common approach is to perform a line search in every iteration. The line search minimization consist in finding the optimal step size on every iteration by solving another minimization problem based, for example, on the Wolfe conditions [37, 38]. In the particular case of quadratic objective functions with linear operators, the line search minimization can be performed analytically yielding an explicit formula for the optimal step size:

$$\tau_k = \frac{\|\nabla F(\mathbf{x}_k)\|^2}{\|\mathbf{A}\nabla F(\mathbf{x}_k)\|^2}, \tag{2.9}$$

which is the step size for the *steepest descent* update [31, 34, 35] (a short and easy explanation is found in [39]). However, in many practical cases an easy to compute method that gives good results is backtracking line search [31]. This line search method starts with a relatively large step size and shrinks it geometrically until a certain stopping criterion based on the Armijo-Goldstein condition is met. An example of the implementation of gradient descent with backtracking line search method is shown in Algorithm 1.

The iterative minimization process ends when the stopping criterion is met. Some examples of stopping criteria are the objective function decreases by a sufficient amount with respect to its initial value ($F(\hat{\mathbf{x}}_\mathbf{i}) \leq \epsilon F(\hat{\mathbf{x}}_\mathbf{0})$), the relative change of the objective function falls below some threshold ($(F(\hat{\mathbf{x}}_\mathbf{i-1}) - F(\hat{\mathbf{x}}_\mathbf{i}))/F(\hat{\mathbf{x}}_\mathbf{i-1}) \leq \epsilon$), or the norm of the gradient is less than some threshold ($\|\nabla F(\hat{\mathbf{x}}_\mathbf{i})\| \leq \epsilon$).

There are three variants of gradient descent, which differ in how many of the variables are used to compute the gradient of the objective function and to update the position. The previously presented variant, Eq. (2.8), is called batch or vanilla

Algorithm 1: Gradient descent algorithm with backtracking line search

Result: Returns the estimated $\hat{\mathbf{x}}$ by minimizing the objective function $F(\mathbf{x})$ after a number $numIter$ of gradient descent steps. In each step an appropriate step size is calculated with a backtracking line search algorithm based on the Armijo-Goldstein condition.

Set value of initial step size τ_{init} (e.g., $\tau_{init} = 1$)

Set values of backtracking line search parameters $\varepsilon \in (0, 1)$, and $\gamma \in (0, 1)$ (e.g., $\frac{1}{2}$ for both)

Initialize $i = 0$ and first estimation $\hat{\mathbf{x}}_\mathbf{0}$

while stopping criterion unfulfilled **do**

  Calculate gradient: $g_i = \nabla F(\hat{\mathbf{x}}_\mathbf{i})$

  Calculate new step size with a backtracking line search algorithm based on the Armijo-Goldstein condition:

  Initialize step size: $\tau_i = \tau_{init}$

  while $F(\hat{\mathbf{x}}_\mathbf{i}) - F(\hat{\mathbf{x}}_\mathbf{i} - \tau_i\, g_i) < \varepsilon\, \tau_i\, \|g_i\|^2$ **do**

    Set $\tau_i \leftarrow \gamma \tau_i$

  end

  Update object estimation in the direction provided by the gradient:

  $\hat{\mathbf{x}}_{\mathbf{i+1}} = \hat{\mathbf{x}}_\mathbf{i} - \tau_i g_i$

  $i = i + 1$;

end

gradient descent. Here the gradient is computed with regards to all the variables. In stochastic gradient descent (SGD), the gradient is computed at a single variable of $\mathbf{x}$:

$$\mathbf{x}_{k+1} = \mathbf{x}_k - \tau \nabla F(\mathbf{x}_k[i]). \tag{2.10}$$

This is repeated for the total of variables of $\mathbf{x}$. This leads to updates that are less expensive to compute but also less accurate. SGD performs frequent updates with a high variance that cause the objective function to fluctuate heavily. This hinders convergence close to the minimum, but also can help to overcome getting stuck in a local minimum. However, the greatest benefit lies in not needing to use all the variables to compute the gradient which makes it suitable for cases where the number of variables is extremely large. Finally, there is a variant that tries to achieve a trade off between batch and stochastic gradient descent: mini-batch gradient descent. In mini-batch gradient descent, for every iteration, the gradient of the objective function is computed for a small number n of variables, called mini-batches, of $\mathbf{x}$:

$$\mathbf{x}_{k+1} = \mathbf{x}_k - \tau \nabla F(\mathbf{x}_k[i : i + n]). \tag{2.11}$$

This way variance of the updates is reduced, leading to a better convergence, and yet still the computation of the gradient can be faster.

Gradient descent is generally a slow method. Therefore, there are several algorithm implementations to optimize gradient descent. Here we will only address some of them, such as momentum, Nesterov's accelerated gradient or conjugate gradients.

For a review of these, and more gradient descent optimization algorithms, I recommend the blog or article of Refs. [40, 41]. Mainly these optimizations of gradient descent are based on choosing a better update direction, denoted by $\mathbf{p}$, than the one given by the gradient.

Momentum is a method that accelerates gradient descent by adding a fraction $m \in [0, 1]$ of the update direction of the previous step to the current update direction:

$$\begin{aligned} \mathbf{p}_k &= m\mathbf{p}_{k-1} + \nabla F(\mathbf{x}_k) \\ \mathbf{x}_{k+1} &= \mathbf{x}_k - \tau \mathbf{p}_k. \end{aligned} \tag{2.12}$$

The way momentum works in gradient descent is the same as in the example of a ball rolling down a hill, the ball gets faster as it accumulates momentum as it rolls downhill. The momentum term increases if successive gradients point in the same directions, accelerating the descent; and decreases if they change directions, reducing or damping oscillations in the descent direction. This results in a faster convergence, less variance in the updates and more likelihood to avoid (roll over) local minima [42, 43].

Another gradient descent acceleration method is Nesterov's accelerated gradient (NAG) [44]. In the example of a ball running downhill, with momentum this ball rolls blindly following the slope. Wouldn't it be better to have a smarter ball that looks ahead to get a sense of where it is going? This idea of looking ahead is the intuition behind NAG. NAG gives our momentum term this kind of prescience by computing it the following way:

$$\begin{aligned} \mathbf{p}_k &= m\mathbf{p}_{k-1} + \nabla F(\mathbf{x}_k - m\mathbf{p}_{k-1}) \\ \mathbf{x}_{k+1} &= \mathbf{x}_k - \tau \mathbf{p}_k. \end{aligned} \tag{2.13}$$

The explanation is as follows: as we know that we will use our momentum term $m\mathbf{p}_{k-1}$ to update our variable, $\mathbf{x}_k - m\mathbf{p}_{k-1}$ thus gives an approximation to the new position, and we can now look ahead by computing the gradient with respect to the approximated new position. While gradient descent with standard momentum first computes the gradient at the current location and then takes a big jump in the direction of the updated accumulated gradient. In contrast, with Nesterov's momentum we first take a big jump in the direction of the previous accumulated gradient, calculate the gradient at this updated position and then make a correction. NAG reduces oscillations and avoids in some extent overshooting when approaching the minima of the objective function.

In conjugate gradients the update is computed as follows [36, 45, 46]:

$$\begin{aligned} \gamma_k &= \frac{\langle \nabla F(\mathbf{x}_k), \mathbf{A}^\mathsf{T}\mathbf{A}\mathbf{p}_{k-1} \rangle}{\langle \mathbf{p}_{k-1}, \mathbf{A}^\mathsf{T}\mathbf{A}\mathbf{p}_{k-1} \rangle} \quad \text{or} \quad \frac{\|\nabla F(\mathbf{x}_k)\|^2}{\|\nabla F(\mathbf{x}_{k-1})\|^2} \\ \mathbf{p}_k &= \gamma_k \mathbf{p}_{k-1} + \nabla F(\mathbf{x}_k) \\ \tau_k &= \frac{\|\nabla F(\mathbf{x}_k)\|^2}{\langle \nabla F(\mathbf{x}_k), \mathbf{A}^\mathsf{T}\mathbf{A}\mathbf{p}_k \rangle} \quad \text{or} \quad \frac{\|\nabla F(\mathbf{x}_k)\|^2}{\langle \mathbf{p}_k, \mathbf{A}^\mathsf{T}\mathbf{A}\mathbf{p}_k \rangle} \\ \mathbf{x}_{k+1} &= \mathbf{x}_k - \tau_k \mathbf{p}_k, \end{aligned} \tag{2.14}$$

where $\langle\ ,\ \rangle$ denotes the dot product. This update rule is similar to momentum but instead of adding a fixed fraction of the previous direction to the current gradient,

a variable fraction is added. This results in a search direction, that after a few steps, points in the direction of the minimum rather than in the normal direction of the isolines, as it happens in standard gradient descent (see Fig. 2.3). Therefore, conjugate gradients needs less steps to converge, theoretically the same number of steps as the dimensionality of our problem.

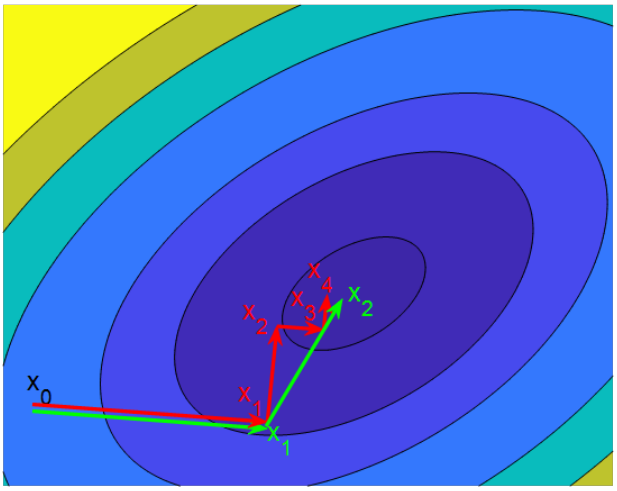

Figure 2.3: Comparison of the steepest descent (gradient descent with optimal step size, in red) and conjugate gradients (in green) for minimizing a quadratic function associated with a linear system. The update directions in gradient descent are always normal to the isolines defined at that point, creating a *zigzag* trajectory. While in the case of conjugate gradients, after the first step, the update directions point in the direction of the center of the ellipsoid. Note also that conjugate gradients needs less steps to converge than steepest descent.

In the case of an objective function with a least squares data fidelity term with a nonlinear forward operator, namely

$$F(\mathbf{x}) = \frac{1}{2}\|\mathcal{A}(\mathbf{x}) - \mathbf{y}\|_2^2, \tag{2.15}$$

the gradient is given by

$$\nabla F(\mathbf{x}) = \mathbf{J}^\mathsf{T}(\mathcal{A}(\mathbf{x}) - \mathbf{y}), \tag{2.16}$$

where $\mathbf{J}$ is the Jacobian matrix of $\mathcal{A}(\mathbf{x})$. In this case gradient descent and conjugate gradients can still be used, but the step size needs to be determined by a line search method, like the backtracking line search algorithm. Also, for conjugate gradients the parameter γ is usually calculated with one of the following expressions which are named after their developers:

$$\gamma_k = \frac{\|\nabla F(\mathbf{x}_k)\|^2}{\|\nabla F(\mathbf{x}_{k-1})\|^2} \tag{2.17}$$

is the Fletcher-Reeves formula [36, 47],

$$\gamma_k = \frac{\langle \nabla F(\mathbf{x}_k), \nabla F(\mathbf{x}_k) - \nabla F(\mathbf{x}_{k-1}) \rangle}{\|\nabla F(\mathbf{x}_{k-1})\|^2} \tag{2.18}$$

is the Polak-Ribière formula [36, 48], and

$$\gamma_k = \frac{\langle \nabla F(\mathbf{x}_k), \nabla F(\mathbf{x}_k) - \nabla F(\mathbf{x}_{k-1}) \rangle}{\langle \mathbf{p}_{k-1}, (\nabla F(\mathbf{x}_k) - \nabla F(\mathbf{x}_{k-1}) \rangle} \tag{2.19}$$

is the Hestenes-Stiefel expression [45]. The choice of one or the other is mainly a heuristic matter [36, 46].

In the nonlinear case one could also linearize the minimization problem. This is done by linearizing $\mathcal{A}(\mathbf{x})$ in the vicinity of the current guess $\mathbf{x}_k$:

$$\tilde{\mathcal{A}}(\Delta\mathbf{x}_k; \mathbf{x}_k) \approx \mathcal{A}(\mathbf{x}_k) + \mathbf{J}\Delta\mathbf{x}_k, \tag{2.20}$$

where $\Delta\mathbf{x}_k = \mathbf{x} - \mathbf{x}_k$ and $\mathbf{J}$ is again the Jacobian matrix calculated with respect to $\mathcal{A}(\mathbf{x}_k)$. Then by substituting $\mathcal{A}(\mathbf{x})$ by its affine approximation $\tilde{\mathcal{A}}(\Delta\mathbf{x}_k; \mathbf{x}_k)$, and by multiplying both summands by $\mathbf{J}^\mathsf{T}$ in eq. (2.15), the following objective function is obtained:

$$\tilde{F}(\Delta\mathbf{x}_k; \mathbf{x}_k) = \frac{1}{2}\|\mathbf{J}^\mathsf{T}\mathbf{J}\Delta\mathbf{x}_k - \mathbf{J}^\mathsf{T}(\mathbf{y} - \mathcal{A}(\mathbf{x}_k))\|_2^2. \tag{2.21}$$

The nonlinear optimization problem is solved by iteratively taking small linear steps given by the update

$$\mathbf{x}_{k+1} = \mathbf{x}_k + \Delta\mathbf{x}_k, \tag{2.22}$$

where $\Delta\mathbf{x}_k$ is obtained by solving the linear least squares problem

$$\Delta\hat{\mathbf{x}}_\mathbf{k} = \arg\min \tilde{F}(\Delta\mathbf{x}_k; \mathbf{x}_k), \tag{2.23}$$

which is solved with one of the methods for linear systems. This method is known as the Gauss-Newton method [31, 36].

Adding a regularization or "damping" term of the form

$$\alpha\mathcal{P}(\Delta\mathbf{x}_k) = \alpha\|\Gamma\Delta\mathbf{x}_k\|_2^2 \tag{2.24}$$

to objective function (2.21) yields

$$\tilde{F}(\Delta\mathbf{x}_k; \mathbf{x}_k) = \frac{1}{2}\|(\mathbf{J}^\mathsf{T}\mathbf{J} + \alpha\Gamma^\mathsf{T}\Gamma)\Delta\mathbf{x}_k - \mathbf{J}^\mathsf{T}(\mathbf{y} - \mathcal{A}(\mathbf{x}_k))\|_2^2, \tag{2.25}$$

with Γ being a regularization matrix. For example, it can be chosen to be the identity matrix ($\Gamma = \mathbf{I}$), prioritizing solutions with smaller norms (known as l_2 regularization), or an operator performing the Fourier transform, to enforce smoothness. This regularization improves the conditioning of the problem, and is what differentiates the Levenberg-Marquardt algorithm from the Gauss-Newton algorithm [36, 49, 50].

Next we will consider the minimization of an objective function that involves not only a data fidelity term but also a prior. First we consider the case of the l_2 norm term, as in the case of the Levenberg-Marquardt algorithm:

$$\mathcal{P}(\mathbf{x}) = \frac{1}{2}\|\Gamma\mathbf{x}\|_2^2. \tag{2.26}$$

Regularization with this kind of terms is also commonly known as Tikhonov regularization, Ridge regression or weight decay [51, 52]. Here the prior term is divided by two for the sake of convenience and weighted by the hyperparameter α. The gradient of this term yields:

$$\nabla \mathcal{P}(\mathbf{x}) = \Gamma^{\mathsf{T}}\Gamma\mathbf{x}, \tag{2.27}$$

thus the update is

$$\mathbf{x}_{k+1} = \mathbf{x}_k - \tau(\nabla \mathcal{D}(\mathbf{x_k}) + \alpha\nabla \mathcal{P}(\mathbf{x_k})) = (1 - \tau\alpha\Gamma^{\mathsf{T}}\Gamma)\mathbf{x}_k - \tau\nabla \mathcal{D}(\mathbf{x_k}), \tag{2.28}$$

which is similar to the update during gradient descent without regularization, but with the difference that we introduce an additional subtraction from the current guess. If the regularization matrix is chosen to be orthogonal $\Gamma^{\mathsf{T}}\Gamma = \mathbf{I}$, or the identity matrix, then the contribution of the regularization consists in reducing our image vector in a fraction $\tau\alpha$. Adding a prior term like this encourages the image values to be small (towards zero, but not exactly zero).

Another commonly used prior is the l_1 norm, defined as the sum of the absolute values of the elements of a vector:

$$\mathcal{P}(\mathbf{x}) = \|\Psi\mathbf{x}\|_1 = \sum_i |(\Psi\mathbf{x})[i]|. \tag{2.29}$$

where Ψ is some regularization matrix chosen in a way that the transformed image vector is sparse. Therefore the l_1-norm prior promotes sparsity (having relatively few nonzero components) of our vector under some transformation. This kind of l_1 regularization is also known as Lasso regression [30, 52]. The derivative or gradient of this prior term leads to the following expression:

$$\nabla \mathcal{P}(\mathbf{x}) = \Psi^{\mathsf{T}} sign(\Psi\mathbf{x}), \tag{2.30}$$

where $sign(\cdot)$ is the sign function. The update rule is

$$\mathbf{x}_{k+1} = \mathbf{x}_k - \tau\left(\nabla \mathcal{D}(\mathbf{x_k}) + \nabla \mathcal{P}(\mathbf{x_k})\right) = \mathbf{x}_k - \tau\left(\nabla \mathcal{D}(\mathbf{x_k}) + \alpha\Psi^{\mathsf{T}} sign(\Psi\mathbf{x})\right). \tag{2.31}$$

The effect of this prior is best understood with the example of an identity regularization matrix $\Psi = \mathbf{I}$. In this case a constant fraction α is added or subtracted from every element of vector $\mathbf{x}$ depending on whether it is positive or negative, respectively, therefore encouraging the image values to be zero.

Another option for the prior is to minimize the TV-norm of the image:

$$\mathcal{P}(\mathbf{x}) = \|\mathbf{x}\|_{TV}, \tag{2.32}$$

where the TV-norm is defined for a two-dimensional signal or image as:

$$\|\mathbf{x}\|_{TV} = \sum_{i,j} \sqrt{(x[i,j] - x[i-1,j])^2 + (x[i,j] - x[i,j-1])^2}. \tag{2.33}$$

which can be interpreted as l_2-norm minimization but where the regularization matrix is defined as the two-dimensional gradient. Taking the derivative of the TV-

norm with respect to each pixel results in the following expression [53, 54]:

$$\begin{aligned}\nabla\mathcal{P}(\mathbf{x})[i,j] =& 2\left[\frac{(x[i,j]-x[i-1,j])+(x[i,j]-x[i,j-1])}{\sqrt{(x[i,j]-x[i-1,j])^2+(x[i,j]-x[i,j-1])^2}}+\right.\\ &-\frac{(x[i+1,j]-x[i,j])}{\sqrt{(x[i+1,j]-x[i,j])^2+(x[i+1,j]-x[i+1,j-1])^2}}+\\ &\left.-\frac{(x[i,j+1]-x[i,j])}{\sqrt{(x[i,j+1]-x[i-1,j+1])^2+(x[i,j+1]-x[i,j])^2}}\right].\end{aligned} \tag{2.34}$$

Note that this expression is not valid for border pixels. In essence, this TV-norm regularization or prior term has a denoising effect on the image as it tries to minimize the derivative (differences) between adjacent pixels, promoting piecewise constant images.

It is worth mentioning that the l_1 and TV-norm are non differentiable (non-smooth) functions, and therefore the previously presented gradients are in fact sub-gradients. Subgradient methods tend to have poor convergence rates [55]. Proximal gradient methods, such as FISTA[3] [56] or ADMM[4] [57] for imaging inverse problems, provide better convergence by formulating a smooth approximation to the non differentiable prior function by applying a proximal method [58]. For example, the proximal operator for the l_1-norm is soft-thresholding, $\text{prox}_{\alpha\|\cdot\|_1}(u_i) = \text{soft}(u_i, \alpha) = \text{sign}(u_i)\max(|u_i| - \alpha, 0)$. In fixed point iterative schemes, like in the FISTA algorithm, the contributions of the smooth data fidelity function and the non-smooth prior function are decoupled by alternating a gradient descent step with respect to the data fidelity term and a soft thresholding step to enforce sparsity from the l_1 prior [58, 59]. That is, the update is written as:

$$\begin{aligned}\mathbf{u}_k &= \mathbf{x}_k - \tau\nabla\mathcal{D}(\mathbf{x}_k)\\ \mathbf{x}_{k+1} &= \text{prox}_{\alpha\mathcal{P}}(\mathbf{u}_k) = \text{soft}(\mathbf{u}_k, \tau\alpha).\end{aligned} \tag{2.35}$$

2.3 Single-pixel imaging

The single-pixel camera (SPC) [60,61] is a perfect example of computational imaging formulated with equations (2.2) and (2.3). Single-pixel imaging (SPI) is based on sampling the object ($\mathbf{x}$) with a sequence of masks (rows of measurement matrix $\mathbf{A}$) and the corresponding measurement of the total intensity coming from the overlap of these masks and the object (stored in the vector $\mathbf{y}$). The most remarkable fact is that the detector does not need to have a pixelated structure. It is a so-called single-pixel detector[5] And opposed to a conventional camera, that captures the image in a single exposure by mapping one-to-one the regions of the scene onto the pixelated sensor plane, the measurements of the SPC are acquired in a sequential manner by scanning the scene with the masks. We can construct our measurement matrix with any orthonormal set of functions. Given an object of dimension N (where N

[3]Fast iterative shrinkage-thresholding algorithm.

[4]Alternating direction method of multipliers.

[5]Sometimes, single-pixel detectors are also called bucket detectors because of their ability to recollect all the light coming from the overlapping of the object and the sampling masks.

is the number of pixels), we just need to chose a mathematical basis of this N-dimensional space as our measurement basis. This basis can be the canonical basis (where $\mathbf{A} = \mathbf{I}$[6]), Hadamard, Fourier, discrete cosine, or wavelet, among many other. Except for the canonical basis, all of these bases share two features. First, each of the measurements with these bases takes information about several pixels of the image at the same time, instead of taking information from one single pixel. This usually increases the SNR of the measurements [62,63]. Second, while the inverse of the measurement matrix can be computed for recovering the object via Eq. (2.3), this entails memory and speed limitations as inverting matrices with a large number of entries is quite inefficient. However, these bases are associated with fast and efficient digital transformation algorithms, that make the inversion feasible even for larger image sizes.

From an experimental point of view, the SPC consists of two main parts: the spatial light modulator (SLM) and the single-pixel detector. Many different SLM technologies are used for single-pixel imaging, such as LED arrays or liquid-crystal devices (LCD), however the most convenient and commonly used choice are digital light projectors (DLP) based on digital micromirror devices (DMDs)[7]. Thus, for the remainder of this section we will consider the use of DMDs only. A DMD consist of an array of several hundred thousand of individually addressable micromirrors (with size in the order of ten microns). Each micromirror can be tilted at $\pm 12°$ with respect to the normal plane of the array. This way we can either reflect or block light in one direction depending on the state of the micromirror. Therefore the DMD can be used as a programmable binary reflective SLM. One advantage of DMDs is their working principle based on semiconductor technologies, providing high modulation rates (around 22kHz, but also up to 50kHz [64], or even 100kHz [65]), compared to LCDs. Another advantage is that the micromirrors are made from metal (usually aluminium) with low losses over the visible (and even the IR) spectrum. The masks and the sample need to physically overlap before measuring the intensity value. But this overlap can be done in different planes. This gives rise to two slightly different experimental SPC configurations [60,61]. In the former, the DMD is used to modulate the light projected onto the scene, whereby the overlap occurs on the scene plane. This is also referred to as structured illumination. The latter scheme does not project structured patterns onto the scene, but does project an image of the scene onto the plane of the SLM. This configuration is referred to as structured detection. During this thesis both configurations have been used in different works.

The relative low number of pixels and refresh rate of current SLMs create the bottleneck in resolution and acquisition speed of the SPC. While this problem can be partially overcome by using advanced signal processing techniques such as adaptive sensing strategies [66,67] or compressive sensing (CS, which will be discussed in the next section), the SPC still offers modest resolution compared to conventional CCD or CMOS sensors which have millions of pixels, and are cheap and fast. One might be asking *"what is the point in using a SPC?"*. The answer is the following: for

[6]This seems identical to the case of a conventional camera but where the measurement of the intensity of each pixel is sequential in time and no pixelated sensor is needed. This is also known as raster scanning.

[7]Even if DMD refers to the chip containing the micromirrors, it is commonly used to refer to the whole light modulating device which includes the DMD chip but also the control electronics.

conditions or tasks where pixelated sensors are neither cheap nor fast, where they are not good enough and their single-pixel counterparts outperform them, or, in the worst case, where array detectors are not even available. Single-pixel detectors can be build in a broad range of spectral ranges, whereas pixelated sensors outside the visible range tend to have relatively high costs (like in the infrared [25, 26, 68], UV [69], and X and gamma rays [70–73] region of the electromagnetic spectrum, or even for electrons [74] and neutrons [75, 76]) or are nonexistent (like in the terahertz regions [77–79]). Also high sensitivity pixelated sensors are more expensive than single-pixel detectors such as avalanche photodiodes (APDs) or single-photon avalanche diodes (SPAD) [67, 80, 81]. However, the area where the SPC stands out the most is probably in multidimensional imaging, where specialized single-pixel detectors allow to easily build cameras sensitive to spectral [82–87], time [83], polarization [85, 88, 89], depth or 3D [86, 90, 91], and holographic or phase [87, 92–94] information.

Besides from the limited refresh rate and number of micromirrors, DMD technology has another limitation: they are binary intensity-only modulators. That does not mean that we are restricted to using basis functions that are binary and positive valued. Almost any function can be generated with the DMD[8]. However implementing such functions comes at a cost. The binary limitation can be by-passed using spatial or temporal multiplexing. By using temporal multiplexing, grayscale values are achieved by changing the amount of time each micromirror spends in the bright and dark state. By using spatial multiplexing, instead of trading temporal resolution for gray levels, spatial resolution is traded. This works by grouping several micromirrors into a *macropixel* whose grayscale value is determined by the ratio of micromirrors that are in the bright and dark state [96, 97]. In order to generate negative-valued functions, temporal multiplexing can also be used.

These are some of the reasons why the Hadamard basis is a popular choice for single-pixel imaging. The use of this basis for SPI was first demonstrated in [98]. The functions of the Hadamard basis are orthogonal with binary values of $+1$ or -1, thus allowing to take advantage of the full refresh rate of the DMD. Hadamard matrices are orthogonal and symmetric, that is, their transpose is equal to its inverse ($\mathbf{H}^\mathsf{T} = \mathbf{H}^{-1}$) and they are their own transpose ($\mathbf{H} = \mathbf{H}^\mathsf{T}$) such that $\mathbf{H}\mathbf{H}^\mathsf{T} = N\mathbf{I}$. This means that the inverse problem of image reconstruction (Eq. (2.3))can be performed without matrix inversion. Also a fast digital transform is available for the Hadamard basis: the fast Walsh-Hadamard transform (FWHT) [99]. The sampling masks for imaging a N pixel image (of size $\sqrt{N} \times \sqrt{N}$) are created by reshaping the rows[9] of the Hadamard matrix (of size $N \times N$) to be the same size as the image. Examples of a Hadamard matrix and the sampling masks are shown in Fig. 2.4.

We can codify negative values by taking into account that the measurement

[8]Even complex-valued functions can be generated by a DMD by means of computer generated holograms [92, 95].

[9]The one-dimensional functions represented by the rows of the Hadamard matrix are called Walsh functions, and the reshaped two-dimensional functions are called Walsh-Hadamard functions.

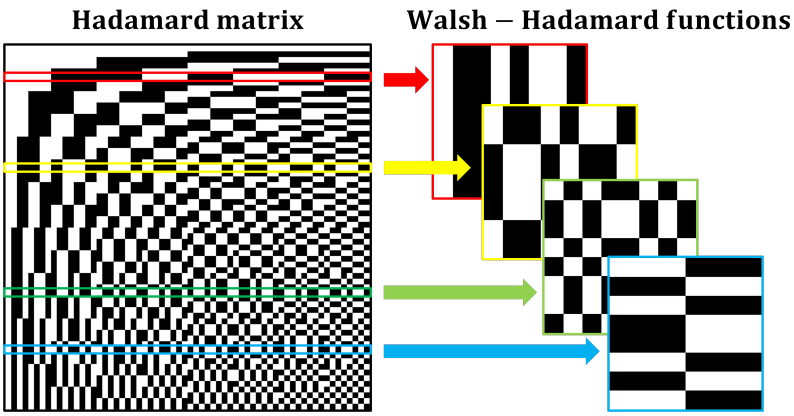

Figure 2.4: Example of the Hadamard matrix of order $N = 64$ (the matrix size is $N \times N = 64 \times 64$), and some of the corresponding masks (Walsh-Hadamard functions) of size $\sqrt{N} \times \sqrt{N} = 8 \times 8$ used to sample the scene with a SPC.

process of Eq. (2.2) is linear and that the Hadamard matrix can be expressed as

$$\begin{aligned} \mathbf{H} &= \mathbf{H}^{+} - \mathbf{H}^{-}, \\ \mathbf{H}^{+} &= \frac{1}{2}\left(\mathbb{1} + \mathbf{H}\right), \\ \mathbf{H}^{-} &= \frac{1}{2}\left(\mathbb{1} - \mathbf{H}\right), \end{aligned} \tag{2.36}$$

which is a linear combination of two positive valued matrices $\mathbf{H}^{+}$ and $\mathbf{H}^{-}$, and where $\mathbb{1}$ is a matrix where every entry is equal to one. $\mathbf{H}^{+}$ is the Hadamard matrix where all the entries with value -1 are set to 0, and $\mathbf{H}^{-}$ is its complementary. With these properties the measurement can be expressed as a two step process:

$$\mathbf{y} = \mathbf{y}^{+} - \mathbf{y}^{-} = \mathbf{H}^{+}\mathbf{x} - \mathbf{H}^{-}\mathbf{x}, \tag{2.37}$$

where in order to measure a single coefficient of $\mathbf{y}$, first we have to project the corresponding function of $\mathbf{H}^{+}$, then its complementary function, and finally subtract the measured values. This differential measurement process removes parasite signals such as ambient light, or slow fluctuations of the light source. However, it comes at the cost of doubling the number of patterns to be displayed on the DMD. In the structured detection configuration, one can exploit both reflection directions of the DMD (one arising from the micromirrors in the on state and another from the micromirrors in the off state which display the complementary pattern) to measure simultaneously the projections of $\mathbf{H}^{+}$ and $\mathbf{H}^{-}$. Furthermore, instead of using two photodetectors, a single balanced detector, which subtracts the two signals in the electrical domain, can be used to increase the dynamic range of the detection [100]. The two reflection arms of the DMD can also be used to measure simultaneously with two different detectors. For example, this allows to acquire two different multidimensional images at the same time. Information from these two images could be joined by using some data fusion algorithm as discussed in section 2.5.

It is interesting to note that a random permutation of the columns of the Hadamard matrix $\mathbf{H}$ does change its symmetry but not its orthogonality. Therefore this random alteration of the order of the columns generates a set of basis functions that

resemble random or noise-like masks with all the advantages of a complete and deterministic base. This is known as scrambled Hadamard [101]. Examples of a scrambled Hadamard matrix and Walsh-Hadamard sampling masks are shown in Fig. 2.5. The FWHT can still be used with scrambled Hadamard by taking into account that sampling an image with disordered masks is the same as sampling a disordered image with standard Hadamard functions.

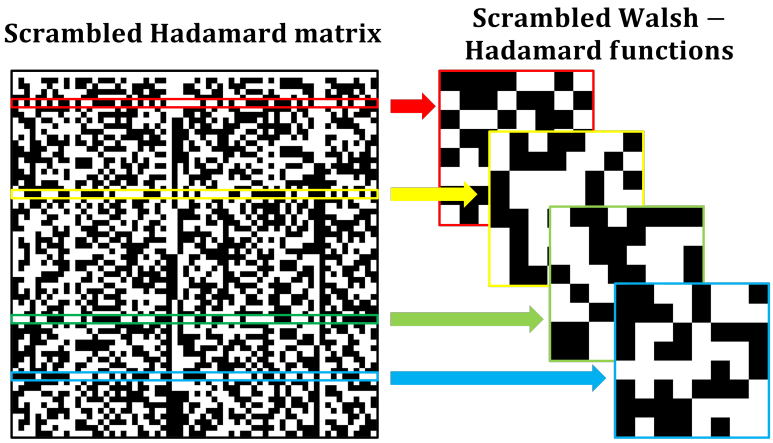

Figure 2.5: Example of an scrambled Hadamard matrix of order $N = 64$ (the matrix size is $N \times N = 64 \times 64$), and some of the corresponding masks (Walsh-Hadamard functions) of size $\sqrt{N} \times \sqrt{N} = 8 \times 8$ used to sample the scene with a SPC.

Also we are not restricted to square masks. They can be tailored to the specific problem. For example, the rows of $\mathbf{H}$ could be reshaped into rectangular masks rather than square ones. In optics, a circular field of view is quite common, so it is not surprising that masks that fill a circular area are desirable. In the work described in Ref. [102], circular Hadamard masks are created by sequentially filling a circular shaped area with the values of the Walsh-Hadamard functions. In Ref. [103], circular Fourier patterns for SPI are used. In the work in Ref. [104], we created circular (and scrambled) Walsh-Hadamard masks for SPI. In this work the bucket detector was an integrating sphere with round apertures, and in order to image the largest possible area we had to project circular masks. The work in question is discussed in detail in the section 4.4. In Fig. 2.6, we show the schematics of the proposed circular Walsh-Hadamard masks. The values along the rows of the Walsh-Hadamard matrix are used for encoding equiangular segments, while the values along the columns are used for encoding disks that scale with the squared radius. Basically we assume that the Walsh-Hadamard matrices are represented in the (ρ^2, ϕ) space, and then we cast them to the (x, y) space. A similar strategy for encoding circular Hadamard matrices can be found in [105, 106], although without application in SPI. The resulting patterns are orthogonal and have a constant pixel area.

2.4 Compressive sensing

Compressive sensing (CS) is a novel sampling theory that aims to reconstruct signals from under-sampled measurements by combining sampling and compression into a single measurement step [107–110]. SPI usually goes in conjunction with CS due to the coded nature of acquisition, and the fact that most images are compressible

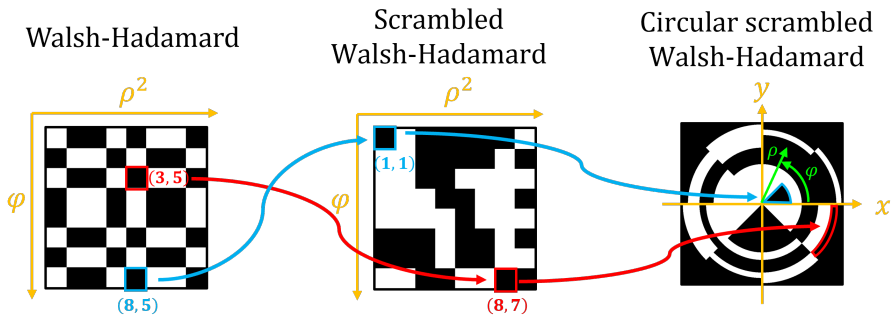

Figure 2.6: Schematic of the implementation of circular and scrambled Walsh-Hadamard masks for SPI. On the left we have a standard Walsh-Hadamard matrix which is assumed to be represented in the (ρ^2, ϕ). In the middle we have the same matrix but with a random permutation of the matrix entries. And on the right we have the projection of this matrix in the (x, y) space. The position of two specific entries have been remarked in blue and red.

[60, 61, 98]. Here CS aims to reduce the number of masks to scan the scene (and therefore acquisition time) by acquiring fewer measurements, lets say a number M, than the number of pixels, N, of the final reconstructed image. It relies on the fact that images typically have a sparse representation in some basis, such as Fourier, discrete cosine, Hadamard, or wavelet bases. This means that most elements of the vector representing the transformed image are zero (or almost zero), and only a few are nonzero. This fact is also exploited in conventional image compression such as JPEG [111]. First, you acquire the full image. Then, you choose a mathematical basis in which your image is sparse, and only store the most relevant elements of the transformed image. With this approach, in order to compress an image, first you need to measure all the information, and then you throw away most of it. It seems more clever to measure the relevant data in the first place. And this is what is accomplished with CS.

The mathematical formulation of the measurement process is, again, given by Eq. (2.2), where the measurement matrix $\mathbf{A}$ is non-square (of size $M \times N$). Also we suppose that our image, $\mathbf{x}$, can be expressed in a different basis, $\mathbf{R}$ (usually called recovery basis), where it has a K-sparse representation $\mathbf{s}$, that is

$$\mathbf{s} = \mathbf{R}\mathbf{x}. \tag{2.38}$$

This means that only K elements of $\mathbf{s}$ will be nonzero, and $N - K$ elements will be zero or very close to zero. However, the nonzero elements are not known in advance and therefore we cannot measure directly with the sparse basis because most of the relevant information would be omitted. Therefore, the measurement basis, that is physically modulated with the DMD, has to be chosen to be maximally incoherent with $\mathbf{R}$ [107, 110, 112, 113]. This incoherence can be understood as a measure of dissimilarity between the elements of each basis. That is, every function represented by a row of $\mathbf{A}$ should have a non-sparse representation in the recovery basis $\mathbf{R}$. This assures that each measurement contains information about many of the elements of the sparse representation.

CS theory states that, with a number of measurements that satisfies the condition

$M \geq O(K \log(N/K))$, the image in the sparse domain can be exactly, or at least approximately, recovered by solving an optimization problem, commonly expressed as

$$\hat{\mathbf{s}} = \arg\min \|\mathbf{s}\|_1 \text{ subject to } \|\mathbf{A}\mathbf{R}^{-1}\mathbf{s} - \mathbf{y}\|_2 \leq \epsilon, \tag{2.39}$$

where ϵ quantifies the uncertainty in the measurement $\mathbf{y}$ due to noise. Whereupon the image in the canonical (or pixel) domain can be recovered by

$$\mathbf{x} = \mathbf{R}^{-1}\mathbf{s}. \tag{2.40}$$

The optimization problem of Eq. (2.39) is known as the basis pursuit problem (with inequality constraints). Another approach considers solving the problem in Lagrangian form, i.e.,

$$\hat{\mathbf{s}} = \arg\min \frac{1}{2}\|\mathbf{A}\mathbf{R}^{-1}\mathbf{s} - \mathbf{y}\|_2^2 + \alpha\|\mathbf{s}\|_1, \tag{2.41}$$

which is the same formulation as the inverse problem of Eq. (2.4) but where $\mathbf{A}$ has been changed for $\mathbf{A}\mathbf{R}^{-1}$. And although standard optimization theory states that these two problems are theoretically equivalent, in practice they are not equally easy to solve [114, 115].

The role of the l_1-norm regularization term in Eq. (2.39) or (2.41) is to ensure the sparsest solution. Although the correct norm minimization that promotes sparsity is the l_0-norm, solving Eq. (2.39) or (2.41) with this norm is both numerically unstable and a NP-hard problem, whereas l_1-minimization can closely recover compressible signal while being a linear problem without to much complexity [98,108,109,112,116].

To obtain the best results, the recovery basis should be chosen so that $\mathbf{s}$ is very sparse, and to measure using functions that are as incoherent as possible with respect to the recovery basis. The former condition is easily meet by using common mathematical bases, such as discrete cosines, Fourier, Hadamard, or wavelets; in which natural images tend to be sparse. Regarding the latter condition, for example, we can use a random subset of a basis matrix (which of course should be different than the recovery basis). This enables faster computations through fast transform algorithms. However, these subsets of basis functions are far from being the optimal choice regarding incoherence. A better option is to use random functions, as they are maximally incoherent with most of the recovery bases. An even better choice in some cases is to use a standard orthonormal basis whose functions have randomly permuted entries, e.g. scrambled Hadamard, which has similar incoherence properties to random functions and associated fast transforms.

Alternatively, a regularization consisting in minimizing the total variation (TV) and reconstructing directly in the canonical domain in chosen. The optimization problem in this case is written as

$$\hat{\mathbf{x}} = \arg\min \|\mathbf{x}\|_{\text{TV}} \text{ subject to } \|\mathbf{A}\mathbf{x} - \mathbf{y}\|_2 \leq \epsilon. \tag{2.42}$$

In this case only one basis, the measurement basis, has to be chosen.

There are several (off-the-shelf) implementations of the CS algorithm available, such as Gradient Projection for Sparse Reconstruction (GPSR) [117], Spectral Projected Gradient for L_1 minimization (SPGL1) [118,119], L1 Magic [120,121], TVAL3

[122], or NESTA [115, 123], among several more. Of the algorithms mentioned above, the only ones capable of minimizing the TV norm are L1 Magic, NESTA and TVAL3 [124]. The L1 Magic package is not a single algorithm, but several; developed as a educational tool for CS. However, it is not suited for large scale problems or difficult ill-posed problems as it lacks optimization and robustness. Faster and more robust options are given by the TVAL3 and NESTA algorithms. The TVAL3 algorithm is based on an augmented Lagrangrian multiplier approach. NESTA in short stands for Nestorov's algorithm, and as the name may suggest, it is based on two of Yurii Nestorov's ideas. The first idea is the accelerated gradient as described in section 2.2 The second idea is a smoothing technique based on a proximal method to replace the non-smooth l_1 or TV-norm with smoothed versions [125].

2.5 Data Fusion

Data fusion (DF) techniques aim to combine any number of individual datasets into one single dataset that provides more consistent, accurate, and useful information than that provided by any of the individual datasets. Similar to the ability of animals and humans to combine information from multiple senses to improve their ability to survive and to thrive, i.e. combining information from sight, smell, taste, our touch to determine if it is safe to eat some food [126]; multidimensional data fusion systems are capable of providing new insights into sample characteristics from a combined view of multispectral, time-resolved, or polarimetric views of the scene [127–130].

Historically, some of the main fields of applications of DF have been remote sensing and satellite imaging, where high spatial and high spectral resolution in a single image is required, and where satellite design imposes severe constraints on the energy consumption, bandwidth, number, size and weight of detectors [131–133]. Given these limitations, usually a single detector is not capable of providing the desired data convincingly. Therefore it is quite normal to have multiple sensors, each one with different spatial resolution and sensitive to a different spectral range or to the polarization state of light. Usually two types of images are available, high spatial resolution grayscale images (panchromatic images) and multispectral images with coarser spatial resolution. After capturing the different images the DF procedure helps to obtain rich chemical and morphological information about the imaged surface.

Another important area of application for DF is life sciences, where the fusion of information from different imaging modalities, such as ultrasound, magnetic resonance image (MRI), computed tomography (CT), or positron emission tomography (PET), has been shown to offer insights that individual sources cannot provide [134–140]. Another fields that benefit from DF are traffic state determination [141], robotics [142], mobile phone cameras [143] or autonomous vehicles [142, 144]. In the latter case, data fusion is used to combine information from many different sensors, such as visible cameras for high spatial resolution, stereo depth cameras, radar, lidar and ultrasonic sensors to provide a cloud of points in the 3D space, and inertial measurement units providing information about the kinematics and dynamics of the car.

Fusion of images from any number of different cameras can be formulated similarly

to the general computational imaging problem. We suppose that the forward model for each of this cameras is given by the matrix $\mathbf{A}_i$, that is, the *i-th* camera performs a measurement $\mathbf{y}_i$ on the object $\mathbf{x}$ given by

$$\mathbf{y}_i = \mathbf{A}_i \mathbf{x}. \tag{2.43}$$

Please note that the object $\mathbf{x}$ can be of any dimension. For example, if we wanted to combine information from a multispectral camera with low spatial resolution and a monochrome high resolution camera, then the merged image $\mathbf{x}$ would be a high resolution multispectral image. As the measurements usually entail a size or dimension reduction, Eq. (2.43) can be understood as the projection of the full image over some subspace. With the previous example, the measurement of the monochrome camera is a projection over the full 2D space, while the multispectral camera provides a projection of $\mathbf{x}$ into the low spatial resolution and spectral space.

Given the datasets or set of mesurements $(\mathbf{y}_i)$, the problem of finding an estimation of the merged image $\mathbf{x}$, that is compatible with all the individual measurements, is formulated as the following minimization problem:

$$\hat{\mathbf{x}} = \arg\min F(\mathbf{x}), \tag{2.44}$$

where the objective function is defined as the weighted sum of the quadratic differences between the projected x and the corresponding measurements, that is

$$\begin{aligned} F(\mathbf{x}) =& \sum_i \alpha_i F_i(\mathbf{x}) + \beta \mathcal{P}(\mathbf{x}), \\ F_i(\mathbf{x}) =& \frac{1}{2} \|\mathbf{A}_i \mathbf{x} - \mathbf{y}_i\|_2^2, \end{aligned} \tag{2.45}$$

where the hyperparameters α_i tune the weight or contribution of the penalty function associated to each individual camera, and also a prior term has been added for completeness. The gradient of objective function (2.45) is defined as the sum of the individual gradients

$$\nabla F(\mathbf{x}) = \sum_i \alpha_i \nabla F_i(\mathbf{x}) + \beta \nabla \mathcal{P}(\mathbf{x}). \tag{2.46}$$

Therefore the application of gradient descent for minimizing this kind of objective functions is straightforward, with the only inconvenience of having to tune the different hyperparameters.

Chapter 3

Time-resolved multispectral imaging for fluorescence imaging

This chapter discusses the physical basis of fluorescence and fluorescence imaging, including fluorescence lifetime imaging (FLIM). Also in this chapter, we present our contributions to perform time-resolved multispectral fluorescence imaging and fluorescence lifetime imaging by combining pixelated sensors with single-pixel cameras using data fusion.

3.1 Fluorescence

One of the fundamental mechanisms of light interaction with matter in general, and biological matter in particular, is luminescence [145–147]. The processes involved behind luminescence are shown in the Jablonski diagram of Fig. 3.1. Absorption of a photon can elevate an electron of a molecule from the ground state, S_0, to an excited state, S_n, in a process called excitation. Note that this excitation is not only caused by interaction with light, but can also be caused by mechanical or chemical mechanisms. The electron in the excited state can relax to the ground state by emitting another photon, heat, or both of them. If another photon is produced, the emission process is referred to as luminescence, which can be subdivided into fluorescence and phosphorescence, depending on the electronic states accessed and on the lifetime of the excited electron; otherwise, it is referred to as nonradiative relaxation. The lifetime is the average time the electron spends in the exited state before returning to the ground state. Once excited, the electron in the excited state S_n decays to the lowest vibrational energy level in the excited state S_1 via vibrational relaxation (also referred to as internal conversion). The timescale of this event is in the order of femtoseconds to picoseconds, and does not result in the emission of a photon as it is a nonradiative transition. From S_1, various transitions can be distinguished: internal conversion to S_0, fluorescence emision to S_0 (also including its vibrational states) with a lifetime in the order of nanoseconds, and intersystem crossing from the singlet to a triplet state T_1 with the subsequent phosphorescence emission to S_0. The transition to the metastable state, T_1, by intersystem crossing alters the electron spin. And as radiative de-excitation from T_1 to S_0 is spin-forbiden, emission occurs only when thermal energy raises the electron to a state where relaxation is

allowed. This fact makes phosphorescence temperature-dependent and exhibit very long lifetimes (in the order of miliseconds or longer).

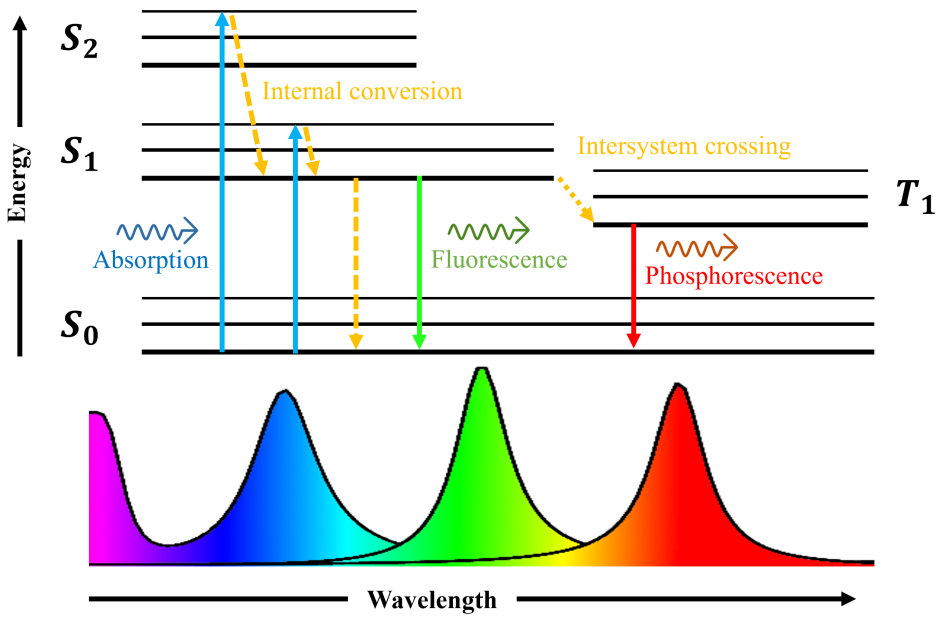

Figure 3.1: Jablonski energy diagram showing excitation and various possible relaxation mechanisms, including fluorescence and phosphorescence emission. An example spectra is shown to point out the shifts in wavelengths.

There are several characteristics to be pointed out from fluorescence emission. Due to energy loss between the absorbed photon and the emitted one after internal conversions, fluorescence is red-shifted relative to the excitation light, that is, fluorescence emission wavelength is usually higher than that of absorption. This is known as the *Stokes shift* [145–148]. Even if the initial excited state is related to the excitation wavelength, the transition to the lowest vibrational level of S_1 before fluorescence emission takes place makes the fluorescence emission spectrum show very little dependence on the excitation wavelength [146, 149]. For many fluorophores, the fluorescence spectrum is a mirror image of the absorption spectrum [146, 150]. Finally, fluorescence light is incoherent even if the excitation light is coherent because uncertain delays in the vibrational relaxations cause photons to be emitted at different times, usually spread over more than one period of the light wave [146].

After introducing several properties of fluorescence emission spectra and coherence, the next important characteristic to be understood is the temporal evolution of the emission, that is, how long after excitation does the emission process take place. Here we use a rate law for a first-order reaction to derive the temporal dependence of fluorescence excited by a very short light pulse. Assume we have a concentration C of molecules (measured in units of molecules/cm^3), and manage to excite a concentration C_0^* of them to an excited state with our pulse. Then by ignoring any intersystem conversion (and thus ignoring phosphorescence emission), and given the constant rates k_r and k_{nr} for radiative and non-radiative de-excitation, respectively, the concentration of molecules in the excited state C^* will vary in time according to:

$$\frac{\mathrm{d}C^*}{\mathrm{d}t} = -(k_r + k_{nr})C^*, \tag{3.1}$$

which can be solved to yield:

$$C^*(t) = C_0^* \exp(-t/\tau), \tag{3.2}$$

where we used the initial condition $C^*(t=0) = C_0^*$ and where we defined the lifetime τ of the excited state as:

$$\tau = \frac{1}{k_r + k_{nr}}. \tag{3.3}$$

The total radiated energy from these molecules during de-excitation will be proportional to the number of molecules inside the irradiated volume V and the radiative rate k_r:

$$P_{fluo}(t) = E_{em} k_r V C_0^* \exp(-t/\tau), \tag{3.4}$$

where E_{em} denotes the energy of the radiative transition. Thus fluorescence emission from excitation by a pulse follows an exponential decay in time, with a lifetime related to the radiative and non-radiative decay rates. The ratio of the number of photons emitted to the number of photons absorbed is referred to as *quantum yield*.

In single-point measurements, i.e., non-spatially resolved, fluorescence is a powerful tool to achieve information concerning molecular cell biology. Although the endogenous fluorescence (autofluorescence) properties of specific target molecules can be exploited to provide label-free molecular contrast in cell biology, the molecules of interest are typically tagged with exogenous labels such as fluorophores (fluorescent molecules) or nanoparticles for both detection of diseased tissue and therapeutic intervention [145, 151–154].

3.2 Fluorescence imaging

Imaging of fluorescence is mainly used to obtain information about localization, that is, to provide a mapping of fluorophore distribution and therefore of labelled proteins. But by using multiple fluorophores with different spectral properties, fluorescence imaging can also be used for co-localization of proteins within the spatial resolution of the imaging system. Also, as fluororescence is extremely sensitive to the local environment surroundings of the fluorophore, imaging can perform a sensing role.

Since the fluorescence process can be studied respect to the fluorescence intensity, excitation and emission spectra, quantum efficiency, polarization response, and fluorescence temporal trace or lifetime; fluorescence imaging is inherently a multidimensional imaging domain. These parameters depend on the properties of the fluorophores itself but are also affected by factors dependent on its local environment, such as local viscosity, temperature, refractive index, pH, calcium and oxygen concentration, electric field, etc., which change the molecular electronic configuration or the excitation and de-excitation pathways.

Fluorescence intensity imaging is probably the most straightforward technique. It allows to determine the spatial localization of fluorophores. However, merely spatial imaging of structures is not sufficient, and this information needs to be combined with spectral, time or polarization related information in order to probe structure and dynamics that provide useful information on biological functions.

Spectral information has always been valuable in fluorescence imaging as it allows the simultaneous use of more than one fluorescent marker and map their distribution

in different biological sites (tissue locations, organelles, etc.). Furthermore, one can probe information about the local environment by monitoring the spectral shift in the emission maximum or the change in the spectral profile of a fluorescent marker [145, 154].

Polarization is another dimension to take into account. It can readily be measured using polarized excitation sources and detectors sensitive to the state of polarization, and gives information about the rotational diffusion of molecules during the lifetime of the excited state, which is dependent on the size and shape of the molecules, and on the viscosity of the local environment. Usually, the sample is excited by a short (ps) polarized light pulse, and fluorescence intensities are measured parallel ($I_{||}$) and perpendicular ($I_{\perp}$) to the plane of incident polarized light. Then the anisotropy function is determined as

$$r(t) = \frac{I_{||}(t) - I_{\perp}(t)}{I_{||}(t) + 2I_{\perp}(t)}. \tag{3.5}$$

This anisotropy decreases exponentially from an initial value r_0 with the rotational diffusion time constant t_r according to $r(t) = r_0 \exp(-t/t_r)$, with t_r being in the order of picoseconds [155]. And as t_r is proportional to the viscosity of the environment, fluorescence polarization can be used to study viscosity of cells or their membranes [150, 154].

In addition to fluorescence intensity and spectra, fluorescence lifetime reveled to be an important parameter characterizing the interaction of a fluorescent molecule with its molecular and cellular environment. Fluorescence lifetime imaging microscopy, often abbreviated as FLIM, provides a spatial lifetime map of a fluorophore within a cell or a tissue. The use of fluorescence lifetime as an image contrast mechanism offers a great number of advantages over steady-state or intensity only fluorescence imaging [154, 156]:

- The fluorescence lifetime is a highly sensitive probe of the local environment.
- Fluorescence lifetimes are independent of the fluorescence intensity, concentration, and photobleaching of the fluorophore.
- Lifetime can be used to distinguish spectrally overlapping fluorophores, or to help distinguish a fluorophore that exhibits similar spectra but different lifetimes in different environments.

Generally, the time-resolved fluorescence intensity profile following instantaneous excitation will exhibit a mono- or an N-component multi-exponential decay that may be modelled as:

$$I(t) = \sum_{i=1}^{N} A_i \exp(-t/\tau_i) + \text{const}, \tag{3.6}$$

where each pre-exponential amplitude is the intensity at time zero for the i-th component. A mono-exponential ($N = 1$) describes the emission of a large ensemble of identical molecules (or a large number of excitations of the same molecule). And a multi-exponential describes the presence of multiple fluorophores species or different states of the same fluorophore arising from interaction with the local environment. There is a general rule stating that as more parameters (A_i and τ_i) are used to describe the fluorescent signal, a higher number of photons need to be detected to achieve an accurate measurement of them [154, 157, 158]. Thus, fitting

the fluorescent decay profile to a multi-exponential decay model requires increased measurement times, which is a problem in terms of temporal resolution for imaging dynamic samples, photobleaching or photodamage. Therefore in some applications it is preferable to approximate the multi-exponential profile with a single exponential decay model. And even though the resulting average lifetime does not provide the same information it can still be useful as it reflects changes in the decay times. The number of photons required to determine the parameters of a multi-exponential decay model can also be reduced by assuming *a priori* that some parameters, e.g. τ_i, take the same value in all the pixels of the image. This is widely known as global analysis [159].

FLIM techniques, and in general fluorescence lifetime measurement methods, can be categorized as time- or frequency-domain techniques, according to whether the fluorescence signal is measured as a function of time delay after a pulsed excitation or whether lifetime information is obtained from measurements of phase (attenuation and delay) between the fluorescent signal and a periodically modulated excitation source.

In the frequency domain, the simplest approach is to use a sinusoidally modulated excitation source (with frequencies of around 100MHz to provide ns lifetime resolution, or up to several GHz for ps resolution). This excitation will produce a fluorescent signal also with a sinusoidal modulation but with a different modulation depth and a relative phase delay. For a mono-exponential decay, by measuring the relative modulation, m, and the delay, ϕ, the lifetime can be determined using one of the following equations (or an average of both):

$$\begin{aligned} \tau_\phi =& \frac{1}{\omega} \tan(\phi), \\ \tau_m =& \frac{1}{\omega} \left(\frac{1}{m^2} - 1 \right)^{1/2} \end{aligned} \tag{3.7}$$

where ω is the angular frequency [154]. In the case of multi-exponential decay, the lifetime values from Eqs. (3.7) will differ, and excitation with a sum of sinusoidally modulated signal with different frequencies are needed to untangle the different lifetime values [154,160,161] Also the use of non-purely sinusoidal modulation allows to use all the harmonic Fourier frequencies that make up the signal to retrieve more information [154, 162]. The idea behind the time domain method is rather simple, is consists in using an ultrashort pulsed excitation source and to directly measure the temporal decay of the fluorescence signal.

Another categorization for time-resolved or fluorescence lifetime determination can be made according to the nature of detection. Here we can distinguish time-gated and photon counting detection. Gated detection determines the relative timing of the fluorescence compared to the excitation signal. In the case of time-domain measurements and a single-exponential decay model with known or zero background, the lifetime can be determined with only two time-gated measurements with the following analytical expression:

$$\tau = (t_2 - t_1) / \ln(I_1 / I_2), \tag{3.8}$$

where I_1 and I_2 are the accumulated photons for a duration of ΔT at times t_1 and t_2, respectively. This expression is referred to as rapid lifetime determination

(RLD) [154, 163, 164]. There are also analytical RLD expressions for the case of unknown background, which requires three gates, and bi-exponential decays, which require four gated measurements [154, 165, 166]. For more complex decay profiles, the fluorescence signal has to be obtained at a higher number of delays to obtain the full temporal profile and fit the curve to the multi-exponential model.

In photon counting techniques, detected photons are assigned to different time bins to build up histograms of the decay profile. They can further subdivided into single-photon counting techniques, such as time-correlated single-photon counting (TCSPC), and techniques that count more than one photon per excitation pulse, like high speed analog to digital converters (ADCs) or time-binning based techniques [150, 154, 167]. In TCSPC a detector converts a single photon to an electronic pulse and the TCSPC electronics records it arrival time with respect to the excitation pulse. This process is repeated many thousand times to create a histogram of photon arrival, showing their statistical intensity as a function of time. TCSPC is one of the most accurate methods of lifetime determination due to the shot noise-limited detection, a high photon economy, low temporal jitter, a high temporal precision (presenting a large number of temporal bins), and a high dynamic range. The major drawback is a low acquisition rate due to the necessity to operate at sufficiently low florescence flux levels to ensure single photon detection and avoid pulse pile up[1] [168]. In photon time-binning techniques, a histogram is build up by accumulating the photoelectrons arising from the detected photons in a number of different time bins [154, 169]. To obtain lifetime information, the histogram (representing the temporal decay profile) is fitted to the mono- or multi-exponential decay model, e.g. with a nonlinear least-squares Levenberg-Marquardt algorithm (similar to the one explained in section 2.2, but in this case not applied to images).

A further categorization of FLIM techniques can be made attending the extension of the excitation source. This way we can distinguish between wide-field and single-point scanning techniques. In wide-field imaging techniques a broad region of the sample is illuminated and detection is performed with a spatially resolved detector. On the other hand, single-point scanning imaging techniques use single-channel detection systems, i.e., without spatial resolution, and scan the sample point-to-point. Usually, wide-field FLIM is implemented with gated imaging detectors, such as streak cameras[2] , while point-scanning FLIM techniques make use of photon counting detectors to sample the fluorescence signal. Recently, development of arrays of single-photon avalanche diodes (SPADs) with TCSPC electronics for each individual pixel has made possible wide field imaging with photon counting detection. However these SPAD arrays suffer from a low pixel count and are therefore unsuitable for high resolution FLIM [171–174].

In the time domain, the scanning FLIM approach with TCSPC detection provides high-temporal resolution and the best lifetime estimation. However, due to the prolonged exposure time to achieve a sufficient photon count, a considerable light exposure is needed, which is undesirable due to photobleaching, photodamage or

[1] Pulse pile up refers to the problem of more than one photon arriving in a single-photon detection period, which results in inaccurate lifetime estimations.

[2] A streak camera is a device that measures very fast light phenomena by providing spatial and temporal (and even spectral) information. It works by accelerating and deflecting photoelectrons to separate them according to their arrival time [170]

phototoxicity. Light dose can be reduced, or at least spread over the whole image area, in the wide-field imaging approach by using sensitive imaging detectors.

The SPI technique described in the previous chapter enables imaging with a single-point detector without scanning the sample point-by-point by using structured wide-field illumination. Therefore, a SPC for time-resolved fluorescence imaging or FLIM combines advantages offered by wide-field illumination with the advantages of photon counting technologies (such as TCSPC): reduced light exposure per unit area and good temporal resolution for accurate lifetime estimation. Such systems have been recently developed by different groups [83, 175]. However, SPI is still bounded by a trade-off between acquisition speed and spatial resolution. Because SPI systems are sequential in nature, to achieve higher spatial resolution more masks need to be generated on the SLM to sample the scene, thus increasing light exposure time. This problem, together with the inherent high amount of data generated by a multidimensional imaging system such as time-resolved multispectral fluorescence imaging, tends to generate bottlenecks in acquisition, transmission, storage, and computational power, which limit the capability of such systems to perform in real time [176]. Signal processing techniques, such as compressive sensing, help alleviate the aforementioned data processing hurdles.

In this chapter, we describe a different and novel approach that combines the SPI and DF paradigms. The capture process is achieved using detectors that individually gather information about a reduced number of dimensions (space, time, and spectra). The system relies on the use of two different kind of cameras: low spatial resolution SPCs capturing multispectral and time-resolved information, and a conventional array detector capturing high spatial resolution images. After the measurement process, the individual 2D, 3D or even (low spatial resolution) 4D projections are merged in the final 4D hypercube. By doing so, it allows to capture high spatial resolution, multispectral, and time-resolved fluorescence images. This approach provides an efficient multidimensional imaging system that is not affected by bottlenecks in data transmission or storage limitations, as each individual sensor measures only a small fraction of the whole information.

Three different works based on the same idea will be presented in the next sections. All three of them share a similar experimental setup, based on the combined use of SPCs and conventional cameras. They differ based on whether they are implemented for macroscopic imaging or microscopy, structured illumination or detection, or on the number of different imaging devices that are fused. In the first one a system for multispectral and time-resolved macroscopic imaging is presented [177]. The second one implements the same idea to microscopy and exploits the additional use of CS to reduce the amount of measurements [178]. In the last one we introduce our idea to perform FLIM by introducing the multi-exponential decay model fitting into the DF process.

It is important to point out that while we developed our work on DF of SPCs and conventional cameras for multispectral and time-resolved fluorescence imaging, other groups have used similar DF-based approaches to create high-spatial-resolution time-resolved fluorescence imaging systems by combining SPAD arrays, which have inherently low spatial resolution, and conventional cameras [174, 179].

3.3 Time-resolved multispectral macroscopic fluorescence imaging

The system described in this work combines the images obtained with two SPCs with the image obtained with a CMOS cameras following the framework depicted in Fig. 3.2. Individually, each SPC provides multispectral or time-resolved images with low spatial resolution, while the CMOS sensor captures a high spatial resolution image of the sample, but neither spectral nor time-resolved. The aim is to use DF to combine these three images to acquire full 4D reconstructions (with two spatial dimensions, x and y, together with the spectral, λ, and temporal, t, dimensions) of a fluorescent sample with different fluorophore species.

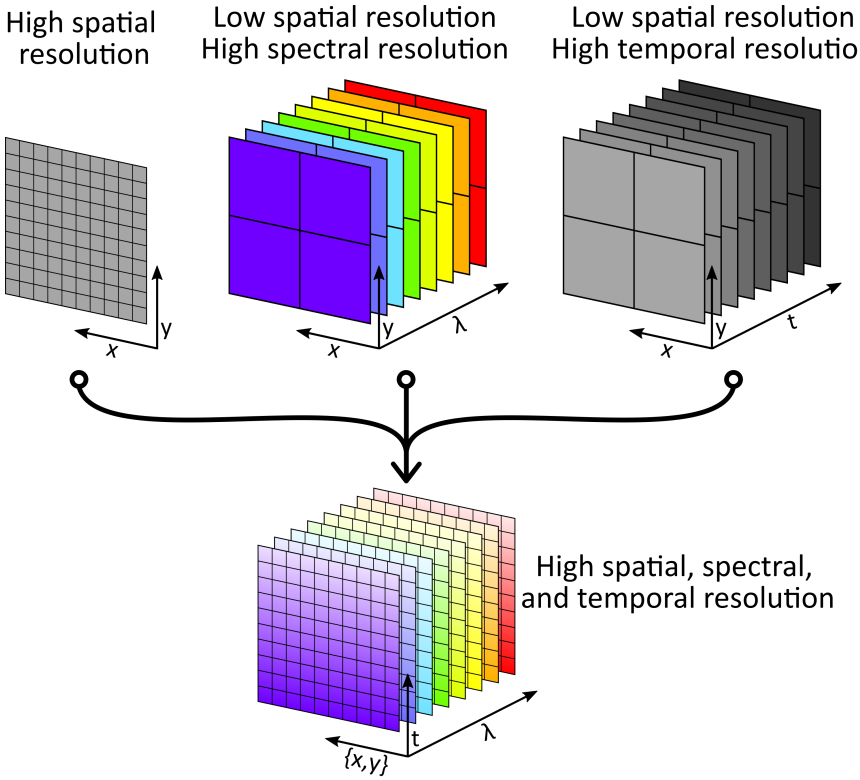

Figure 3.2: Spatiotemporal–spectral data fusion framework. A CMOS camera acquires a high spatial resolution image with neither temporal nor spectral resolution. A multispectral SPC acquires a low spatial, but high spectral resolution datacube, using a spectrometer as its detector. Last, an additional SPC measures a low spatial, but high temporal resolution datacube, using a fast bucket detector. All three datasets are combined via regularization to obtain a 4D high-resolution spatial, temporal, and spectral hypercube.

For each camera, we can formulate a forward model that represents the acquisition of a projection of the high-resolution 4D hypercube, denoted by $\mathbf{x}$, over several dimensions. The measurement for the CMOS camera is expressed as $\mathbf{y}_{cmos} = \mathbf{S}\,\mathbf{T}\mathbf{x}$, where $\mathbf{S}$ and $\mathbf{T}$ represent the spectral and temporal integration operators, respectively. $\mathbf{S}$ and $\mathbf{T}$, in combination, project $\mathbf{x}$ over the 2D space. The forward models for the two SPCs are formulated in a similar way. For the spectral SPC the forward model is given by $\mathbf{y}_{spec} = \mathbf{R}_L\,\mathbf{T}\mathbf{x}$, where $\mathbf{R}_L$ is the spatial downsampling operator. $\mathbf{R}_L$ projects a high spatial resolution image into the low resolution space, i.e., per-

forms a spatial downsizing to match the low spatial resolution of the SPC. Lastly, for the time-resolved SPC we have $\mathbf{y}_{temp} = \mathbf{R}_L\,\mathbf{S}\mathbf{x}$. Some insight about these operators is provided in Appendix A. Once we have formulated the different forward models, the problem then resides on finding an estimation of the hypercube, $\hat{\mathbf{x}}$, that is compatible with the three measurements. This is done by solving the problem of Eq. (2.44), where the objective function given by Eq. (2.45) is

$$\begin{aligned} F(\mathbf{x}) =& \frac{1}{2}\|\mathbf{S}\,\mathbf{T}\mathbf{x} - \mathbf{y}_{cmos}\|_2^2 + \frac{1}{2}\alpha\|\mathbf{R}_L\,\mathbf{S}\mathbf{x} - \mathbf{y}_{temp}\|_2^2 + \\ & \frac{1}{2}\beta\|\mathbf{R}_L\,\mathbf{T}\mathbf{x} - \mathbf{y}_{spec}\|_2^2. \end{aligned} \tag{3.9}$$

The first term in Eq. (3.9) minimizes the quadratic difference between the projection of the 4D hypercube over the full resolution 2D space and the image obtained with the CMOS camera. The second term minimizes the difference between the projection of the 4D hypercube over a low-resolution 3D space (x, y, t) and the measurement of the time-resolved SPC. The last term minimizes the difference between the projection of the 4D hypercube over a low-resolution 3D space (x, y, λ) and the multispectral SPC measurement. The hyperparameters α and β tune the relative weight of each data data fidelity term, and have been tuned to yield the best results. Note that no prior term was added[3]. Given the gradient of the objective function of Eq. (3.9),

$$\begin{aligned} \nabla F(\mathbf{x}) =& \mathbf{T}^\mathsf{T}\,\mathbf{S}^\mathsf{T}(\mathbf{S}\,\mathbf{T}\mathbf{x} - \mathbf{y}_{cmos}) + \alpha\mathbf{S}^\mathsf{T}\,\mathbf{R}_L^\mathsf{T}(\mathbf{R}_L\,\mathbf{S}\mathbf{x} - \mathbf{y}_{temp}) + \\ & \beta\mathbf{T}^\mathsf{T}\,\mathbf{R}_L^\mathsf{T}(\mathbf{R}_L\,\mathbf{S}\mathbf{x} - \mathbf{y}_{spec}), \end{aligned} \tag{3.10}$$

minimization is performed with a standard gradient descent algorithm with backtracking line search. The code is implemented in MATLAB and publicly available together with an example dataset [180].

The experimental implementation of the system is shown in Fig. 3.3. The excitation light source is a 40 MHz mode-locked supercontinuum fiber laser (Fianium, SC450, 6 ps pulsewidth) spectrally filtered thought a bandpass filter centered at 480 nm with 10 nm FWHM. The illumination area is $2.5 \times 2.5\,\mathrm{cm}^2$. On the detection side, we have the three detectors working simultaneously. The CMOS camera (Grasshopper GS3-U3-23S6M, Point Grey Research) is used to acquire an 512×512 px monochrome image of the sample ($\mathbf{y}_{cmos}$). In parallel, the sample is imaged onto the surface of a DMD (Discovery Kit 4100, Vialux), corresponding to a structured detection configuration. This DMD sequentially codifies a set of 2048 Walsh-Hadamard masks for SPI acquisition, to reconstruct 32×32 px images. In order to image simultaneously with both SPCs and speed-up acquisition, we use both reflection arms of the DMD in parallel. This also improves light efficiency as both reflection paths are used. In one reflection path, we place a time-resolved detector: a hybrid-PMT (HPM-100-50, Becker & Hickl) connected to a TCSPC board

[3]No prior was added because it was not needed in this experiment. Initially, we tried several priors, but we found that the algorithm converged to the same solution even without a prior. This is probably due to the well-behaved measurement, with little noise and with fluorophore species that are spatially separated.

(SPC-130-EM, Becker & Hickl), which provides photon time-of-arrival histograms on a temporal window of about 25ns, with up to 4096 time bins. Nonetheless, to reduce noise, binning of 16 time bins of the temporal trace is performed. The image provided by this time-resolved SPC ($\mathbf{y}_{temp}$) is a $32 \times 32 \times 256$ datacube (32×32 pixels with 256 time bins of 97.7 ps each). In the other reflection direction, we have a multispectral detector consisting in a spectrometer (Acton, sp-2151i, Princeton Instruments). The spectrometer includes a difraction grating (600 lines/mm) that disperses the light onto a 16-channel photo-multiplier tube (PMT, PML-16-C, Becker & Hickl). This multispectral SPC produced an image ($\mathbf{y}_{spec}$) consisting in a $32 \times 32 \times 16$ datacube (32×32 pixels with 16 spectral channels covering a range between 510 and 650 nm).

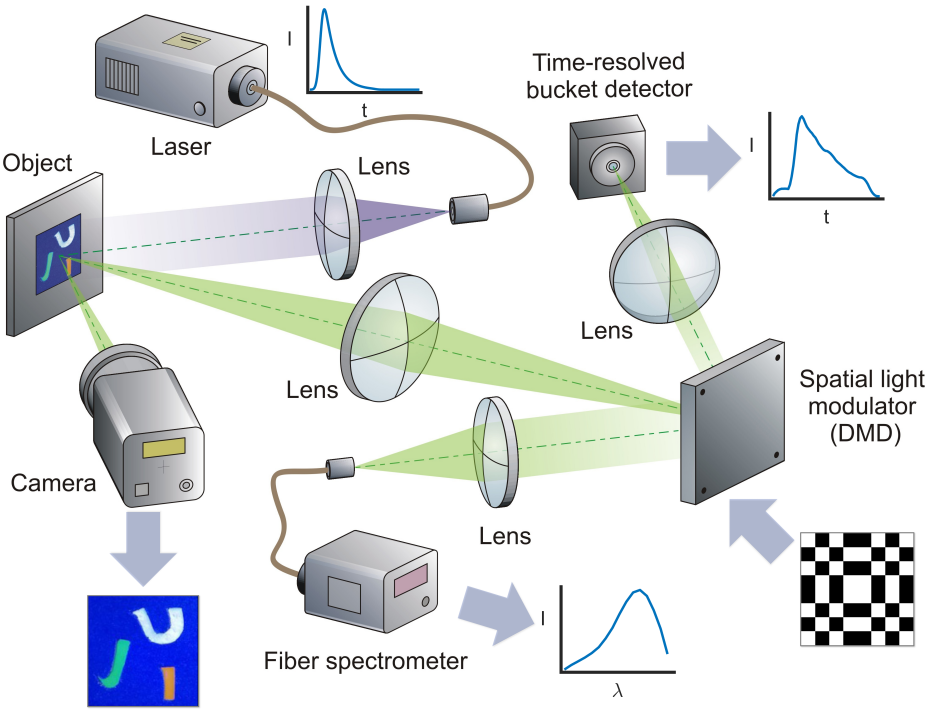

Figure 3.3: Experimental implementation of the multispectral time-resolved fluorescence imaging system that merges a conventional camera and two SPCs with DF. The object is illuminated in reflection geometry with a laser beam. The conventional camera records a high-resolution 2D image of the object. The object is also imaged on the DMD. A sequence of Hadamard patterns is codified on the DMD at a high frame rate. For each pattern, the light reflected by the DMD is collected in parallel by a time-resolved bucket detector and a spectrometer coupled with a detector array.

Both images from the multispectral and time-resolved SPCs share the same point view of the scene. Nonetheless, the CMOS camera sees the scene from another perspective. To overcome this problem, the CMOS image was aligned with the SPC images by means of image registration [181].

The imaged object is a macroscopic fluorescent sample with multiple fluorophore species. More specifically, it consists of a plaque with three letters (U,J, and I) forming a minimalist version of our university's statutory logo. The U character contains the 4-dicyanomethylene-2-methyl-6-p-dimethylaminostyryl-4H-pyran (DCM)

laser dye painted on white paper, while the J and I characters are made of fluorescent plastic slides, respectively emitting in the green and orange regions of the spectra.

The image acquired by the CMOS camera and the spatial projections of the multispectral and time-resolved images can be seen in Fig. 3.4. Insets show the spatial resolution at different points of the letters.

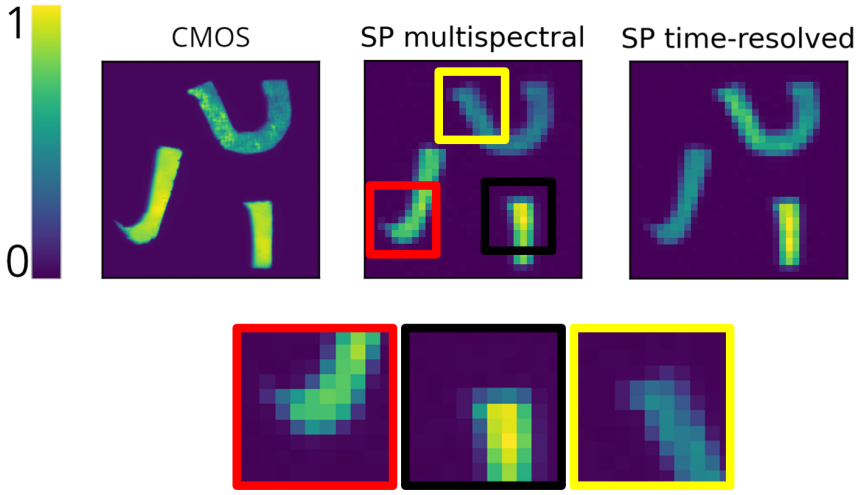

Figure 3.4: Representation of the three measured datasets. On the left the high-resolution image from the CMOS camera. In the middle the spatial projection of the multispectral SPC image. And on the right the spatial projection of the time-resolved SPC image. The three insets at different point of the characters show the spatial resolution of the SPC images.

After the acquisition, the three datasets were feed to the DF algorithm, where they were merged to generate a 4D hypercube of size $512 \times 512 \times 16 \times 256$ (which is approximately one giga-voxel). In fact, the measurements are only a very small fraction of the information contained by the reconstructed data. Considering the number of measured (M) versus the reconstructed (N) voxels, we can define a measurement ratio as $M.R. = M/N = \frac{512\times512+32\times32\times16+32\times32\times256}{512\times512\times16\times256} \approx 0.0005$. Visualizing this 4D information on a 2D medium such as this manuscript is tricky. Anyway, Fig. 3.5 shows our best attempt on visualizing the DF recovery provided by merging the three individual datasets. Here we have the spatial projection of the hypercube with the same insets as in Fig. 3.4 to highlight the increase in spatial resolution of the images when compared to the SPC images. In Fig. 3.5, we also show the temporal-spectral traces for different regions of the sample. With these 2D maps of time versus wavelength we can identify that the regions with the J and I characters present very similar temporal traces, but different spectral signatures; while the regions with the U and I characters have similar spectral signatures, but different temporal decays. Thus, by exploiting both spectral and temporal information, we can distinguish the three fluorescent species present in the sample. From the individual datasets alone, which lack combined spectral and temporal information, this classification could not be made. A visualization of the full reconstructed dataset can be done with a movie showing the temporal evolution of the 16 different spectral channels. This can be found in the visualization published together with the article [182].

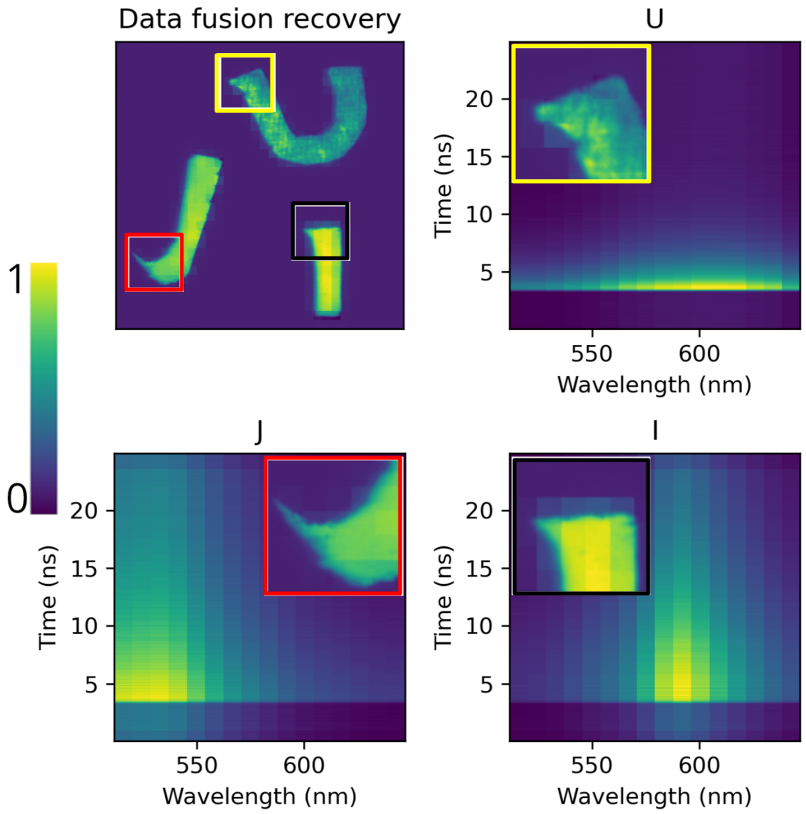

Figure 3.5: Results from the DF process. Spatial projection of the DF-recovered 4D hypercube and temporal-spectral traces for the different characters (averaged over multiple pixels for the U, J, and I characters) present in the sample. The insets show the increased spatial resolution when compared to the SPC datasets.

Although the improvement in spatial resolution might not seem so high, acquiring 512x512 pixel hypercubes solely with the SPCs would result in acquisition times that are 256 times longer due to the sequential nature of SPI (because more masks have to be scanned to obtain higher resolution). Also, DF between the two high-resolution 3D datasets would be needed to merge the temporal and spectral information. Finally, the measurement and reconstruction voxel ratio would also be higher: $M.R. = M/N = \frac{512\times512\times16+512\times512\times256}{512\times512\times16\times256} \approx 0.07$.

To further test the quality of the results, we compared the recovered spectra and fluorescence decay with reference measurements of the species present in the sample. The reference temporal traces were measured with a fast detector (1024 temporal bins of 24.4 ps each). The normalized data from the DF reconstruction and the reference measurements are shown in the top of Fig. 3.6. Each temporal trace is fitted to a mono-exponential decay. The lifetime values obtained from the DF reconstruction for the U, J, and I characters are $\tau_U = 2.07\,\text{ns}$, $\tau_J = 9.07\,\text{ns}$, and $\tau_I = 10.8\,\text{ns}$, respectively, which show very good agreement with the reference values for the three fluorophores. The spectral reference measurements were performed with a high-resolution spectrometer (Hamamatsu TM-VIS/NIR C10083CA-2100). The comparison with the spectral signatures of each of the three characters is shown in the lower half of Fig. 3.6, showing good agreement with the results from the DF.

3.4 Time-resolved multispectral fluorescence microscopy

Once we demonstrated the feasibility of the DF approach for macroscopic imaging, the next logical step was to use it to perform multi-dimensional fluorescence microscopy. While the main framework is the same, the application to microscopy, and specially to biological samples such as cells, entails obviously some changes in the experimental setup but also some challenges to overcome such as, for example, the greater complexity of the samples and measurements with lower SNRs. Unlike the sample used for our macroscopic imaging system, biological samples present more complex shapes, both in the spatial distribution of the fluorescence emission and in the shape of the spectro-temporal signal. Usually fluorophores with different decay times and different spectral signatures coincide at the same spatial position, resulting in complex spectro-temporal traces. On the other hand, lower excitation intensities have to be used to avoid photobleaching or photodamage, even more in microscopy where the light is concentrated in a smaller area. This results in weaker signals and therefore images degraded by noise.

Contrary to the previously described system for macroscopic fluorescence imaging, with a structured detection scheme and where two SPCs were employed, in this work, a single SPC in structured illumination configuration was employed to provide the spectral and temporal information in a 4D low-spatial-resolution dataset. The experimental setup is shown in Fig. 3.7. The excitation is performed with the same pulsed laser as in the previous experiment, but in this situation filtered by a band-pass filter centered at 520 nm (FB520-10, Thorlabs, 10 nm FWHM). Next, light is projected on a DMD (V-7000, Vialux). This scheme corresponds to a structured illumination configuration. The light modulated by the DMD is sent to the specimen

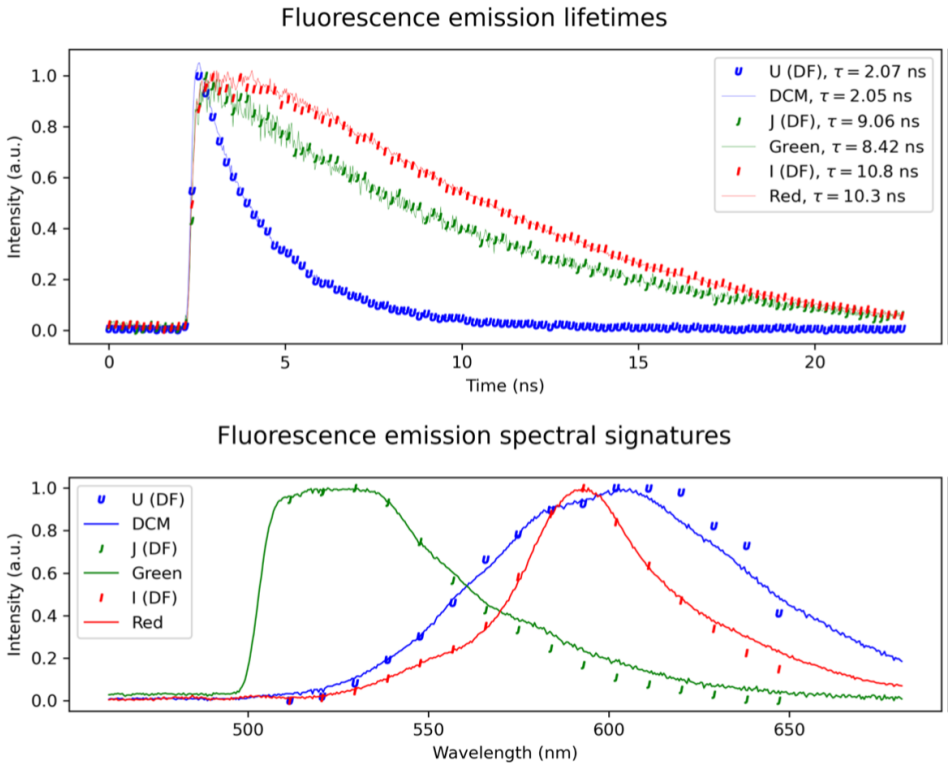

Figure 3.6: Temporal and spectral traces quality estimation. Temporal (top) and spectral (bottom) traces for the three species present in the sample (U, J, and I characters). Solid lines correspond to the reference temporal traces and spectral signatures present in the sample, while the markers correspond to the values extracted from our 4D reconstruction. To ease visualization, we show only one of every two intensity values recovered by the DF algorithm in the temporal traces. The legend of the top figure shows two lifetime values for each region or fluorophore, corresponding to the fit of the reconstructed and reference temporal traces.

by a tube lens ($f = 200\,\text{mm}$, AC508-200-A, Thorlabs) and a microscope objective (Plan N 40× NA=0.65 infinity corrected, Olympus). With the choice of this objective, and for modulations involving 512×512 DMD mirrors, the illuminated area of the sample, and thus the field-of-view (FOV), is about $150 \times 150\,\mu\text{m}^2$.

In the detection path, the fluorescence signal is selected with a long-pass filter at 550 nm (FELH0550, Thorlabs), and addressed to the same imaging spectrometer, coupled to the 16-channel PMT detector, as in the macroscopic setup. The signal from this detector is processed with the TCSPC board. By combining the structured illumination with this detector we are able to obtain a low spatial-resolution 4D dataset (denoted by $\mathbf{y}_{spc}$) of size $32\times32\times16\times256$ (32×32 pixels, 16 spectral channels which are tuneable to some extent over the 550-720 nm range, and 256 temporal bins of about 100 ps each). Nevertheless, to further reduce the number of measurements, CS with the TVAL3 algorithm is used to reconstruct a low-resolution image for each time bin and each spectral channel from an undersampled measurement with a scrambled Hadamard basis. Since the regularization is performed by minimizing the TV norm, no second basis is needed, i.e., the recovery basis is the canonical basis. A second purpose of using CS with TV-norm minimization is the reduction of noise in the images. As this SPC already provides full 4D information, but in low spatial-resolution, the forward model is formulated as $\mathbf{y}_{spc} = \mathbf{R}_L\mathbf{x}$. Also, the SPC features a non-mechanical zoom capability, which allows to reconstruct images in a region of interest (ROI) smaller than the FOV, and hence increasing spatial resolution, without changes in the optical setup. This works by codifying the same 32 x 32 pixel patterns with different numbers of micrromirrors in the DMD. For example, instead of using 512 x 512 micromirrors (16 x 16 micromirrors for each of the 32 x 32 pixels) we can use 256 x 256 micromirrors (involving 8 x 8 mirrors for each pixel) thus increasing lateral resolution in a factor of two.

Also in the detection path, with the help of a flip mirror, the scene is imaged on a 16-bit 512×512 cooled CCD camera (VersArray 512, Princeton Instruments). This camera is used to acquire the high-resolution image (256×256 pixels) of the sample, denoted by $\mathbf{y}_{ccd}$. The forward model for this camera is the same as in the previous system. This image is also used to create a mask in the spatial dimensions for $\mathbf{y}_{spc}$, based on a fixed threshold, to exclude noisy background pixels where no signal is expected based on the information provided by the high-resolution camera.

From the mathematical point of view, the fusion process of $\mathbf{y}_{spc}$ with $\mathbf{y}_{ccd}$, to reconstruct a high-resolution 4D hypercube, can be expressed as the minimization of the following objective function:

$$F(\mathbf{x}) = \frac{1}{2}\|\mathbf{S}\,\mathbf{T}\mathbf{x} - \mathbf{y}_{ccd}\|_2^2 + \frac{1}{2}\alpha\|\mathbf{R}_L\mathbf{x} - \mathbf{y}_{spc}\|_2^2 + \frac{1}{2}\beta\|\mathbf{R}_G\mathbf{x} - \mathbf{R}_g\mathbf{y}_{spc}\|_2^2, \qquad (3.11)$$

where the third least-squares term enforces a global fidelity of the time-spectra map by applying the operators $\mathbf{R}_G$ and $\mathbf{R}_g$, which perform a spatial integration over the high-resolution and low-resolution data cubes, respectively, to get a time-spectra map. The goal of this last term is to enforce the fidelity of the spectro-temporal information without additional enforcement of spatial similarity. A similar term was included in the objective function for DF in Ref. [174]. α and β are two hyperparameters that are manually tuned to find the best estimation. No prior was added to the objective function as the reconstruction of the images of SPC already

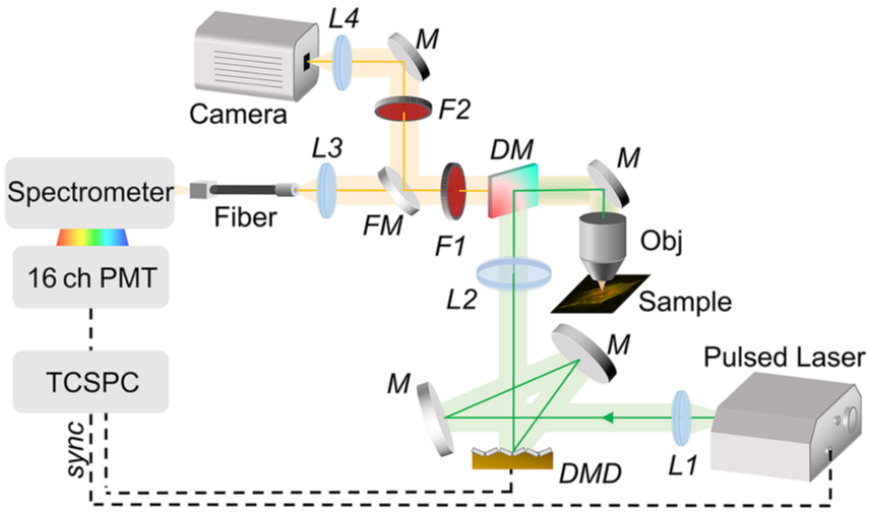

Figure 3.7: Optical scheme of the DF-based multispectral time-resolved fluorescence microscope. Structured illumination from a pulsed laser and a DMD is projected onto the sample with a tube lens and a microscope objective. The reflected light by the sample is either imaged by a CCD camera or integrated by a time-resolved multispectral single-pixel detector. This detector consists an imaging spectrometer coupled to a 16-channel PMT detector conected to a TCSPC board.

includes a TV-norm regularization. The gradient of this objective function is

$$\nabla F(\mathbf{x}) = \mathbf{T}^{\mathsf{T}}\,\mathbf{S}^{\mathsf{T}}(\mathbf{S}\,\mathbf{T}\mathbf{x} - \mathbf{y}_{ccd}) + \alpha\mathbf{R}_L^{\mathsf{T}}(\mathbf{R}_L\,\mathbf{x} - \mathbf{y}_{spc}) + \beta\mathbf{R}_G^{\mathsf{T}}(\mathbf{R}_G\mathbf{x} - \mathbf{R}_g\mathbf{y}_{spc}). \quad (3.12)$$

And minimization is performed through conjugate gradients with line-search.

Two different samples have been imaged with this system. The first one contains fluorescent beads (of $4\,\mu m$ of diameter) deposited on a microscope slide (FocalCheck F36909, Invitrogen). The beads are stained with four different fluorophores; although only two of them emit within the detection spectral window[4]. The second is a sample of fixed human embryonic kidney 293 (HEK-293, ATCC) cells. The cells are treated with poly (3-hexylthiophene-2,5-diyl) nanoparticles (P3HT NPs) (absorption at 500 nm and emission at 650nm), and their actin[5] filaments are stained with phalloidin conjugated to Alexa-Fluor 488 (ALF, absorption at 490 nm and emission at 520 nm, Sigma-Aldrich). The relevance of such samples resides in the nanoparticles's role at interfacing with living cell, as they can be used, for example, for cell stimulation, biosensing, and drug delivery [183–185].

For the sample with the beads, the image acquired by the CCD camera is shown on the left of Fig. 3.8(a). The figure on the right of 3.8(a) shows the spatial projection, i.e., integrated over the entire recorded spectra (550-690nm) and a temporal window of 10 ns from the temporal emission peak, of the SPC dataset. The image from the SPC shares the same FOV as the CCD camera. This dataset is reconstructed with the TVAL3 CS algorithm by using 307 of the 1024 patterns, which gives a compression ratio ($CR = 1 - M/N$) of 70%.

[4]It may appear illogical to use four different fluorophores for staining when only the emission of two of them can be measured, but the reason for this is that the sample was not specifically prepared for this imaging system.

[5]Actin is a family of proteins that form microfilaments in the cytoskeleton.

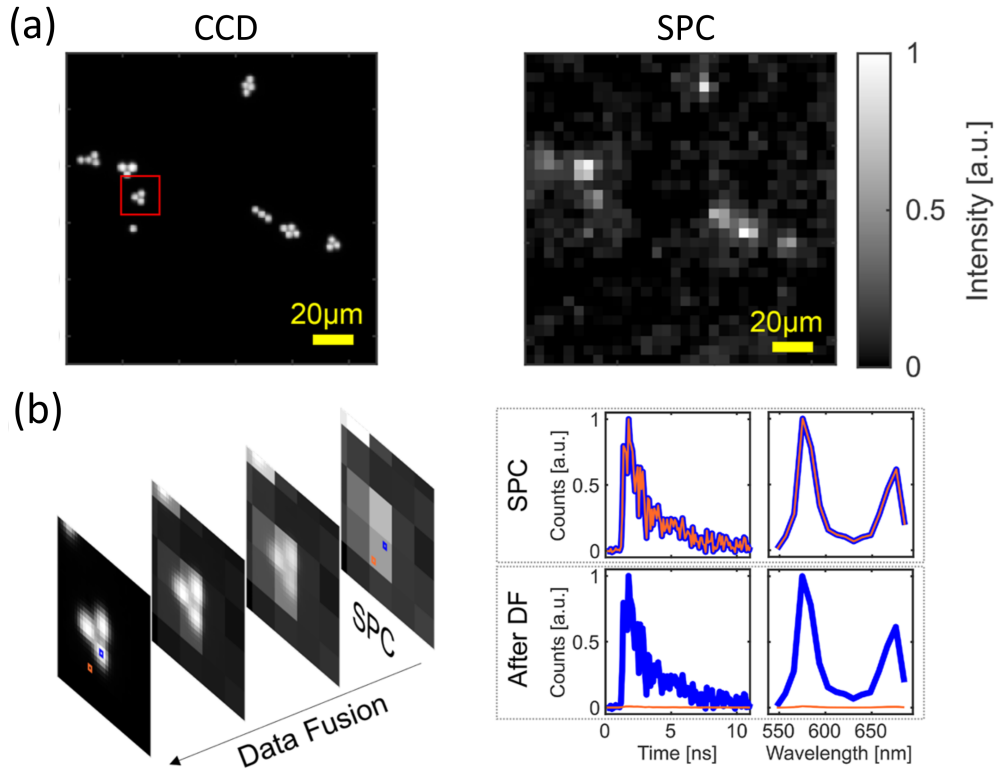

Figure 3.8: Datasets and results for the sample with the beads. (a) Left: Image from the CCD camera. Right: spatial projection of the SPC dataset acquired with CR=70%. (b) Left: Images from the ROI in red in (a) at different intermediate steps of the DF process. Right: Spectral and temporal traces from the blue and orange spots, before and after the DF process.

The results from the DF are shown in Fig. 3.8(b). On the left we have the reconstructed images at intermediate iterations of the DF process, which shows the increase in spatial resolution of the 4D hypercube. The shown images are from within the small area indicated by the red square in Fig. 3.8(a). On the right side of Fig. 3.8(b) we have the temporal traces and spectra of the two highlighted spots (blue and orange). Initially, the two spots contain the same spectral and temporal information as they belong to the same pixel of the low-resolution dataset. However, after the DF, these two spots correspond to different areas of the image. The orange spot lies in the background, while the blue one corresponds to a bead. Therefore, the temporal and spectral traces have changed: the temporal trace and spectral signature of the orange spot is flat, while the blue spot shows a defined spectrum and a temporal decay.

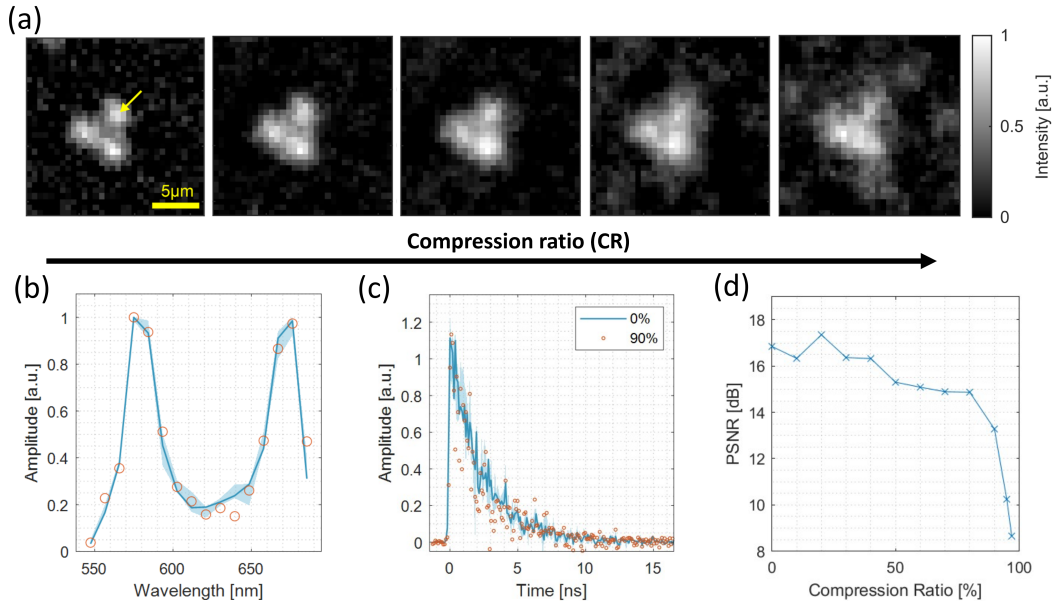

Figure 3.9: Study of the effect of compression on the quality of the reconstruction. (a) Images obtained with the SPC with the zoom feature within the red square of Fig. 3.8(a) for different levels of compression: CR = 0%, 60%, 80%, 90%, and 95%. (b) and (c) show the impact of compression on the quality of of the reconstructed spectra and temporal trace, respectively, from the area indicated by the yellow arrow in Fig. 3.9(a). (d) Analysis of the PSNR image quality metric for increasing CR.

Since temporal and spectral information is solely provided by the SPC, it is crucial to test how this information deteriorates with increasing compression. Figure 3.9(a) shows the images obtained with the zoom feature over a group of three beads within the read square of Fig. 3.8(a) for different levels of compression: CR = 0%, 60%, 80%, 90%, and 95%, respectively. The size of the zoomed area is about $20 \times 20\,\mu m^2$ by using only 64×64 micromirrors of the DMD (2×2 mirrors for each pixel). Hence, the pixel size of the zoomed image is about $0.6\,\mu m$, which is comparable to the spatial resolution achievable with the CCD camera. Obviously, the resolved spatial details decrease with increased CR, however, up to CR = 90% is is still possible to recognize the shape of the three beads. An analysis of the image similarity with the PSNR metric, with respect to the corresponding area of the CCD camera image as ground truth, is shown in Fig. 3.9(d). Here we can see that image

quality decreases drastically for CRs above $80-90\%$. The impact of compression on the quality of the reconstructed spectral and temporal information is analysed in Fig. 3.9(b) and (c). In these graphs we show the spectra and temporal trace from a ROI of 5×5 pixels centered around the bead indicated with a yellow arrow in Fig. 3.9(a), integrated over a 10 ns temporal window from the emission peak and integrated over the 560-600 nm spectral band, respectively. The solid lines represent the traces for the case of no compression, while the orange dots represent the traces at CR = 90%. The semi-transparent thick blue line represents the maximum fluctuations in the spectral and temporal traces for CRs from 10% to 80%. Also quantitative analysis of the similarity of the spectra for different CRs with respect to the uncompressed case were made with the mean squared error (MSE) metric. The results show that until CR = 90%, the MSE is less than 0.3%. Quantitative analysis of the temporal traces was performed by comparing lifetimes obtained from a mono-exponential fitting. Until CR = 80% the relative error in lifetime value with respect to the uncompressed case is less than 9%, and at CR = 90%, it is 11%. This analysis of the PSNR, MSE of the spectra, and estimated lifetime indicates that CR = 90% is the highest acceptable compression level for this dataset.

Next we imaged the sample with ALF-stained and P3HT treated HEK cells. The wide FOV CCD camera image is shown in Fig. 3.10(a). The SPC dataset (of 32×32 spatial pixels) is acquired over the same FOV, over a spectral range from 580 to 720 nm, and with CR = 80% (205 masks). The dataset integrated over the spectral dimension and 10 ns from the temporal fluorescence peak is shown in Fig. 3.10(b). These datasets are fed into the DF algorithm to obtain a high-resolution hypercube.

The spectra and lifetime of the ALF fluorophore and the P3HT nanoparticles were previously characterized. ALF, when described by a mono-exponential, has a lifetime of about 3.14 ns and P3HT presents a lifetime shorter than 200 ps. Therefore, as a result of this preliminary characterization, ALF can be highlighted by selecting a spectral band between 580 and 595 nm and a time gate of 7 ns. Likewise, P3HT nanoparticles can be underlined with a spectral band between 650 and 700nm and a shorter time gate of 1 ns. Applying these time gates and spectral filters we can separate the emission from the ALF stained actin filaments and the P3HT nanoparticles. Representation of this information in a single synthetic RGB rendered image is reported in Fig. 3.10(c). This image allows us to localize the parts with actin filaments (yellow areas) and the aggregates of P3HT nanoparticles (red spots) within the cell.

Even if the spatial resolution is increased by DF of the 4D SPC dataset with the CCD camera image, the low resolution of the SPC dataset still limits the final achievable resolution. Therefore, to increase the spatial resolution and to discriminate smaller structures within the cell, e.g., smaller P3HT nanoparticle clusters, SPC was repeated in a smaller FOV (shown in the inset of Fig. 3.10(b)) by using the zoom feature. This new FOV is of size $40\times40\,\mu\text{m}^2$, and was measured with only 77 masks of 16×16 pixels (CR = 70%). This new SPC dataset is merged with the corresponding area of the CCD camera. The resulting time- and spectra-integrated image is shown in Fig. 3.10(d). Two regions were selected (orange and blue circles), two show the spatially averaged spectral (Fig. 3.10(e)) and temporal (Fig. 3.10(f)) traces. While the emission spectrum of the blue circled area clearly shows a strong emission towards the lower end of the measured range, compatible with ALF, the

emission spectra of the orange circled area does not allow us to deduct the content. However, the temporal profile shows the presence of a short lifetime, corresponding to the presence of P3HT. Therefore, this set of measurements demonstrated the capability of the setup to discriminate between fluorophores based on the spectral and temporal information.

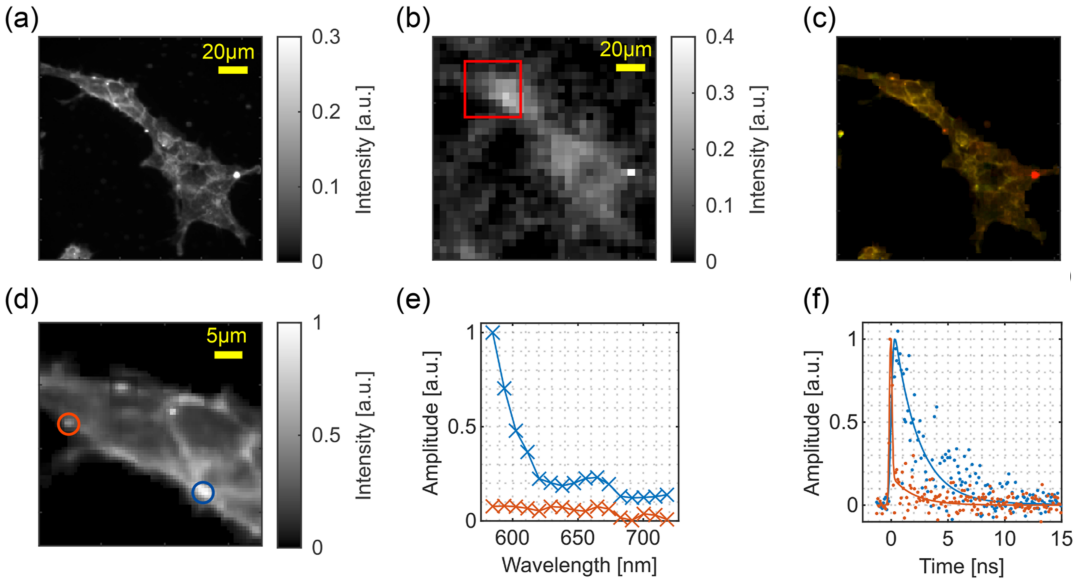

Figure 3.10: Datasets and results for the HEK cell sample. (a) High-resolution image from the CCD camera. (b) Low-resolution image from the spatial projection of the SPC dataset acquired with CR=80%. (c) RGB rendering of the selectively filtered hypercube to distinguish the emission from the ALF stain from the emission from the P3HT NPs. (d) Fusion of a SPC dataset acquired in the ROI marked by the red square in (b) with the zoom feature and the corresponding area of the CCD camera image. (e) and (f) show the spectral signatures and temporal traces, respectively, of the regions highlighted with orange and blue circles in (d).

In this section we have shown the application of DF and SPI for fluorescence microscopy. Instead of employing two SPCs, one for the time-resolved images and another one for the spectral images, in this work a single SPC acquiring low-resolution 4D information was used. The fusion with the high-resolution image from the conventional camera therefore serves to increase the spatial resolution. In addition, CS has been used to reduce the acquisition time of this camera, which was the most limiting factor regarding acquisition speed, by up to 90%. This approach is crucial when a short measurement time is needed to avoid photobleaching and cell damage, or to capture dynamic phenomena.

3.5 Multispectral fluorescence lifetime imaging

Fluorescence lifetime imaging consists in obtaining images of the fluorescent lifetime distribution, rather than the temporal evolution of fluorescence intensity. The classical approach is to obtain the full temporal information (which can be as low as only two time gates for a mono-exponential behaviour) and then to retrieve the lifetimes, usually by a fitting operation. In this sense, in both previous presented

works, this could have been performed after obtaining the high-resolution, multispectral, and time-resolved 4D hypercube. This process would entail reconstructing the whole temporal information for every pixel of the high-resolution space, and for every spectral channel; and afterwards fitting all these temporal profiles to a mono- or multi-exponential decay model. But one might ask if it is really necessary to reconstruct the whole temporal trace for the high number of pixels. Usually the number of different fluorophores is limited, and so is the number of different lifetimes. Let's take the hypercube of the macroscopic fluorescence imaging system as an example. In this case we have 512×512 pixels, 16 spectral channels and 256 temporal bins. This results in a hypercube with $512 \times 512 \times 16 \times 256 \approx 1.07 \cdot 10^9$ voxels and roughly 8.5 gigabytes (and exactly 8 gibibytes) of data. However, the number of different lifetimes is three. As such, and supposing that different fluorophores can spatially overlap, each temporal trace can be modeled with a tri-exponential decay, that is, with 7 parameters (the three lifetimes with their amplitudes and a constant); and the whole hypercube can be described by $512 \times 512 \times 16 \times 7 \approx 29.4 \cdot 10^6$ voxels (roughly 234.9 megabytes).

As a result, by adding a multi-exponential decay model fitting to the DF reconstruction process, we can achieve a great reduction of the size of the reconstructed hypercube. Also a desirable side effect of this fitting procedure is that, instead of reconstructing a noisy temporal trace, it finds the parameters that best suit the trace; which can be seen as having a denoising effect on the temporal information. However, it should be recalled that the multi-exponential fitting is not very robust to noise, in the sense that as noise increases the estimated lifetimes fluctuate drastically.

This new procedure only changes the algorithmic part, and not the acquisition step. Therefore, we will use this DF procedure with multi-exponential decay model fitting with the same or similar acquired datasets as in the two previous experiments. As these datasets are acquired either with three or two detectors the mathematical formulation of the procedure is slightly different in both cases (similarly as in the standard DF process).

In both cases the reconstructed hypercube is divided in two parts: $\mathbf{x} = [\mathbf{x}_A, \mathbf{x}_K]$, where $\mathbf{x}_A$ and $\mathbf{x}_K$ are the multispectral images for the decay amplitudes and decay rates, respectively. The decay rate is defined as the reciprocal of the lifetime $k = 1/\tau$. The number of lifetimes or decay rates, denoted by N_τ, is estimated by performing the singular value decomposition (SVD) of the temporal dataset rearranged in a matrix so that the temporal trace of each spatial position (and, if applicable, for each spectral bin) is a row of this matrix. An example of such matrix is shown in Fig.3.11(a), which is the rearranged temporal SPC dataset from the macroscopic imaging system. What is interesting of the SVD, is that we can clearly see that the singular values decay rapidly (see Fig. 3.11(b)). The physical meaning of this distribution is that there is a limited number of different temporal traces, and therefore a limited number of different lifetimes. In the example we have about three, so for each spatial position (and each spectral bin, if applicable) we have either one of the lifetimes or a combination of them. A coarse estimation of the lifetimes, used to create the initial guess for the algorithm, is made by assuming a global analysis approach, that is assuming the same lifetimes in all spatial positions and for all wavelengths, and performing a fitting of the temporal SPC dataset.

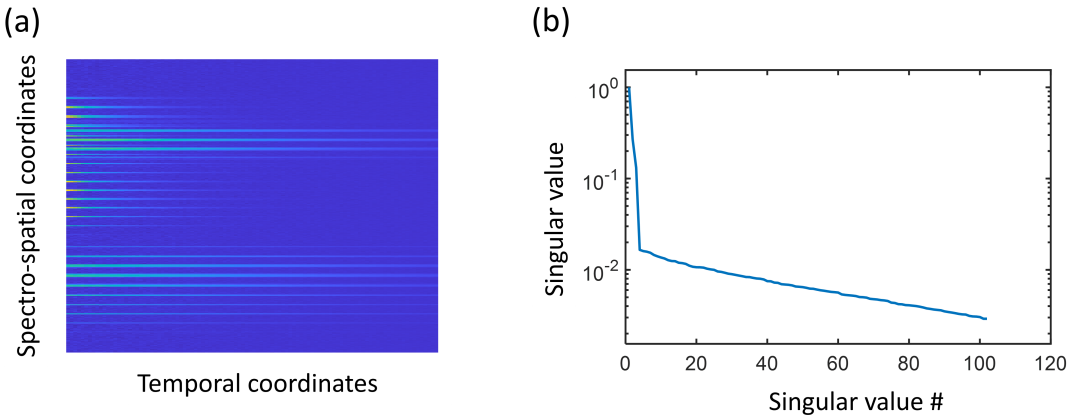

Figure 3.11: Example of the SVD-based procedure to estimate the number of different lifetimes present in the sample, in this case with the time-resolved SPC dataset from the macroscopic fluorescence imaging system (the UJI dataset). (a) Temporal dataset expressed in matrix form. Each spatial position corresponds to a row of the matrix, and the columns contain the temporal trace for each pixel. (b) Plot of the singular values obtained with the SVD of the matrix despicted in (a). The singular values after the thrid one are almost negligible, indicating that there are basically just three different temporal traces in the sample.

The DF problem with multi-exponential decay fitting for the first sample, the one with three measured datasets, is formulated as minimization of the following objective function:

$$\begin{aligned} F(\mathbf{x}) =& F(\mathbf{x}_A, \mathbf{x}_K) = \\ & \frac{1}{2}\|\mathbf{S}\,\mathbf{T}\,\mathbf{M}(\mathbf{x}_A, \mathbf{x}_K) - \mathbf{y}_{cmos}\|_2^2 + \frac{1}{2}\alpha\|\mathbf{R}_L\,\mathbf{S}\,\mathbf{M}(\mathbf{x}_A, \mathbf{x}_K) - \mathbf{y}_{temp}\|_2^2 + \\ & \frac{1}{2}\beta\|\mathbf{R}_L\,\mathbf{T}\,\mathbf{M}(\mathbf{x}_A, \mathbf{x}_K) - \mathbf{y}_{spec}\|_2^2, \end{aligned} \tag{3.13}$$

where $\mathbf{S}$, $\mathbf{T}$ and $\mathbf{R}_L$ are the linear operators that have already been introduced, and where $\mathbf{M}$ is a non-linear operator that creates the temporal traces from the decay rates and their amplitudes assuming a multi-exponential decay model. That is, given a set of parameters $\{A_i, k_i\}_i^{N_\tau}$ for a certain pixel and spectral bin, this operator creates the trace $\sum_i^{N_\tau} A_i \exp(-k_i t)$.

Because of the non-linearity of this latter operator, the whole inversion process is implemented as a non-linear least squares problem. However, solving this minimization problem for the complete space of parameters $\mathbf{x}$, i.e., simultaneously for both the amplitudes and decay rates, is very inefficient and presents a high probability of getting stuck in a local minimum instead of finding the global one. Therefore, in order to tackle these problems, the separability of operator $\mathbf{M}$ into a linear and a non-linear operator is exploited, similar to the variable projection method [186–188]. Following this premise, we have that $\mathbf{M}(\mathbf{x}_A, \mathbf{x}_K) = (\mathbf{A}\mathbf{x}_A)\,\mathbf{E}(\mathbf{x}_K)$, where $\mathbf{A}$ is the linear operator associated to the amplitude space, and $\mathbf{E}$ is the non-linear operator in the decay rate space that constructs the exponential decay for every entry of $\mathbf{x}_K$.

The separability of operator $\mathbf{M}$ and the partitioning of the parameters ($\mathbf{x}$) in

a linear ($\mathbf{x}_A$) and a non-linear ($\mathbf{x}_K$) part allows the minimization problem to be separable. That is, we can perform optimization in each reduced space separately. In this sense, we can solve

$$\hat{\mathbf{x}}_A = \arg\min_{\mathbf{x}_A} F(\mathbf{x}_A, \mathbf{x}_K), \tag{3.14}$$

for fixed $\mathbf{x}_K$, and

$$\hat{\mathbf{x}}_K = \arg\min_{\mathbf{x}_K} F(\mathbf{x}_A, \mathbf{x}_K), \tag{3.15}$$

for fixed $\mathbf{x}_A$. This gives rise to the double gradient descent approach presented in Algorithm 2. In this iterative minimization process we alternate between steps that minimize the objective function with respect to $\mathbf{x}_A$ and $\mathbf{x}_K$. Further gradient descent acceleration and step size computations are omitted in Algorithm 2 for simplicity. An appropriate stopping criteria for both the outermost loop and the nested loops for the reduced spaces is a change in the objective function smaller than some threshold. Obviously the threshold should be different on each loop.

Algorithm 2: Double gradient descent algorithm for minimizing an objective function with alternating steps in the reduced parameter spaces.

Result: Returns the estimated $\hat{\mathbf{x}} = [\hat{\mathbf{x}}_A, \hat{\mathbf{x}}_K]$ by minimizing a two variable objective function $F(\mathbf{x}) = F(\mathbf{x}_A, \mathbf{x}_K)$ by taking alternating steps in each reduced parameter space.

Initialize $\hat{\mathbf{x}}_{A,0}$ and $\hat{\mathbf{x}}_{K,0}$
Set $i = 0$ and $j = 0$
while *global stopping criterion unfulfilled* **do**
  while *A-subspace stopping criterion unfulfilled* **do**
    Calculate gradient: $\mathbf{g}_{A,i} = \nabla_{\mathbf{x}_A} F(\hat{\mathbf{x}}_{A,i}, \hat{\mathbf{x}}_{K,j})$
    Update $\hat{\mathbf{x}}_{A,i}$ in the direction provided by $\mathbf{g}_{A,i}$:
    $\hat{\mathbf{x}}_{A,i+1} = \hat{\mathbf{x}}_{A,i} - \tau_A \, \mathbf{g}_{A,i}$
    $i = i + 1$
  end
  while *K-subspace stopping criterion unfulfilled* **do**
    Calculate gradient: $\mathbf{g}_{K,j} = \nabla_{\mathbf{x}_K} F(\hat{\mathbf{x}}_{A,i}, \hat{\mathbf{x}}_{K,j})$
    Update $\hat{\mathbf{x}}_{K,j}$ in the direction provided by $\mathbf{g}_{K,j}$:
    $\hat{\mathbf{x}}_{K,j+1} = \hat{\mathbf{x}}_{K,j} - \tau_K \, \mathbf{g}_{K,j}$
    $j = j + 1$
  end
end

The operator $\mathbf{M}$ creates a $n \times n \times N_\lambda \times N_t$ hypercube, where n is the number of pixels of the rows and columns (N is used to denote the total number of pixels $N = n^2$), N_λ is the number of spectral channels and N_t is the number of time bins in the measured dataset. This is highly inefficient and slows down the calculations. Therefore, in the two terms that minimize the quadratic differences with the conventional camera and the spectral SPC, the combination of operators $\mathbf{T}\,\mathbf{M}(\mathbf{x}_A, \mathbf{x}_K)$ is substituted by another operator $\mathbf{D}(\mathbf{x}_A, \mathbf{x}_K)$. This new operator performs the integration over the temporal dimension of the temporal trace for each pixel. That is, on a set of parameters $\{A_i, k_i\}_i^{N_\tau}$, the operator $\mathbf{D}$ performs the operation $\sum_j^{N_t} \sum_i^{N_\tau} A_i \exp(-k_i t_j) = \sum_i^{N_\tau} A_i [1 - \exp(-k_i t_f)]/\Delta t \, k_i$, where Δt is the width

of each time bin, and t_f is the total length of the integrated time window. This way we avoid calculating the whole temporal hypercube.

For the remaining term of the objective function, the data fidelity term with the temporal SPC, another trick can be applied to reduce computational cost. Even if the linear operators ($\mathbf{R}_L$ and $\mathbf{S}$) do not strictly commute with the non-linear one ($\mathbf{M}$), they can be applied directly to $\mathbf{x}_A$ and $\mathbf{x}_K$ to produce low spatial resolution spectral-integrated images of the fluorescence amplitudes and decay rates. Then applying the operator $\mathbf{M}$ afterwards is less computationally demanding. However, this trick comes at the expense of a less accurate reconstruction because the operators do not actually commute.

On one hand, the gradient of the linear part, $\nabla_{\mathbf{x}_A} F(\hat{\mathbf{x}}_A, \hat{\mathbf{x}}_K)$, can be calculated with its analytic expression. On the other hand, the gradient of the non-linear part, $\nabla_{\mathbf{x}_K} F(\hat{\mathbf{x}}_A, \hat{\mathbf{x}}_K)$ could be calculated by computing the Jacobian. However, we exploited another approach where the non-linear gradient is calculated numerically using automatic differentiation (AD, for more information see Appendix B).

For the case of the macroscopic UJI dataset, the CMOS camera image was resized to 128×128 pixels (shown in Fig. 3.12(a)) for convenience. The number of different lifetimes was estimated with the SVD (see Fig. 3.11) to be around three, which also agrees with the knowledge we have about the sample. Therefore a total number of three decay rates and four amplitudes (one for each decay rate and one for the constant background) were retrieved for every pixel and spectral channel. Consequently the reconstructed hypercubes, $\mathbf{x}_A$ and $\mathbf{x}_K$, are of size $128 \times 128 \times 16 \times 4$ and $128 \times 128 \times 16 \times 3$, respectively.

Fidelity of reconstructed data with respect to the measured datasets is depicted in Fig. 3.12(b)-(d). Figure 3.12(b) shows the spatial projection of the reconstructed hypercubes obtained by the operation $\mathbf{S}\,\mathbf{D}(\mathbf{x}_A, \mathbf{x}_K)$. Figure 3.12(c), shows the temporal traces from the U, J and I characters, and from the background, both from the temporal SPC dataset and from the time-resolved reconstruction, obtained by $\mathbf{S}\,\mathbf{M}(\mathbf{x}_A, \mathbf{x}_K)$. Finally, in Fig. 3.12(d) we have the spectral signatures of the characters and the background, both from the measured spectral SPC and the time-integrated reconstruction obtained by $\mathbf{D}(\mathbf{x}_A, \mathbf{x}_K)$. While there is an almost perfect spatial and spectral reconstruction, the temporal part shows some discrepancy. More specifically the temporal trace for the I character shows greater differences at early times, resulting in an underestimation of the corresponding lifetime. This behavior is caused by the flattened peak of the measured temporal trace due to experimental conditions, which cannot be modeled by a multi-exponential decay.

The reconstructed lifetime image for every spectral channel is presented in Fig. 3.13. These images are obtained by applying a binary mask, resulting from thresholding the corresponding amplitudes ($\mathbf{x}_A$), onto the reciprocal decay rate hypercube ($\mathbf{x}_K^{-1}$), and superimposing (adding) all the lifetime channels. The J character presents a lifetime value of around 9-10 ns, and is mostly present in the lower half of the measured spectral window, vanishing as its amplitude decreases for higher wavelengths. The U character displays a lifetime value of around 2 ns, and is present for the whole spectral window as it presents a flatter spectral signature. Lastly, the I character presents a lifetime value of approximately 10 ns, and is mostly present at wavelengths between 566 and 629 nm. In summary, the three characters with

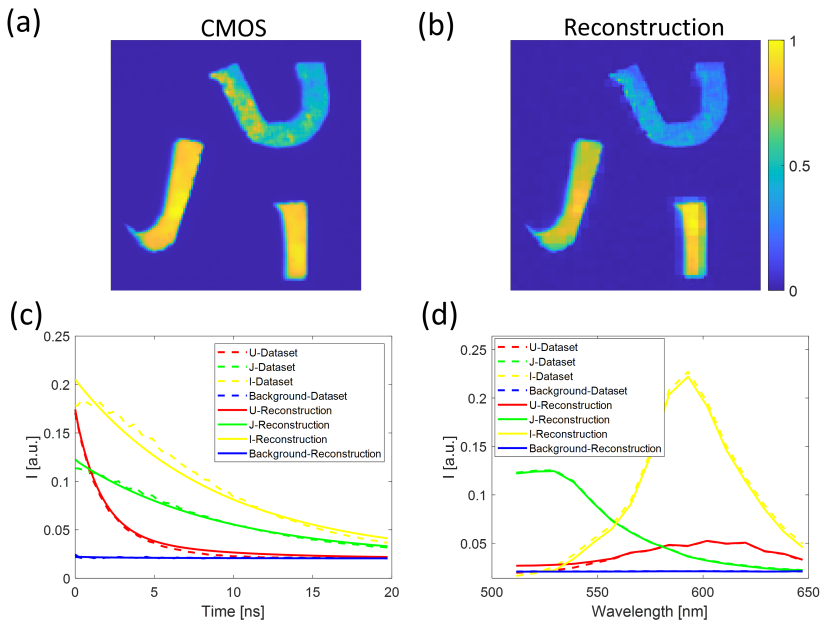

Figure 3.12: (a) CMOS camera image resized to 128×128. (b) Projection over the spatial dimension of the reconstructed hypercubes obtained by the operation $\mathbf{S}\,\mathbf{D}(\mathbf{x}_A, \mathbf{x}_K)$. (c) Comparison of the temporal traces for the different characters from the SPC dataset and from the reconstructed hypercubes. (d) Comparison of the spectral signatures for the different characters from the SPC dataset and from the reconstructed hypercubes.

different fluorophore species show lifetime values consistent with the previous characterization presented in section 3.3. Also the spectral behaviours agrees with the measured spectra.

Next, we tried to apply the same idea to a dataset acquired with the microscopy system. The two main differences between this case and the previous one lies in the number of datasets and the SNR of the measurements. While in the UJI macroscopic dataset there are three datasets (one for high spatial resolution, one for the temporal information, and one for the spectral information), with the microscopy system there are only two dataset to be fused (one for the spectro-temporal information and one for the increase in spatial resolution). Also, the level of noise in the temporal dimension is much higher for the SPC dataset of the microscopy system (e.g., compare the temporal traces from Figs. 3.6 or 3.12 with the traces from Figs. 3.8, 3.9, or 3.10). The presence of noise in the temporal traces hinders the task of finding the correct lifetime values of a multi-exponential decay model.

The imaged sample consists of a prepared microscope slide containing bovine pulmonary artery endothelial (BPAE) cells (FluoCells Prepared Slide #1 BPAE cells, F36924, Invitrogen). In this sample MitoTracker Red CMXRos (excitation at 579 nm and emission at 600 nm) was used to stain the mitochondria, actin was stained with Alexa Fluor 488 phalloidin, and the nuclei were counterstained with the blue-fluorescent DNA stain DAPI (excitation at 358 nm and emission at 461 nm).

The measured two datasets are represented in Fig. 3.14. Figure 3.14(a) shows the 256×256 pixel CCD camera image. Figure 3.14(b) shows the spatial projection, i.e.

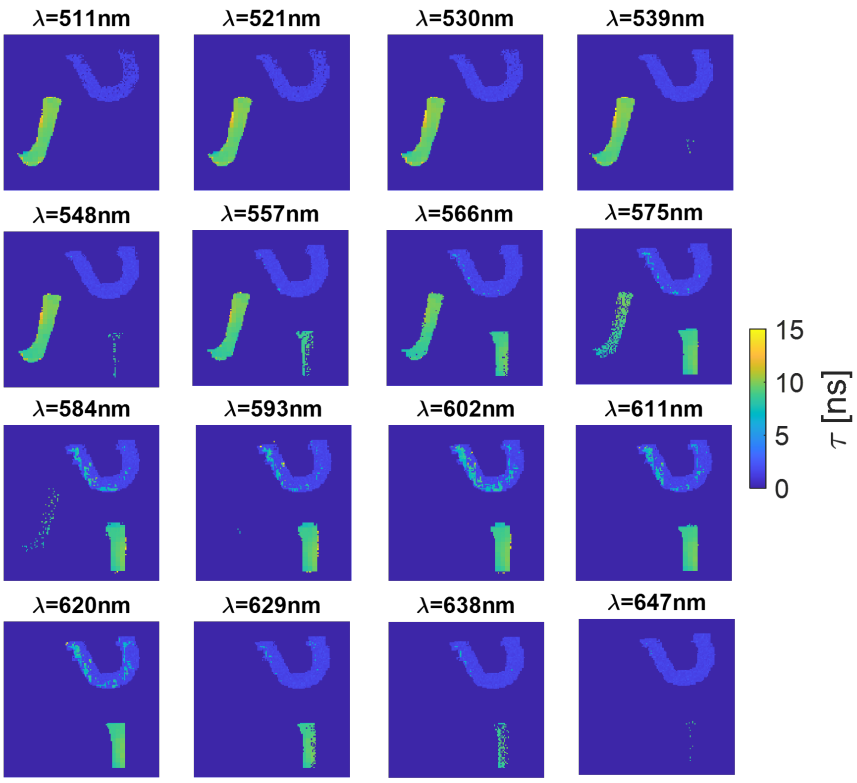

Figure 3.13: Lifetime images for every spectral channel of the UJI datasets.

integrated over the entire temporal spectral dimension, of the 4D ($32 \times 32 \times 16 \times 128$) SPC image. Figures 3.14(c) and 3.14(d) show the same SPC image integrated over the entire temporal dimension, but integrated for $\lambda < 575\,\text{nm}$ and $\lambda > 575\,\text{nm}$, respectively. The detected spectral window is in the range $547 - 685\,\text{nm}$. Due to the excitation wavelength centered at 520 nm, the DAPI fluorophore is not excited in this experiment, but the position of the nucleus is revealed by the absence of signal in the center of the cell. Figure 3.14(c), which is integrated for the lower end of the measured spectrum, reveals the position of the actin filaments of the cytoskeleton, while Fig. 3.14(d) reveals the areas with the presence of mitochondria due to the reddish emission of the MitoTracker Red CMXRos fluorophore.

Note that the SPC image (Fig. 3.14(b)) has a noisy background, so a binary mask calculated from thresholding the high-resolution image (Fig. 3.14(a)) is superimposed on the SPC image to avoid reconstruction artifacts. The SVD analysis of the rearranged SPC dataset yields the value $N_\tau = 4$. Therefore, three decay rates and four amplitudes were retrieved for each pixel and spectral bin, and the resulting hypercubes, $\mathbf{x}_A$ and $\mathbf{x}_K$, are of size $256 \times 256 \times 16 \times 4$ and $256 \times 256 \times 16 \times 3$, respectively.

The gradient descent optimization process is the same as in the previous case, but in this case, where we have only two datasets to combine, the objective function is composed of only two data fidelity terms:

$$F(\mathbf{x}_A, \mathbf{x}_K) = \frac{1}{2}\|\mathbf{S}\,\mathbf{D}(\mathbf{x}_A, \mathbf{x}_K) - \mathbf{y}_{ccd}\|_2^2 + \frac{1}{2}\alpha\|\mathbf{R}_L\,\mathbf{M}(\mathbf{x}_A, \mathbf{x}_K) - \mathbf{y}_{spc}\|_2^2. \tag{3.16}$$

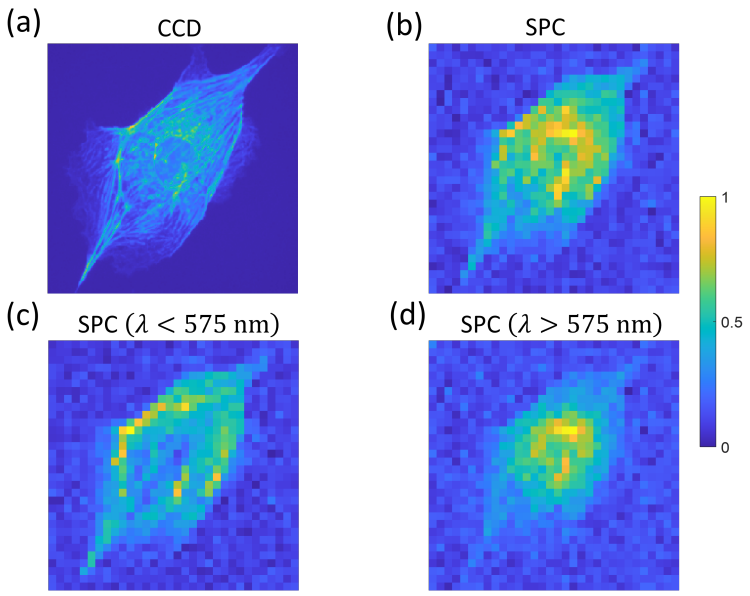

Figure 3.14: Representation of the BPAE cell dataset used for FLIM. (a) CCD camera image. (b) Projection over the spatial dimension of the SPC dataset by integrating over the full temporal and spectral dimension. (c) Projection over the spatial dimension of the SPC dataset by integration over the whole temporal dimension and for $\lambda < 575\,\text{nm}$. (d) Projection over the spatial dimension of the SPC dataset by integration over the entire temporal dimension and for $\lambda > 575\,\text{nm}$. All images are normalized in the range $[0, 1]$.

The fidelity of the reconstructed data with respect to the measured datasets is shown in Fig. 3.15. The spatially projected hypercubes by the operation $\mathbf{D}(\mathbf{x}_A, \mathbf{x}_K)$ and integrated for the lower half ($\lambda < 575\,\text{nm}$) and the upper half of the spectrum ($\lambda < 575\,\text{nm}$), are shown in Figs. 3.15(a) and 3.15(b), respectively. These high-resolution images match the qualitative spectral behavior of the SPC dataset (Figs. 3.14(a)-(b)). Figure 3.15(c) shows the temporal traces of a region of the cytoskeleton, mitochondria, and the background (as deduced from the spectral images), both from the temporal SPC dataset and from the time-resolved reconstruction obtained by $\mathbf{S}\,\mathbf{M}(\mathbf{x}_A, \mathbf{x}_K)$. And in Fig. 3.15(d) we have the spectral signatures of the same areas, both from the measured spectral SPC and from the time-integrated reconstruction obtained by $\mathbf{D}(\mathbf{x}_A, \mathbf{x}_K)$. While the spectral part shows a good agreement, the two temporal traces, one from the cytoskeleton and the one from the areas with mitochondria, show an almost identical decay due to the noisy measurements.

The reconstructed lifetime image for every spectral channel is presented in Fig. 3.16. There is no clear difference in lifetime between the areas where mitochondria are expected to be (lifetime images for $\lambda = 557\,\text{and}\,566\,\text{nm}$) and the areas where the cytoskeleton is expected to be (lifetime images for $\lambda \in 593 - 621\,\text{nm}$). While these two cell parts can be distinguished by the different spectral emission of their stains, lifetime analysis doesn't allow differentiation. This is due to the noise in the temporal dimension, but also to the spatial overlap of different fluorophores in cellular samples (for example, the actin filaments of the cytoskeleton can be found throughout the cell, including the areas where we have a mitochondrion), which

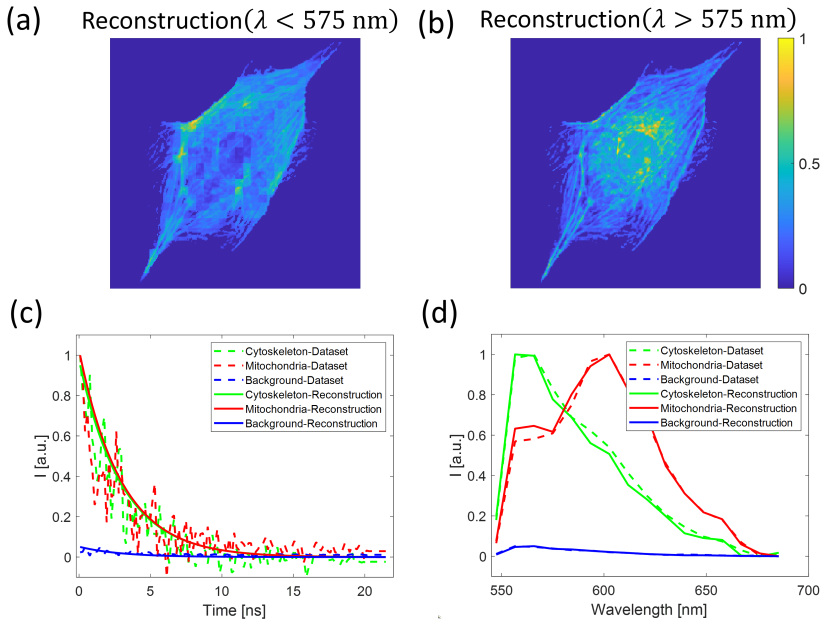

Figure 3.15: Spatial projections of the reconstructed hypercubes by integrating over time (operation $\mathbf{D}(\mathbf{x}_A, \mathbf{x}_K)$) for $\lambda < 575\,\text{nm}$ (a) and for $\lambda > 575\,\text{nm}$ (b) to highlight the different spectral emission of the different areas of the BPAE cell. The emission for $\lambda < 575\,\text{nm}$ corresponds to the Alexa Fluor 488-stained actin filaments of the cytoskeleton, and the emission for $\lambda > 575\,\text{nm}$ corresponds mainly to MitoTracker Red CMXRos-stained mitochondria. (c) Comparison of the temporal traces for the different parts of the cell from the SPC dataset and from the reconstructed hypercubes. (d) Comparison of the spectral signatures for the different parts of the cell from the SPC dataset and from the reconstructed hypercubes.

complicates the task of finding the correct lifetime values. To mitigate the former, we need to ensure that the measured SPC data set has the best achievable SNR or perform a denoising on the temporal dimension of the SPC dataset before feeding it to the DF algorithm. Also, as a future approach to this problem, we propose to reformulate the objective functions as:

$$F(\mathbf{x}_A, \mathbf{x}_K) = \frac{1}{2}\|\mathbf{S}\,\mathbf{D}(\mathbf{x}_A, \mathbf{x}_K) - \mathbf{y}_{ccd}\|_2^2 + \frac{1}{2}\alpha\|\mathbf{R}_L\,\mathbf{M}(\mathbf{x}_A, \mathbf{x}_K) - \mathbf{y}_{spc}\|_2^2 + \beta\mathcal{P}(\mathbf{x}_A, \mathbf{x}_K), \tag{3.17}$$

to hold an additional generic data prior term. This prior term is included because the problem is now much less well conditioned due to the noisy temporal trace and the spatial overlap of different fluorophores. The prior term can act on $\mathbf{x}_A$, $\mathbf{x}_K$, both, or even be a combination of several terms. Here is a list of some possible options for the prior term:

- l_1 norm of the amplitudes ($\mathbf{x}_A$) over the different lifetime channels enforcing a solution where the signal of each pixel is described with the least amount of different fluorophores.
- TV norm over the spatial dimension of $\mathbf{x}_A$, $\mathbf{x}_K$, or both, enforcing neighbouring pixels to have similar amplitudes or lifetime values.
- l_1, l_2 or TV norm of the whole datasets ($\mathbf{x}_A$, $\mathbf{x}_K$, or $\mathbf{M}(\mathbf{x}_A, \mathbf{x}_K)$), which are known priors for regularizing inversion problems.

This experiment is expected to produce convincing results by ensuring the best SNR in the measured SPC dataset, which of course implies longer integration times with the TCSPC system and therefore generally longer acquisition times; and by finding the appropriate prior (or priors) to disentangle the correct lifetime values.

3.6 General remarks for the chapter

While the DF of different detectors for multispectral time-resolved fluorescence imaging has been proven to work (at least in most of the experiments described), there is still room for improvement. For example, and following the motto of *Four eyes see more than two*[6], when the data sets to be merged share more than one dimension, with different resolutions, the fusion process would be less prone to errors in the measurements. Let's take the example of the macroscopic imaging system. Here there are three data sets, and the only dimension they share is space. Thus, the temporal or spectral information is only provided by the respective SPC. A better fusion would be achieved by replacing the high-resolution monochrome camera with a time-gated camera (with only a few time-gates) or an RGB color camera that shares more dimensions with the SPC than just the space. In addition, while the DF framework presented here is used to perform multispectral and time-resolved imaging, it can be applied to imaging any other dimension, such as polarization, phase, depth, or any other parameter.

[6]This is the literal translation of a proverb used in German (*Vier Augen sehen mehr als zwei*) or Spanish (*Más ven cuatro ojos que dos*) whose semantic translation in English is *Two heads are better than one*. Given the context of this thesis, the literal translation seemed more appropriate.

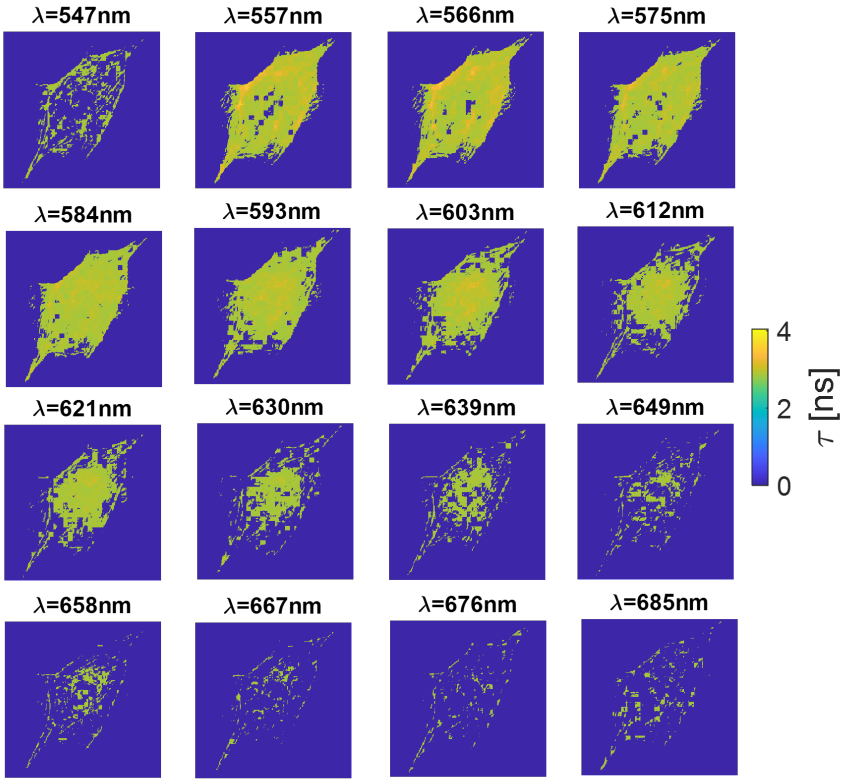

Figure 3.16: Lifetime images for every spectral channel for the BPAE cell dataset.

Chapter 4

Imaging of scattering and absorption

In this chapter, we will give some insights into the theory of light propagation in turbid media, presenting different models such as the radiative transport theory, the diffusion theory, the Monte-Carlo model or even the Kubelka-Munk (KM) model. We will also address the problem of imaging in turbid media, specifically the imaging or spatial characterization of the absorption and scattering properties of turbid media (called diffuse optical imaging or DOI), with special emphasis on the spatial frequency domain imaging (SFDI) technique. The contributions presented in this chapter include two DOI systems based on the concept of the SPC with an integrating sphere as a bucket detector. The first one uses reflectance and transmittance measurements and the KM model. And the other one uses only reflectance measurements while the theoretical framework is provided by SFDI.

4.1 Light propagation in turbid media

Many materials and most biological tissues are characterized by strong optical scattering. They are therefore referred to as scattering or turbid media. In this kind of media, the propagation of light is dominated by multiple scattering so that most photons undergo several scattering events before being re-emitted. In this chapter, we assume that light-matter interaction can be modeled by elastic scattering and absorption. In this case, scattering may change the direction of photon propagation, but it does not shift its wavelength. On the other hand, we will also consider that scatterers are sparsely distributed, i.e., the average distance between scattering centers is much greater than the size of the scatterer and the wavelength of the photons. This implies that successive scattering events are independent, and thus a single-scattering theory applies to each event[1] [145, 146, 189].

Light-matter interaction due to absorption is described with the absorption coefficient μ_a, which is defined as the probability of photon absorption in a medium

[1] Otherwise, in a densely packed medium, scattering events are coupled and a multiple scattering theory applies.

per unit path length[2]. The reciprocal of μ_a is referred to as the mean absorption length, which represents the average distance a photon propagates in the medium before being absorbed.

Interaction due to scattering is modeled by the scattering coefficient μ_s, and by the scattering phase function $p(\hat{\mathbf{s}}, \hat{\mathbf{s}}_0)$. The scattering coefficient is defined as the probability of photon scattering per unit path length. Its reciprocal represents the distance a photons travels before getting scattered and is referred to as the scattering mean free path (scattering MFP).

The phase function describes the probability of light incident on the scattering center from direction $\hat{\mathbf{s}}_0$ to be scattered in direction $\hat{\mathbf{s}}$. Being a probability function, it is normalized so that the probability of suffering a scattering at any angle is unity:

$$\int p(\hat{\mathbf{s}}, \hat{\mathbf{s}}_0)\, d\Omega = 1. \tag{4.1}$$

For large collections of scattering centers, approximations for the phase function are usually used. For example, an approximation can be given by Rayleigh's theory, but the most common phase function used in biomedical optics is Henyey-Greenstein's phase function [145, 146, 190]:

$$p(\hat{\mathbf{s}}, \hat{\mathbf{s}}_0) = p(\hat{\mathbf{s}} \cdot \hat{\mathbf{s}}_0) = \frac{1}{4\pi} \frac{1 - g^2}{(1 + g^2 - 2g\hat{\mathbf{s}} \cdot \hat{\mathbf{s}}_0)^{3/2}}, \tag{4.2}$$

which is a function of two variables: the angle θ subtended by the vectors $\hat{\mathbf{s}}$ and $\hat{\mathbf{s}}_0$ (because $\hat{\mathbf{s}} \cdot \hat{\mathbf{s}}_0 = \cos(\theta)$), and the anisotropy factor of the phase function, g, defined as $g = \langle \hat{\mathbf{s}} \cdot \hat{\mathbf{s}}_0 \rangle = \langle \cos(\theta) \rangle = 2\pi \int_0^\pi \cos(\theta) p(\theta) \sin(\theta) d\theta$. The anisotropy factor has a value between -1 and 1, and tells us how much scattering occurs in the forward direction compared to the backward direction. A value of zero indicates isotropic scattering, a value close to 1 represents dominantly forward scattering, and a negative value indicates that more light is back-scattered (see Fig. 4.1). Typical values for g in biological tissues is in the range $g \simeq 0.8 - 0.9$ [145–147].

The extinction coefficient is defined as

$$\mu_t = \mu_a + \mu_s, \tag{4.3}$$

and its reciprocal defines the MFP, l_{tr}, between two interaction events. The albedo a is defined as

$$a = \frac{\mu_s}{\mu_t}. \tag{4.4}$$

The variation in intensity of a light beam propagating in the direction of the z-axis is given by

$$\frac{dI(z)}{I(z)} = -\mu_t dz. \tag{4.5}$$

Assuming that μ_t is constant over z (valid for homogeneous media), and by integrating Eq. 4.5 we obtain Beer-Lambert's law:

$$I(z) = I_0 \exp(-\mu_t z), \tag{4.6}$$

[2]The absorption coefficient, as well as the scattering coefficient, are usually expressed in units of reciprocal centimeters cm^{-1}

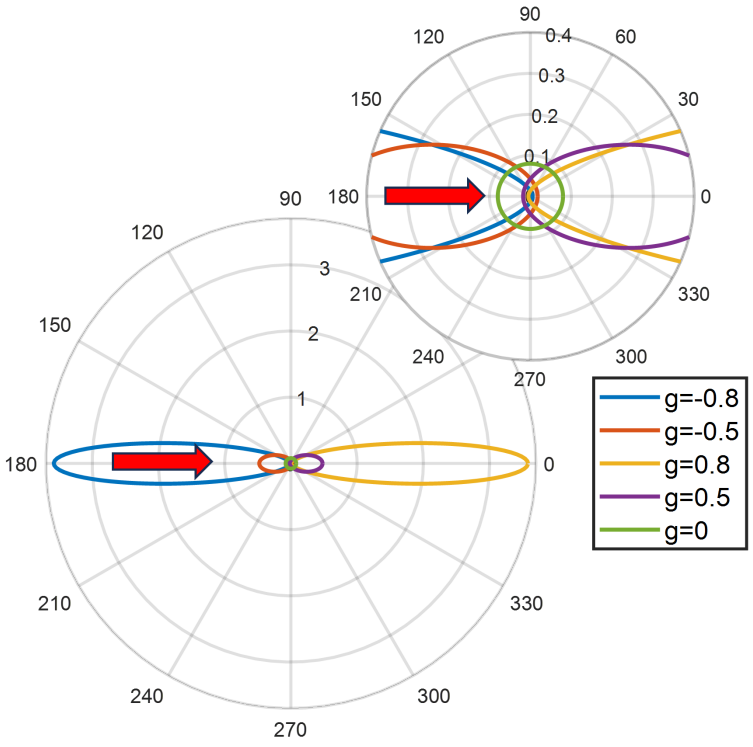

Figure 4.1: Polar plot of the Henyey-Greenstein phase function for anisotropy values of $g = -0.8, -0.5, 0, 0.5$, and 0.8. The inset on the right upper corner shows in greater detail the differences for the different anisotropy values. The red arrow indicates the light's direction of incidence.

where I_0 is the intensity of incident light. This expression predicts the attenuation of ballistic light, i.e., photons that travel in a straight line (see Fig. 4.2), due to propagation in the turbid media. Accordingly, the ballistic regime is defined to cover a depth given by $z \leq l_{tr}$. The number of unscattered photons decays exponentially, and after one MFP, the probability of no scattering is about 37%. Accordingly we define a quasi-ballistic regime, where photons have sustained a few scattering events but retain a strong memory of the original direction. Those kind of photons are also called *snake* photons due to their snake-like trajectory [191]. Intensity of snake photons also decays exponentially according to the following expression:

$$I(z) = I_0 \exp\left(-\mu_t' z\right), \tag{4.7}$$

but where we replaced μ_t by the reduced extinction coefficient, μ_t' defined as

$$\begin{aligned} \mu_t' &= \mu_a + \mu_s', \\ \mu_s' &= \mu_s(1-g), \end{aligned} \tag{4.8}$$

where μ_s' is referred to as the reduced scattering coefficient, which takes into account the average angular distribution of radiance through the inclusion of the anisotropy factor. The reciprocal of μ_t' is referred to as the transport mean free path (TMFP), l_{tr}', and as for most turbid media $g > 0$ the TMFP is larger than the MFP. This means that *snake* photons penetrate deeper into the media than ballistic photons. Consequently, the quasi-ballistic regime is defined to cover the range $l_{tr} < z \leq l_{tr}'$. After a few TMFPs, practically all photons have undergone many scattering events and thus have almost completely lost their memory of original direction. This is known as the diffusive regime [146, 147, 191]. The reduced scattering coefficient allows us to define the transport albedo

$$a' = \frac{\mu_s'}{\mu_t'}. \tag{4.9}$$

For biological tissues, representative values for the absorption and scattering coefficients, and the anisotropy factor are $\mu_a \simeq 0.1\text{cm}^{-1}$, $\mu_s \simeq 100\text{cm}^{-1}$, and $g \simeq 0.9$. Thus extending the ballistic regimen to approximately 0.01cm, and the quasi-ballistic regime to approximately 0.1cm [146].

4.1.1 The Kubelka-Munk model and method

Before proceeding to more advanced models, such as the one provided by the radiate transport equation (RTE) or the diffusion theory, I would like to mention that there are simpler models available, such as the adding-doubling method [145, 192], the δ-Eddington approximation [145, 193], or the Kubelka-Munk (KM) model [145, 194–196]. These models predict fluence rates as well as the amount of light reflected or transmitted by turbid media, and are used to estimate absorption and scattering properties of the media. Although the first two are methods for solving or approximating the RTE, the latter is a separate model with its own parameters. The KM model is a one-dimensional model that is still widely used because of its relative simplicity, as it allows to express the scattering and absorption coefficients directly in terms of the measured reflection and transmission, and

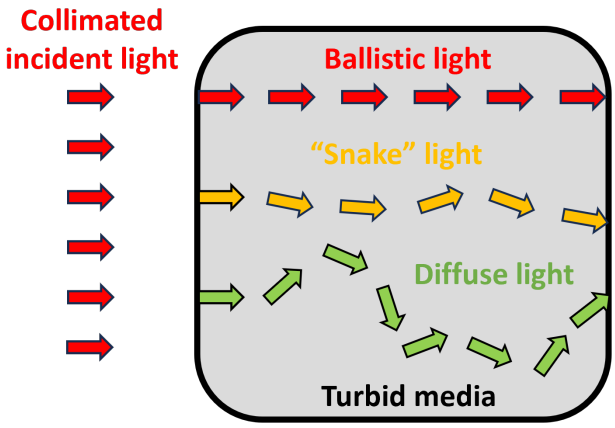

Figure 4.2: Schematic of the different components of light propagating in turbid media.

its acceptable prediction accuracy. It assumes that light propagation in turbid media can be modeled by two fluxes, which counter-propagate in the turbid media (see Fig. 4.3). The first flux i travels in the direction of the incident light and is decreased by absorption and scattering, while it is increased by back-scattering of the counter-propagating flux j. An analogous balance is made for the second or counter-propagating flux (j). The spatial evolution of those fluxes is described by the following system of differential equations:

$$\begin{aligned} -di &= -(S+K)idz + Sjdz, \\ dj &= -(S+K)jdz + Sidz, \end{aligned} \tag{4.10}$$

where S and K are the KM scattering and absorption coefficients, respectively, and where the direction of propagation is assumed to be in the z-axis. The KM model is based on several assumptions: the turbid medium is isotropic and homogeneous (S and K are constant throughout the medium), light loss at the edges is neglected as infinite lateral extension is assumed, there is no reflection at the boundaries, and illumination incident on the surface is completely diffuse [195, 197, 198].

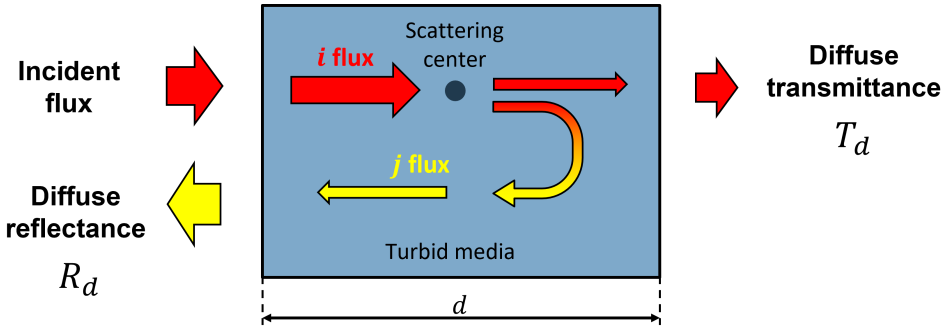

Figure 4.3: Schematic of the two-flux Kubelka-Munk model. The i flux travels in the direction of incident light and contributes to the transmittance, while the j flux travels in the opposite direction, is enhanced by scattering of the i flux, and contributes to the reflectance.

Integrating the KM equations for a finite turbid media slab of thickness d yields

the following expressions for the diffuse reflectance and transmittance:

$$\begin{aligned} R_d =& \frac{\sinh(bSd)}{a\sinh(bSd) + b\cosh(bSd)}, \\ T_d =& \frac{b}{a\sinh(bSd) + b\cosh(bSd)}, \end{aligned} \tag{4.11}$$

where we defined the secondary constants a and b as

$$\begin{aligned} a =& \frac{S+K}{S} = \frac{1 + R_d^2 - T_d^2}{2R_d}, \\ b =& \sqrt{a^2 - 1}. \end{aligned} \tag{4.12}$$

The measurement of R_d and T_d yields the KM parameters, S and K, via the inversion of Eqs. (4.11):

$$\begin{aligned} S =& \frac{1}{bd} \ln\left[\frac{R_d(b-a)+1}{T_d}\right], \\ K =& S(a-1). \end{aligned} \tag{4.13}$$

When scattering prevails on absorption, S and K can be related to the light transport theory coefficients (μ_a and μ_s') with the following general relations [199–201]:

$$\begin{aligned} S =& \eta\mu_s' - \vartheta\mu_a, \\ K =& \xi\mu_a. \end{aligned} \tag{4.14}$$

For an isotropic medium the values $\xi \in [1, 2]$, $\vartheta = 0$,and $\eta \in [0.3, 3/4]$ have shown to be valid [199, 202]. For an anisotropic medium good results have been obtained with the values $\xi = 2$, $\vartheta = 1/4$,and $\eta = 3/4$ [145, 199, 203, 204].

Nevertheless, in many experimental cases the condition of diffuse incident beam is not met. To extend the relations to include collimated incident light, and to extend the validity to the non-diffusive regime ($\mu_s' \gtrsim \mu_a$), the following empirical non-linear relations can be used [199]:

$$\begin{aligned} S =& 0.408\mu_s', \\ K =& \mu_a + 0.882(\mu_a\mu_s')^{0.72}. \end{aligned} \tag{4.15}$$

where S, K, μ_a, and μ_s' are expressed in units of cm^{-1}. The relations in Eqs. (4.15) can be inverted to obtain the coefficients μ_s' and μ_a from the KM parameters.

Additionally, by measuring the collimated transmittance (T_c) and applying Beer's law (Eq. (4.6)), the extinction coefficient can be obtained via

$$\mu_t = \frac{1}{d} \ln\left[\frac{(1-R_F)^2}{T_c}\right], \tag{4.16}$$

where $R_F = [(n-1)/(n+1)]^2$ is the Fresnel coefficient of reflection for normal incidence, and n is the relative refraction index of the sample and surrounding media. The additional determination of μ_t allows μ_s and g to be calculated in a

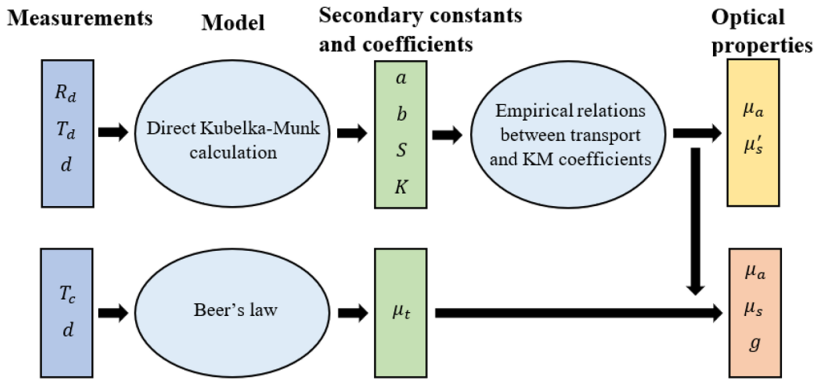

Figure 4.4: Flowchart of the process of calculating the optical properties of turbid media with the Kubelka-Munk (KM) model. Measurements of diffuse reflectance and transmittance lead to KM coefficients, which are then converted to transport coefficients. Additional measurement of the collimated transmittance permits separate estimation of all three transport coefficients (μ_a, μ_s', and g).

straightforward manner with Eqs. (4.3) and (4.8). Thus, all three radiative transfer parameters (μ_s, μ_s', and g) can be determined from experimental measurements of diffuse transmittance (T_d), diffuse reflectance (R_d), and collimated transmittance (T_c). The steps of this measurement process are represented in Fig. 4.4.

Experimental implementation of the KM method for measuring the optical properties of turbid media is performed using a collimated transmission method for measuring ballistic transmittance (Fig. 4.5(a)), and an integrating sphere technique for measuring diffuse reflectance and transmittance [145]. By using a double-integrating sphere configuration where the sample is "sandwiched" between two integrating spheres (see Fig. 4.5(b)), both reflectance and transmission can be measured simultaneously [145, 205]. In Fig. 4.5(b), the exit port of the second integrating sphere is intentionally left open, otherwise this integrating sphere would measure total transmittance ($T_t = T_c + T_d$) instead of diffuse transmittance. Also, in the case of a double-integrating sphere arrangement, corrections for multiple light exchange between the spheres should be considered [145, 206]. For the arrangement in Fig. 4.5(b), the following two coupled equations relate the measured transmittance (T_{IS}) and reflectance (R_{IS}) through the integrating spheres to the real reflectance (R_d) and transmittance (T_d):

$$\begin{aligned} R_{IS} &= \frac{[1 - m(\alpha + s/A)]\,[R_d A^2(1 - \alpha m - R_d s/A) + AsT_d^2]}{m\,[A^2(1 - \alpha m - R_d s/A)^2 - s^2 T_d^2]}, \\ T_{IS} &= \frac{[1 - m(\alpha + s/A)]\,[T_d A^2(1 - \alpha m - R_d s/A) + AsT_d R_d]}{m\,[A^2(1 - \alpha m - R_d s/A)^2 - s^2 T_d^2]}, . \end{aligned} \tag{4.17}$$

where m is the reflection factor of the sphere wall, s is the area of the sample, A is the total sphere area, and $\alpha = 1 - (\delta + s + h)/A$ is the area of the sphere wall relative to the total sphere area, e.g., excluding the area of the sample, the area of the entry or exit holes (h) and the area of the detector (δ).

Despite the use of a simple and less accurate model, the KM method is still widely used to measure the optical properties of turbid media. While some of the initial assumptions of the model, such as an isotropic medium and a diffuse incident beam,

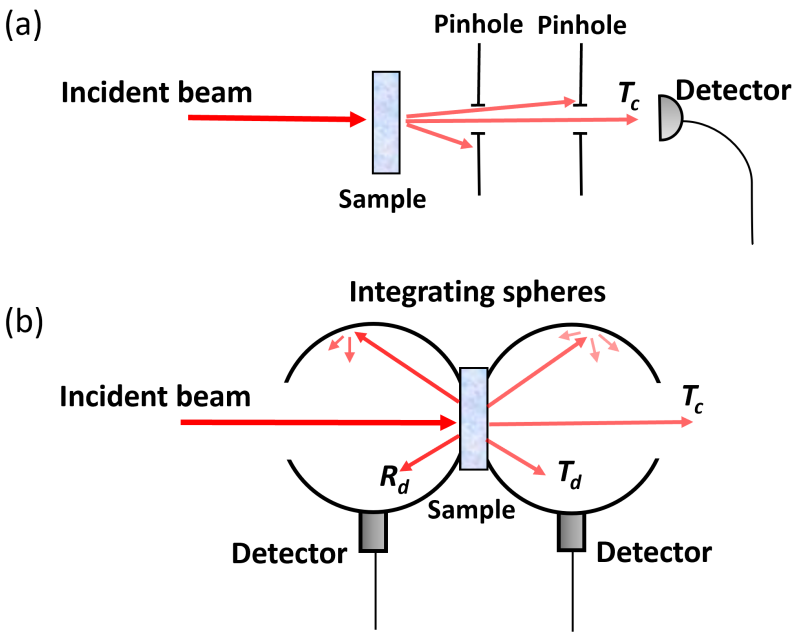

Figure 4.5: Experimental configurations for measuring (a) ballistic transmittance with a collimated transmission method and (b) diffuse reflectance and transmittance with two integrating spheres.

can be overcome with the correct choice of relations between the KM and transport theory coefficients, the method is still limited to the remaining assumptions and also to relatively thin samples due to the requirement of transmittance measurement. Often this model is used as a first guess in an inverse algorithm to estimate the optical properties based on a more accurate model.

4.1.2 Radiative transport equation

A more accurate modeling of photon transport in turbid media can be achieved with the Radiative Transport Equation (RTE). This model does not treat light as a wave, and therefore does not account for properties such as coherence, polarization, and nonlinearity [146, 147, 207, 208]. Applying the conservation of radiance to a differential volume element around position $\vec{r}$ over a differential solid angle element $d\Omega$ around direction $\hat{s}$ at time t yields the following equation:

$$\begin{aligned}\frac{1}{v}\frac{\partial L(\vec{r},\hat{s},t)}{\partial t} = &-\hat{s}\cdot\nabla L(\vec{r},\hat{s},t) - \mu_t L(\vec{r},\hat{s},t) + \\ &\mu_s \int_{4\pi} L(\vec{r},\hat{s}',t)p(\hat{s}'\cdot\hat{s})\,d\Omega' + S(\vec{r},\hat{s},t),\end{aligned} \tag{4.18}$$

which is known as the RTE (also called Boltzmann transport equation), and where $L(\vec{r},\hat{s},t)$ is the radiance (power per unit area per unit solid angle) at position $\vec{r}$ in the direction $\hat{s}$ at time t, v is the speed of light in the medium, $p(\hat{s}'\cdot\hat{s})$ is the phase function, $d\Omega'$ is the differential solid angle element around $\hat{s}'$, and $S(\vec{r},\hat{s},t)$ is the radiant source function.

The term on the left-hand side of Eq. (4.18) is the time derivative of the radiance (the net number of photons entering or leaving the differential volume element)

which equals the sum of different contributions: radiance diverging out of the volume element (first term on the right-hand side of Eq. (4.18)), the extinction (photon or energy loss due to scattering and absorption) within the volume element (second term on the right-hand side), the energy scattered from the differential solid angle element $d\Omega'$ into the solid angle element $d\Omega$ (third term on the right-hand side), and the energy radiated by a source into the volume element (last term).

4.1.3 Diffusion theory

The RTE is difficult to solve due to its integro-differential structure and its dependence on space, angle, and time (thus having six independent variables). As a result, analytical solutions are only available for simple scenarios, and numerical solutions are computationally intensive [146, 207–209].

Usually, approximations to the RTE are made, like in the δ-Eddington method or the diffusion theory. The diffusion approximation assumes that the radiance is nearly isotropic in a high-albedo scattering medium, i.e., in a medium where the scattering probability is much larger than the absorption probability ($\mu_s' \gg \mu_a$). To obtain the diffusion equation, the basic idea is to perform a first-order expansion of the radiance on the basis of spherical harmonics:

$$L(\vec{r}, \hat{s}, t) \approx \frac{1}{4\pi}\Phi(r,\vec{t}) + \frac{3}{4\pi}\vec{J}(\vec{r}, t) \cdot \hat{s}, \tag{4.19}$$

where $\Phi(r,\vec{t})$ is the fluence rate, defined as the energy flux per unit area per unit time regardless of the flux direction, expressed as the integral of the radiance over the entire solid angle; and $\vec{J}(\vec{r}, t)$ is the current density or energy flux, defined as the net energy flux per unit area per unit time, expressed as the integral of the directed radiance over the entire solid angle. The first term on the right side of Eq. (4.19) represents the isotropic component of the radiance, while the second term represents the anisotropic or directional component of the radiance.

By assuming a isotropic source function, i.e., independent of the direction $\hat{s}$ ($S(\vec{r}, \hat{s}, t) = S(\vec{r}, t)/4\pi$), substituting Eq. (4.19) into the RTE, and integrating over the entire solid angle we obtain the following scalar differential equation:

$$\frac{1}{v}\frac{\partial\Phi(\vec{r}, t)}{\partial t} + \mu_a\Phi(\vec{r}, t) + \nabla \cdot \vec{J}(\vec{r}, t) = S(\vec{r}, t). \tag{4.20}$$

With the same procedure, but multiplying both sides of the RTE by $\hat{s}$ before integrating, we obtain the following vector differential equation:

$$\frac{1}{v}\frac{\partial\vec{J}(\vec{r}, t)}{\partial t} + (\mu_a + \mu_s')\vec{J}(\vec{r}, t) + \frac{1}{3}\nabla\Phi(\vec{r}, t) = 0. \tag{4.21}$$

Equations (4.20) and (4.21) do not contain $\hat{s}$, but do have two physical variables: $\Phi(\vec{r}, t)$ and $\vec{J}(\vec{r}, t)$. To obtain a single differential equation containing $\Phi(\vec{r}, t)$ only we have to assume that

$$\frac{1}{v}\left|\frac{\partial\vec{J}(\vec{r}, t)}{\partial t}\right| \ll (\mu_a + \mu_s')\left|\vec{J}(\vec{r}, t)\right|, \tag{4.22}$$

and therefore the time-dependent term in Eq. (4.21) vanishes, leading to Fick's law:

$$\vec{J}(\vec{r},t) = -D\nabla\Phi(\vec{r},t), \tag{4.23}$$

where the diffusion coefficient D is defined as

$$D = \frac{1}{3(\mu_a + \mu_s')}. \tag{4.24}$$

In general, Fick's law states that the diffusive flux is inversely proportional to the concentration gradient and describes not only the diffusion of photons in turbid media, but also diffusion in other forms, such as particles suspended in liquids or gases, or heat in a metal [146].

Finally, by substituting Eq. (4.23) into Eq. (4.20), we obtain the diffusion equation:

$$\frac{1}{v}\frac{\partial\Phi(\vec{r},t)}{\partial t} + \mu_a\Phi(\vec{r},t) - \nabla\cdot[D\nabla\Phi(\vec{r},t)] = S(\vec{r},t). \tag{4.25}$$

Additionally, if D is space-invariant we obtain the following equation:

$$\frac{1}{v}\frac{\partial\Phi(\vec{r},t)}{\partial t} + \mu_a\Phi(\vec{r},t) - D\nabla^2\Phi(\vec{r},t) = S(\vec{r},t), \tag{4.26}$$

which is the diffusion equation for homogeneous media. The diffusion equation does not depend on the direction $\hat{s}$, and thus has only four instead of six degrees of freedom. It also does not depend on μ_s or g, but on their combination in the reduced scattering coefficient. This is known as the similarity relation.

Three approximations were made in the derivation of the diffusion equation (Eq. (4.26)):

- The gradient of the diffusion coefficient (D) is zero or close to zero, which is valid for homogeneous turbid media or media without drastic changes in optical properties.
- A first-order expansion of the radiance on the basis of spherical harmonics is made. This approximation is valid when the radiance is nearly angularly uniform and shows only a relatively small flux in a given direction, i.e., the radiance is nearly isotropic.
- The fractional change in the current density in one TMFP is much less than unity. This means that the photon current is temporally broadened because of multiple scattering events.

Both conditions, the isotropic radiance and the temporal broadening, can be condensed into a single condition: the reduced scattering coefficient has to be much larger than the absorption coefficient ($\mu_s' \gg \mu_a$), because for photons to be completely diffuse, they must undergo a sufficient number of scattering events before being absorbed. In addition, the observation point must be sufficiently distant from sources and boundaries.

In a stationary, that is, time-independent state, Eq. (4.26) becomes:

$$\nabla^2\Phi(\vec{r}) - \mu_{eff}^2\Phi(\vec{r}) = -3\mu_t' S(\vec{r}), \tag{4.27}$$

where

$$\mu_{eff} = \sqrt{\frac{\mu_a}{D}} = \sqrt{3\mu_a(\mu_a + \mu_s')} \tag{4.28}$$

is the effective attenuation coefficient. Equation (4.27) is referred to as the time-independent diffusion equation for homogeneous media.

Impulse responses and boundary conditions

Equation (4.27) is a inhomogeneous Helmholtz equation. It can be solved for any source function $S(\vec{r})$ using the method of Green's function. The Green function in an infinite turbid media, $\Phi_\infty(\vec{r};\vec{r}')$, is obtained by solving

$$\nabla^2\Phi_\infty(\vec{r};\vec{r}') - \mu_{eff}^2\Phi_\infty(\vec{r};\vec{r}') = -3\mu_t' S_0\delta(\vec{r}-\vec{r}'), \tag{4.29}$$

which corresponds to the Eq. (4.27) with a point source located at $\vec{r}'$ ($S(\vec{r}) = S_0\delta(\vec{r}-\vec{r}')$). Therefore the Green functions is also referred to as the impulse response. The solution to Eq. (4.29) is

$$\Phi_\infty(\vec{r};\vec{r}') = \frac{S_0}{4\pi D\|\vec{r}-\vec{r}'\|}\exp\left(-\mu_{eff}\|\vec{r}-\vec{r}'\|\right). \tag{4.30}$$

With the appropriate boundary condition (fluence rate vanishing at infinity), the general solution to the time-independent diffusion equation (Eq. (4.27)) is

$$\Phi(\vec{r}) = \int_{V'}\Phi_\infty(\vec{r};\vec{r}')S(\vec{r}')\,d\vec{r}', \tag{4.31}$$

which represents a convolution because the Green function is translation-invariant.

In the case of non-infinite turbid media, boundary conditions must be introduced to account for the interface between the turbid medium and the ambient medium. In a refractive index mismatched boundary, the radiance propagating from the ambient medium into the scattering medium comes from radiance inside the turbid medium that is reflected at the interface. This imposes the following boundary condition for the fluence rate [146]:

$$\Phi(\vec{r}) - 2C_R D\nabla\Phi(\vec{r})\cdot\hat{n} = \Phi(\vec{r}) - 2C_R D\frac{\partial\Phi(\vec{r},t)}{\partial z} = 0, \tag{4.32}$$

where C_R is defined as

$$C_R = \frac{1+R_{\text{eff}}}{1-R_{\text{eff}}}, \tag{4.33}$$

with R_{eff} being an effective reflection coefficient that represents the fraction of outgoing radiance integrated over the solid angle that is reflected at the interface and converted to incoming radiance integrated over the solid angle. Commonly the following empirical formula is used [146, 210]:

$$R_{\text{eff}} \simeq 0.0636\,n + 0.668 + \frac{0.710}{n} - \frac{1.440}{n^2}. \tag{4.34}$$

By using the Maclaurin series expansion to the first order of the fluence rate in the z dimension, we obtain

$$\Phi(\vec{r}) = \Phi(\vec{\rho},z) \simeq \Phi(\vec{\rho},z=0) - \left.\frac{\partial\Phi(\vec{r})}{\partial z}\right|_{z=0} z, \tag{4.35}$$

where $\vec{\rho} = x\hat{x} + y\hat{y} = \rho\hat{\rho}$ are the coordinates in the xy-plane[3]. We can see that the boundary condition (Eq. (4.32)) is fulfilled, and therefore the fluence rate is approximately zero, on an extrapolated boundary at a distance $z = -z_b$ given by:

$$z_b = 2C_R D. \tag{4.36}$$

Equation (4.30) describes the response of an infinite turbid medium to an isotropic point source. To model the response of an infinitely narrow beam, normally incident on a semi-infinite medium, with diffusion theory, the boundary conditions must be taken into account along with some approximations. First, the anisotropic medium ($g \neq 0$) is converted into an isotropic medium ($g = 0$) based on the similarity relation (keeping μ_s' constant). Second, the infinitely narrow beam is converted into an isotropic point source located one TMFP inside the scattering medium, with its power reduced by a factor given by the transport albedo a'. Lastly, the interface with the ambient medium is removed, and an image source is added at a distance $z = -(l_{tr}' + 2z_b)$ to satisfy the boundary condition.

The image point source is symmetrical to the original under reflection at the extrapolated boundary, but with opposite polarity (i.e. opposite sign). By adding this image source, the single point source in a semi-infinite medium is converted into two point sources in an infinite medium. The impulse response in a semi-infinite medium is therefore approximated by a superposition of the responses to the two sources in an infinite medium, that is,

$$\Phi_{\infty/2}(\vec{\rho}, z; \vec{\rho}', z') = a' \left[\Phi_\infty(\vec{\rho}, z; \vec{\rho}', z') - \Phi_\infty(\vec{\rho}, z; \vec{\rho}', -z' - 2z_b)\right], \tag{4.37}$$

where $z' = l_{tr}'$, but z' has been retained in order to generalize this result to an isotropic point source at an arbitrary distance z' that is not strictly the TMFP. The approach of replicating the boundary conditions by replacing the physical boundaries with image sources is similar to the method of image charges used in electrostatic problems.

Diffuse reflectance is calculated as the current density projected to the surface normal [189]:

$$R_d(\vec{\rho}) = -\left(\hat{n} \cdot \vec{J}(\vec{r})\right)\Big|_{z=0} = D\left.\frac{\partial \Phi(\vec{r})}{\partial z}\right|_{z=0}, \tag{4.38}$$

where Fick's law has been used to write this expression as a function of the fluence rate. Using Eq. (4.38) to compute the reflectance impulse response in a semi-infinite turbid medium yields:

$$R_{d,\infty/2}(\vec{\rho};\, \vec{\rho}', z') = a' \left[R_\infty(\vec{\rho};\, \vec{\rho}', z') - R_\infty(\vec{\rho};\, \vec{\rho}', -z' - 2z_b)\right], \tag{4.39}$$

where

$$R_\infty(\vec{\rho};\, \vec{\rho}', z') = \frac{S_0 z'(1 + \mu_{eff}\|\vec{\rho} - \vec{\rho}' - z'\hat{z}\|)\exp\left(-\mu_{eff}\|\vec{\rho} - \vec{\rho}' - z'\hat{z}\|\right)}{4\pi\|\vec{\rho} - \vec{\rho}' - z'\hat{z}\|^3}. \tag{4.40}$$

[3]Note that $\vec{r} = x\hat{x} + y\hat{y} + z\hat{z} = \vec{\rho} + z\hat{z} = \rho\hat{\rho} + z\hat{z}$, where $\hat{x}$, $\hat{y}$ and $\hat{z}$ are the unit vectors in Cartesian coordinates, and $\hat{\rho}$ is the radial unit vector along the axis of symmetry in cylindrical coordinates.

In a finite turbid medium such as a slab, an infinite number of image sources corresponding to the successive reflections at the extrapolated boundaries are required to completely describe the fluence rate. However, the series of image sources can be truncated after several pairs of sources, depending on the required accuracy [146].

4.1.4 Monte Carlo method

Photon transport in turbid media can also be modeled with a numerical simulation based on the Monte Carlo (MC) method [145, 146, 211]. The MC light transport model (hereafter MC model) consists of generating random photon trajectories based on probability distributions derived from Beer's law and the phase function. By tracking a large number of photon trajectories, the spatial distribution of various physical quantities (such as reflectance, transmittance, absorption, internal fluence rates, etc.) can be estimated. Here we describe the method for computing the reflectance impulse response for an infinitely narrow and normally incident beam on a semi-infinite medium. The response to a broadbeam source in a homogeneous medium can be obtained by convolution of the impulse response with the intensity profile of the beam [146].

The steps followed by the MC simulation are shown in the flowchart of Fig. 4.6. A photon packet of unit weight ($W = 1$) is launched perpendicularly onto the turbid medium. Because of Fresnel reflection only a fraction of the weight ($(1 - R_F)W$) is transmitted into the medium. Next, the photon packets propagates a distance s, which is statistically distributed around the MFP based on Beer's law, calculated as

$$s = -\frac{\ln \xi}{\mu_t}, \tag{4.41}$$

where ξ is a random variable uniformly distributed between 0 and 1. After moving the distance s, the photon packet loses a fraction $1-a$ of its weight due to absorption. If the weight of the photon packet falls below some predefined threshold then the Russian roulette is activated. This technique terminates low-weight photon packets early in order to save computation time. However, in order to conserve the total energy, the Russian roulette gives the photon packet one chance in m (where m is a parameter of the Russian Roulette and can be taken as $m = 10$) of surviving with an increased weight of mW. Mathematically this technique is expressed as

$$W \rightarrow \begin{cases} mW & \text{if} \quad \xi \leq \frac{1}{m} \\ \\ 0 & \text{if} \quad \xi > \frac{1}{m}, \end{cases} \tag{4.42}$$

where ξ is once again a random number between 0 and 1. Next, the photon packet is scattered in a new direction, which is determined statistically based on the Henyey-Greenstein phase function. These steps are repeated until the photon packet is terminated or re-emitted to the ambient medium, in which case its weight is stored in a radial grid representing the radially-resolved reflectance impulse response $R_{MC}[\rho_i]$[4]. And the whole process is repeated and averaged over a large number (N) of photon packets.

[4]The reflectance is written as a function of the radial coordinate only because of the angular rotation simetry. Also, the computed distribution is discrete and not continuous.

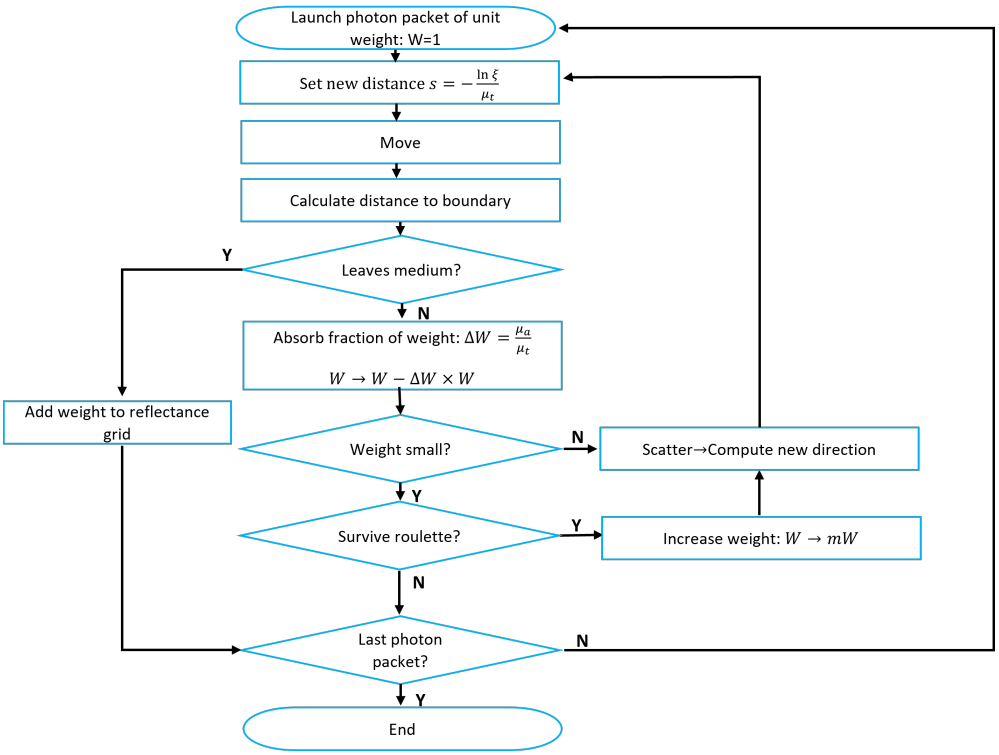

Figure 4.6: Flowchart of the Monte Carlo light propagation model for computing the diffuse reflectance of a semi-infinite medium. Y and N represent yes and no, respectively.

Unlike diffusion theory, the MC model is accurate even outside the diffuse regime and close to sources and boundaries. However, it is computationally inefficient due to the need to simulate large numbers of photon packets traveling large trajectories before being absorbed or reflected, whereas the impulse response of diffusion theory can be computed very efficiently. A combination of these two approaches, a hybrid model of Monte Carlo and diffusion theory, or hybrid Monte Carlo (HMC), would combine the best of both: the accuracy and flexibility of the MC method, yet be faster to compute than a pure MC simulation.

The HMC model has two steps, in the first one the conventional MC method is used to track the trajectory of photons until they are re-emitted to the ambient medium (in which case they would be part of $R_{MC}[\rho_i]$), absorbed, or until they reach a critical depth z_c. If a photon packet scatters beyond z_c, a new direction is computed. And if by moving a TMFP along this new direction the photon packet does not leave the critical depth, it is converted to an isotropic point source, otherwise its path is followed with the MC part.

Conversion of the photon packet to an isotropic point source is based on the similarity relation and the previously explained steps of approximation. The anisotropic turbid medium is converted to an isotropic medium while maintaining μ_s'. After moving one TMFP, the weight of the photon packet is reduced by a factor $1-a'$ due to absorption. Next the photon packet is converted into an isotropic point source, and its weight is recorded into a source function $S[\rho_i, z_j]$. This MC step is repeated for a large number (N) of photon packets. Consequently, the radially distributed diffuse reflectance R_{MC}, and the distribution of isotropic sources S are averaged

over the N photon packets.

Next, in the diffusion step, the contribution of S to the diffuse reflectance is computed with the diffusion theory:

$$R_{DT}[\rho_i] = \rho_i \Delta\rho \sum_{j,k} S[\rho'_j, z'_k]\, I[\rho_i; \rho'_j, z'_k], \tag{4.43}$$

where $\Delta\rho$ is the width of the radial grid element, and $I[\rho_i; \rho'_j, z'_k]$ is the discretization of the following integral:

$$I(\rho; \rho', z') = \int_0^{2\pi} R_{d,\infty/2}(\rho, \phi = 0;\, \rho', \phi', z')\, d\phi', \tag{4.44}$$

where we used the impulse response in a semi-infinite turbid medium (Eq. (4.37)) and cylindrical coordinates so that $\vec{\rho} = (\rho, \phi)$ with ϕ being the azimuthal angle. This integral over ϕ' can be evaluated with numerical methods. The derivation of Eq. (4.43) can be found in Appendix C.

The final diffuse reflectance R_d provided by the HMC model is the sum of the contributions of the MC step and the diffusion theory step:

$$R_d[\rho_i] = R_{MC}[\rho_i] + R_{DT}[\rho_i]. \tag{4.45}$$

4.2 Imaging in turbid media

The imaging of structures and objects through dense turbid media is a challenge for research in the technological field, but especially in the biomedical field. Some of the imaging modalities traditionally used in these fields are X-ray radiography and tomography, magnetic resonance imaging (MRI), ultrasound, and positron emission tomography (PET) [146, 212–214]. As an alternative, optical imaging techniques have been postulated, which are non-invasive, fast, economical and harmless since they do not use ionizing radiation. These characteristics make these techniques particularly interesting for *in vivo* imaging.

Optical imaging techniques in turbid media can be classified into three classes according to the light propagation regimes defined in section 4.1: ballistic, quasi-ballistic (or *snake*), or diffuse light imaging techniques [191]. A more or less similar classification based on the depth of operation has been made into microscopy, macroscopy, and mesoscopy [212]].

Ballistic imaging techniques provide the best resolution (generally only limited by the diffraction of the optical system) but can only be used for thin samples as the ballistic signal attenuates rapidly as it passes through the turbid medium. They are based on filtering or discriminating the scattered light. Examples of ballistic techniques are time-gated imaging [146, 191, 215], spatiofrequency-filtered imaging[5] [17,146,191,216], polarization-difference imaging[6] [146,191,217,218], holographic imaging techniques [191,219], confocal microscopy [191,212,220], two-photon microscopy [212, 221] and optical coherence tomography (OCT) [145, 146, 191, 212].

[5] Also called Fourier space-gated or Fourier filtering imaging.

[6] Also called polarization-gated imaging.

Imaging with *snake* light is an intermediate regime between ballistic and diffuse. Traditionally is has received the least attention. However, recent advances in techniques based on wavefront control with SLMs have made it possible to develop imaging methods in this regime, increasing the depth range down to the mesoscopic level while maintaining good resolution [19, 20]. These methods are based on the measurement of the transfer matrix of the turbid medium [222], on the use of iterative techniques [223] or on phase conjugation techniques [224]. Methods that use speckle scanning microscopy (SSM) exploiting the memory effect have also been proposed [18].

Finally, we have the imaging techniques that operate in the diffuse regime, and which are called diffuse optical imaging (DOI) techniques. When imaging in thick scattering media, all detected photons are diffuse, and images must be formed with highly scattered photons. In this modality, it is not an object embedded in the turbid medium that we want to image, but the inhomogeneities of the scattering medium itself are the structures we want to image [207, 208, 225, 226]. An object in this sense would be, for example, tumor tissue, which has different scattering and absorption properties than the surrounding healthy tissue due to its greater vascularization. It is also necessary to use a model of light transport in turbid media to set up an inversion method to extract information about scattering and absorption properties.

DOI has the already mentioned advantages of optical imaging techniques (non-invasive, non-ionizing and economical), in addition to others such as the possibility of examining samples of high thickness and high optical density, due to their great penetration power (up to several centimeters into biological tissue for light in the red and infrared parts of the spectrum) [146, 191, 207]. Disadvantages include the low spatial resolution of these techniques [146, 191], on the order of 20% of the penetration depth, and the need to use approximate models along with inversion methods, which limits accuracy.

The main applications of DOI are found in the biomedical field for optical mammography, detection of tumors, hemorrhage, embolism and stroke, imaging and monitoring of brain activity and visualization of muscle tissue [207, 226, 227]. In addition to the important applications in biomedicine, it also has applications in the chemical, food and agricultural industries [209, 228].

Typically, measuring the optical properties of a turbid medium relies on a technique that resolves either the spatial or temporal response of light propagation within the medium. Therefore, the measurements and instrumentation for DOI can be classified into two domains: the time-independent (also known as spatial domain) and the time-dependent (also known as time-resolved, or simply time domain). Similar to fluorescence imaging measurements (Section 3.2), both domains (spatial and temporal) can be divided into two subdomains: the real and the frequency domain. In the real domain, the response to a point in space or a pulse in time (the point-spread function (PSF) or impulse response) is measured. On the other hand, the frequency domain measures the amplitude modulation or phase shift (related to the modulation transfer function (MTF)) of a periodic illumination in space or time [208, 210, 229, 230]. Thus, measurements in one of these domains, in conjunction with an appropriate light propagation model, allow the scattering and absorption properties of the sample to be distinguished and quantified.

The real and frequency domains, whether temporal or spatial, are related via the Fourier transform: the measurement of the PSF in response to a infinitely narrow point or infinitely short pulsed source is equivalent to a frequency domain sweep of the MTF. However, measurements in each domain have their respective advantages and disadvantages in terms of accuracy, instrumentation cost, resolution, imaging speed, computational cost, etc.

In time-domain techniques, the sample is illuminated with light pulses (of the order of a few picoseconds) and the temporal PSF (t-PSF) is measured using time-gated or single photon counting detection. The rich information provided by temporal light propagation allows the best decoupling of optical absorption and scattering properties from the analysis of the attenuation and broadening of the t-PSF with respect to the source pulse. However, extracting information from the temporal measurements requires the use of more complex models and more expensive instrumentation [146, 207, 208, 229].

In the temporal frequency domain (this technique is also referred to as temporal frequency domain migration (FDPM)), an intensity-modulated source is used instead of a pulsed source [146, 191, 207, 208, 230]. The modulation frequency is on the order of a few hundred MHz. The propagation of light causes the response to be modulated at the same frequency, but amplitude-attenuated and time-delayed. With the proper model of photon transport, the measured relative phase and amplitude provide an accurate estimate of the optical properties. This method can be performed at single or multiple modulation frequencies. Sweeping over many frequencies yields the temporal MTF (t-MTF), which is the Fourier equivalent of the t-PSF.

The real spatial domain (often referred to as continuous wave (CW)) measures the intensity response to a time-invariant light source. The spatial PSF (s-PSF) is typically characterized by multi-distance measurements to track the spatial response to a point-like source. This can be done by scanning with a single point detector, by using multiple point detectors, or by using spatially resolved detectors. And the spatial resolution to obtain an image is usually achieved by using multiple point sources. Typically, CW instrumentation is fast and inexpensive, but provides limited absorption and scattering separability. [146, 208, 210, 229, 231, 232].

Lastly we have the spatial frequency-domain imaging (SFDI), which would be the spatial analog to FDPM, but with spatial instead of temporal modulation. The general procedure in this modality is to project spatially structured light patterns (e.g. sinusoidal fringes) at multiple spatial frequencies and phases onto the sample and to capture the diffuse reflected light distribution with a camera. These measurements of diffuse reflectance are processed to obtain information about the spatial MTF (s-MTF) in order to spatially map the optical properties of the sample [208, 210, 229, 233, 234].

Methods that operate in the real domain can provide high SNR, but are usually implemented with point source and point detector pairs or in point scanning geometries, which is a problem for capturing larger FOVs. It should be noted that wide-field imaging in the time domain can be achieved by using ultrafast cameras such as SPAD arrays or streak cameras, but this suffers from high complexity and cost. On the other hand, due to the nature of the instrumentation used, mea-

surements in the frequency domain can be easily multiplexed over multiple pixels, allowing for wide field imaging. In this sense, SFDI is particularly advantageous in terms of spatial multiplexing, imaging a large FOV, and the relative simplicity and cost of the instrumentation. However, because SFDI is a non-contact method and is typically used in a reflectance geometry, it provides limited depth sensitivity (limited to around a few mm) [208, 210, 229, 233, 234].

4.2.1 Spatial frequency domain imaging

In this section, we present the theory and experimental methods for performing SFDI. First, we will derive the analytical expression for the fluence rate and diffuse reflectance in response to a sinusoidally modulated source. We assume a semi-infinite medium and a normally incident plane wave source with periodic modulation along the x-axis:

$$S(\vec{r}) = S_0(z)\cos(2\pi f x + \alpha), \tag{4.46}$$

where f is the spatial frequency of the sinusoidal modulation, and α is an arbitrary spatial phase. $S_0(z)$ describes the depth dependence of the source.

Assuming a linear medium, the sinusoidally modulated source will yield a fluence rate modulated at the same frequency and phase

$$\Phi(\vec{r}) = \Phi_0(z)\cos(2\pi f x + \alpha). \tag{4.47}$$

Inserting Eqs. (4.46) and (4.47) into the time-independent diffusion equation for a homogeneous media (Eq. (4.27)) yields the following one-dimensional second-order Helmholtz equation for the z-dependent part of the fluence rate:

$$\frac{\mathrm{d}^2}{\mathrm{d}z^2}\Phi_0(z) - \mu'_{eff}\Phi_0(z) = -3\mu'_t S_0(z), \tag{4.48}$$

where

$$\mu'_{eff} = \sqrt{\mu_{eff}^2 + (2\pi f_x)^2} \equiv \frac{1}{\delta'_{eff}}. \tag{4.49}$$

The Eq. (4.48) can be understood as a time-independent wave equation with an effective attenuation coefficient μ'_{eff}, which depends on the optical properties of the medium, but also on the spatial frequency of the modulation. In other words, the periodically modulated plane wave source gives rise to a periodically modulated wave that propagates in the medium with an effective penetration depth δ'_{eff}. This penetration depth decreases for higher frequencies and increases for lower frequencies, with the maximum penetration depth at zero frequency ($f = 0$). This feature enables depth sensing and tomography [233, 234].

Next, we model an extended and isotropic source created by scattering of a collimated beam of power P_0 [210, 235]. Therefore, the z dependence of the source function is written as

$$S_0(z) = P_0\mu'_s\exp(-\mu'_t z), \tag{4.50}$$

with which the general solution to Eq. (4.48) can be expressed as a combination of the solution to the associated homogeneous differential equation, and a particular solution:

$$\Phi_0(z) = \Phi_{0,h}(z) + \Phi_{0,p}(z). \tag{4.51}$$

The particular solution is given by:

$$\Phi_{0,p}(z) = A \exp(-\mu_t' z), \tag{4.52}$$

where

$$A = \frac{3\mu_t'\mu_s' P_0}{\mu_{eff}'^2 - \mu_t'^2}. \tag{4.53}$$

The homogeneous solution is given by:

$$\Phi_{0,h}(z) = B \exp(\mu_{eff}' z) + C \exp(-\mu_{eff}' z), \tag{4.54}$$

where $B = 0$ because the fluence rate has to vanish in the limit $z \to \infty$, and where C is a constant determined by substituting the general solution $\Phi_0(z)$ into the boundary condition given by Eq. (4.32):

$$C = \frac{-3P_0\, a'(2C_R + 3)}{(\mu_{eff}^2/\mu_t'^2 - 1)(2C_R\mu_{eff}'/\mu_t' + 3)}. \tag{4.55}$$

The derived fluence rate $\Phi(\vec{r})$ yields, trough Eq. (4.38), the following diffuse reflectance:

$$R_d(\vec{\rho}; f) = MTF(f) \cos(2\pi f x + \alpha), \tag{4.56}$$

which follows the same periodic modulation but with an amplitude given by:

$$MTF(f) = \frac{3a'}{(\mu_{eff}'/\mu_t' + 1)(2C_R\mu_{eff}'/\mu_t' + 3)}, \tag{4.57}$$

which can be shown (Appendix D) to be the s-MTF evaluated at the spatial frequency f. The frequency dependence of $MTF(f)$ describes the low-pass spatial filtering properties of turbid media. Also, at low spatial frequencies ($\mu_{eff} >> 2\pi f$) the absorption has maximal effect on the MTF, and at high spatial frequencies ($\mu_{eff} << 2\pi f$) the MTF becomes more sensitive to changes of μ_s' [210]. It is important to note that since Eq. (4.57) is derived with diffusion theory, its validity is limited to spatial frequencies much lower than the reduced transport coefficient $f << \mu_t' = 1/l_{tr}'$ [210, 229, 233].

Measurements of the amplitude modulation of the diffuse reflected sinewave can be related to the s-MTF, and by solving an inversion problem, the optical coefficients, μ_a and μ_s' can be extracted. The simplest implementation requires the projection of sinusoidal patterns at different spatial frequencies (at least two) each with three different spatial phase offsets ($\alpha = 0, 2\pi/3$ and $4\pi/3$) onto the turbid medium. Typically, to best decouple absorption from scattering, two spatial frequencies are used, a low or zero frequency ($f_{DC} \approx 0$) and a relatively high frequency (f_{AC}). In practice, the projection is usually done with a SLM based on DMD technology, and the illumination must be a superposition of an AC (carrying the modulation) and a DC (planar or constant illumination) term, since we cannot illuminate with negative intensity. Therefore, by exploiting the fact that a zero spatial frequency component is always present when projecting intensity light patterns, single AC frequency patterns can be used. In the latter case, three reflectance images ($I[x_i, y_j; f_{AC}, \alpha = 0], I[x_i, y_j; f_{AC}, \alpha = 2\pi/3]$, and $I[x_i, y_j; f_{AC}, \alpha = 4\pi/3]$) are

captured by a camera. Each reflectance image is a superposition of the AC and DC components:

$$I[x_i, y_j; f_{AC}, \alpha] = I_{AC}[x_i, y_j; f_{AC}, \alpha] + I_{DC}[x_i, y_j]. \tag{4.58}$$

The AC component of the image can be modeled by a sinewave with an amplitude envelope $M_{AC}[x_i, y_j; f_{AC}]$:

$$I_{AC}[x_i, y_j; f_{AC}, \alpha] = M_{AC}[x_i, y_j; f_{AC}] \cos(2\pi f_{AC} x_i + \alpha), \tag{4.59}$$

and the DC contribution is given by the DC amplitude modulation ($I_{DC}[x_i, y_j] = M_{DC}[x_i, y_j]$). The images of the AC and DC amplitude modulation are obtained from the camera images with the following three-step demodulation method:

$$\begin{aligned} M_{AC}[x_i, y_j; f_{AC}] =& \frac{\sqrt{2}}{3} \Big\{ (I[x_i, y_j; f_{AC}, \alpha = 0] - I[x_i, y_j; f_{AC}, \alpha = 2\pi/3])^2 \\ &+ (I[x_i, y_j; f_{AC}, \alpha = 2\pi/3] - I[x_i, y_j; f_{AC}, \alpha = 4\pi/3])^2 \\ &+ (I[x_i, y_j; f_{AC}, \alpha = 4\pi/3] - I[x_i, y_j; f_{AC}, \alpha = 0])^2 \Big\}^{1/2}, \\ M_{DC}[x_i, y_j] =& M_{AC}[x_i, y_j; f_{DC} = 0] = \frac{1}{3} (I[x_i, y_j; f_{AC}, \alpha = 0] \\ &+ I[x_i, y_j; f_{AC}, \alpha = 2\pi/3] + I[x_i, y_j; f_{AC}, \alpha = 4\pi/3]) . \end{aligned} \tag{4.60}$$

The measured amplitude modulations are not only affected by the MTF of the turbid medium, but also by the optical imaging system's MTF (MTF_{OIS}), and are therefore expressed as a product of the source intensity (I_0), the MTF of the imaging system, and the MTF of the turbid medium:

$$M_{AC}[x_i, y_j; f_{AC}] = I_0 \, MTF_{OIS}[x_i, y_j; f_{AC}] \, MTF[x_i, y_j; f_{AC}]. \tag{4.61}$$

Next, a calibration step is performed to remove the contribution of the imaging system's MTF. This step consists of measuring the same three reflectance images, but from a homogeneous reference turbid media phantom with known optical properties. These images are also demodulated to obtain reference images of the amplitude modulations, $M_{AC,ref}[x_i, y_j; f_{AC}]$ and $M_{DC,ref}[x_i, y_j]$. Using a model, such as diffusion theory, the MC or HMC method, the MTF is predicted at the AC frequency ($MTF_{ref}(f_{AC})$) and the DC frequency ($MTF_{ref}(f_{DC})$). The calibration is performed as a direct division correction:

$$\begin{aligned} MTF[x_i, y_j; f_{AC}] &= \frac{M_{AC}[x_i, y_j; f_{AC}]}{M_{AC,ref}[x_i, y_j; f_{AC}]} MTF_{ref}(f_{AC}), \\ MTF[x_i, y_j; f_{DC}] &= \frac{M_{DC}[x_i, y_j]}{M_{DC,ref}[x_i, y_j]} MTF_{ref}(f_{DC}). \end{aligned} \tag{4.62}$$

This calibration avoids the need to perform deconvolution with the system's PSF in the real spatial domain (or division by the system's MTF in the spatial frequency domain) [210], and also corrects for illumination inhomogeneities.

The values of $MTF_{ref}(f_{AC})$ and $MTF_{ref}(f_{DC})$ can be calculated directly with Eq. (4.57), or with the MC or HMC model. In the former case, the inversion method (the procedure to extract μ_s' and μ_a) is usually set up as a nonlinear fitting of Eq.

(4.57) for each pixel of the retrieved images. To improve the accuracy, more than two frequencies can be used to perform a multi-frequency fitting [210]. In the latter case, the MC or HMC simulation is used to compute the reflectance PSF ($R_d[\rho_i]$) for a given set of values of optical properties. The MTF is found by Fourier transforming $R_d[\rho_i]$. Since $R_d[\rho_i]$ is radially symmetric, its two-dimensional Fourier transform is also radially symmetric and can be computed with the one-dimensional Hankel transform of zero order. The discretized version of the Hankel transform is:

$$MTF[f_j] = 2\pi \sum_i \rho_i J_0[2\pi f_j \rho_i] R_d[\rho_i] \Delta\rho. \tag{4.63}$$

where J_0 is the zero order Bessel function of the first kind. The inversion method is often implemented as an interpolation with lookup tables (LUTs) computed with a forward model like the MC (or HMC) model. This involves calculating the MTFs for a large ensemble of different values of μ_s' and μ_a. Interpolation is performed for each pixel independently. An example of such a LUT is shown in Fig. 4.7. The strong orthogonality between the absorption and scattering contour lines is due to the different sensitivity of the MTF at the low and high frequencies, and allows the optical coefficients to be accurately decoupled.

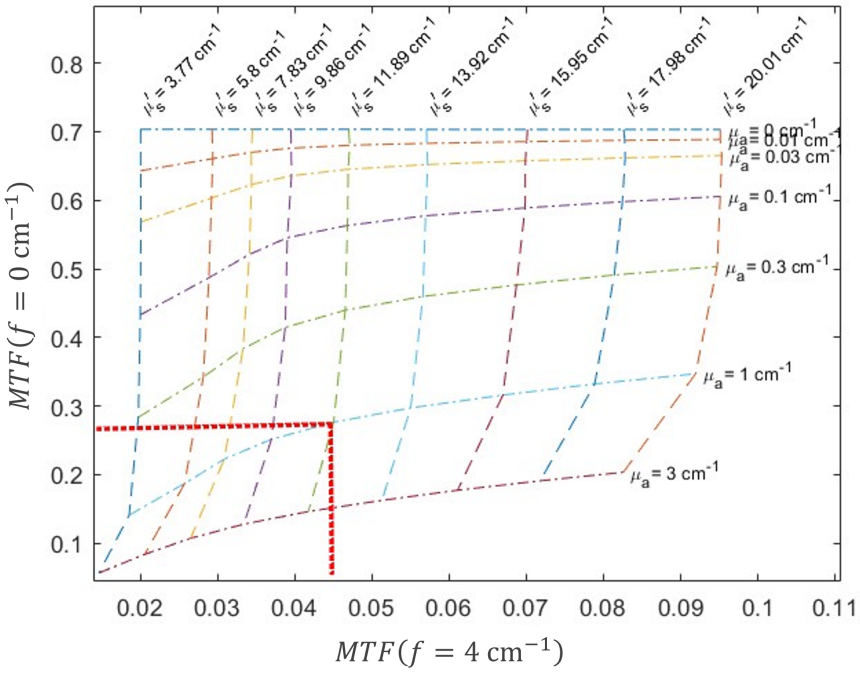

Figure 4.7: Example of a lookup table for interpolation of μ_s' and μ_a from the values of the s-MTF at two frequencies (0 and $4\,cm^{-1}$), generated from HMC model forward predictions. Dashed contour lines indicate constant μ_s', dash-dotted countour lines indicate constant μ_a, and the red dotted line shows the lookup method, which translates $MTF[f_{DC}]$ and $MTF[f_{AC}]$ values into μ_s' and μ_a coefficients. MTF values were calculated with the HMC using an average of 5 simulations, each with 10^6 photon packets. The values of the refractive index (n), anisotropy factor (g), and the critical depth (z_c) were 1.33, 0.71, and $0.5l_{tr}'$.

4.3 Imaging with the Kubelka-Munk method

The KM model does not predict spatially resolved reflectance or transmittance. In addition, the method requires the use of integrating spheres to measure those quantities. This makes imaging with conventional array-based cameras impossible. In this section we present a DOI system based on the KM model, where we use structured illumination and integrated detection for the spatial characterization of the scattering and absorption properties, i.e. μ_a, μ_s' and g, of inhomogeneous turbid media [236]. The ability to obtain images of the optical properties despite the use of integrating spheres with photodiodes as detectors is due to the use of the SPI technique, which allows imaging without the use of array detectors, and in particular to the tolerance of an active SPC to the presence of diffusers between the object to be characterized and the bucket detector [7] (as demonstrated in Ref. [237])).

The experimental setup is shown schematically in Fig. 4.8. Illumination is provided by a collimated deep red ($\lambda = 660\,\text{nm}$) LED source (M660L4, Thorlabs). This beam is structured by a DMD (V-7000, Vialux) and projected by a $4-f$ system through an integrating sphere onto the turbid media slab. The detection stage of this system consists of two integrating spheres (IS236A, Thorlabs) equipped with their respective photodiode (SM05PD1B, Thorlabs). By using a double integrating sphere arrangement with the turbid media slab sandwiched between them, we are able to measure reflectance and transmittance simultaneously. The use of integrating spheres together with the SPI technique allows us to obtain images of the spatial distributions of forward ($I_{T_d}[x_i, y_j]$) and backward scattered light ($I_{R_d}[x_i, y_j]$) at all angles, which are computationally reconstructed from the measured signals. To reconstruct absolute transmittance and reflectance images, reference measurements were made without any sample and the transmittance integrating sphere. Taking into account this reference image ($I_0[x_i, y_j]$), we can obtain absolute transmittance and reflectance maps with the operations:

$$T_d[x_i, y_j] = \frac{I_{T_d}[x_i, y_j]}{I_0[x_i, y_j]}, \quad R_d[x_i, y_j] = \frac{I_{R_d}[x_i, y_j]}{I_0[x_i, y_j]}, \tag{4.64}$$

which also corrects for any unevenness in the illumination beam. Double integrating sphere corrections for multiple light exchanges between the spheres were performed based on Eqs. (4.17).

The additional measurement of ballistic light with the collimated transmission method (see Fig. 4.5(a)) allows to reconstruct an image of collimated transmitted light ($I_{T_C}[x_i, y_i]$), which with a reference image without the sample ($I_{T_c,0}[x_i, y_j]$) allows us to calculate the map of absolute collimated transmittance:

$$T_c[x_i, y_j] = \frac{I_{T_c}[x_i, y_j]}{I_{T_c,0}[x_i, y_j]}. \tag{4.65}$$

This measurement is performed with a third photodiode (DET36A, Thorlabs) and allows the spatial distribution of the three transport parameters (μ_a, μ_s and g) to be determined pixel by pixel by performing the calculations of the KM method (see

[7] In the work described here, the diffuser between the object and the detector is not the turbid medium, but the integrating sphere, whose walls reflect light diffusely.

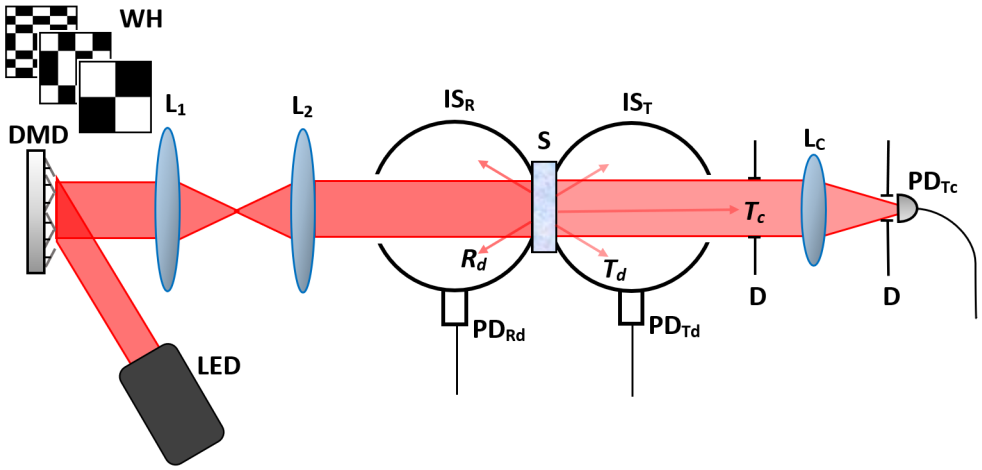

Figure 4.8: Schematic of the experimental setup for imaging the scattering and aborption properties of turbid media with integrating spheres and the Kubelka-Munk model.

Fig. 4.4). However, the acquisition of collimated transmittance limits the sample thickness to a few MFPs (depending on detector sensitivity). The signals from all three photodiodes are acquired simultaneously, amplified (PDA200C, Thorlabs) and digitized by a multichannel data acquisition system (NI6251, National Instruments). The control of the hardware (projection of the SPI patterns and data acquisition) is done with LabView software, while the computations are done with Matlab.

The patterns for imaging with the SPI technique are the Walsh-Hadamard functions of order $N = 128$, so a set of 2×16384 patterns was used (the factor 2 comes from using complementary functions). These patterns were modulated with 768×768 micromirrors of the DMD (6×6 micromirrors for each pixel of our patterns). A circular pupil was superimposed on the patterns to adjust the sampled area to a size slightly smaller than the circular apertures of the integrating spheres. This avoids artifact errors in the periphery of the measured images caused by light scattered too close to the port edges. Together with the unity magnification of the $4-f$ system, this results in a circular imaged area of about $3.5\,\mathrm{cm}^2$. For the DMD operating at 20 kHz, the acquisition time for all three images is about $1.6\,s$.

In a first set of experiments, and in order to validate the imaging system, the sample to be characterized (Fig. 4.9) is a phantom consisting of a slab of epoxy resin (diameter $\varnothing = 52.45\,\mathrm{mm}$, thickness $d = 7.55\,\mathrm{mm}$, and refractive index $n = 1.56$) as matrix material, with TiO_2 nanoparticles (titanium(IV) oxide, rutile nanopowder, $< 100\,\mathrm{nm}$, Sigma Aldrich) as a scattering agent [238, 239]. As shown in the lower part of Fig. 4.9, two inclusions were introduced into the otherwise homogeneous slab. The first one is a lower absorption and higher scattering heterogeneity, consisting of a hole of diameter 5.4 mm filled with an epoxy resin mixture with a higher concentration of nanoparticles. The second inclusion is a 1.1 mm thick fragment of an absorbing neutral density filter which was placed inside the sample serving as an absorbing object. The bulk optical properties were measured by oblique incidence reflectometry (OIR) [146, 240] and yielded values of $\mu_a \approx 0.6\,\mathrm{cm}^{-1}$ and $\mu_s' \approx 2.6\,\mathrm{cm}^{-1}$ for the background, and $\mu_a \approx 0.1\,\mathrm{cm}^{-1}$ and $\mu_s' \approx 10.5\,\mathrm{cm}^{-1}$ for the scattering inclusion.

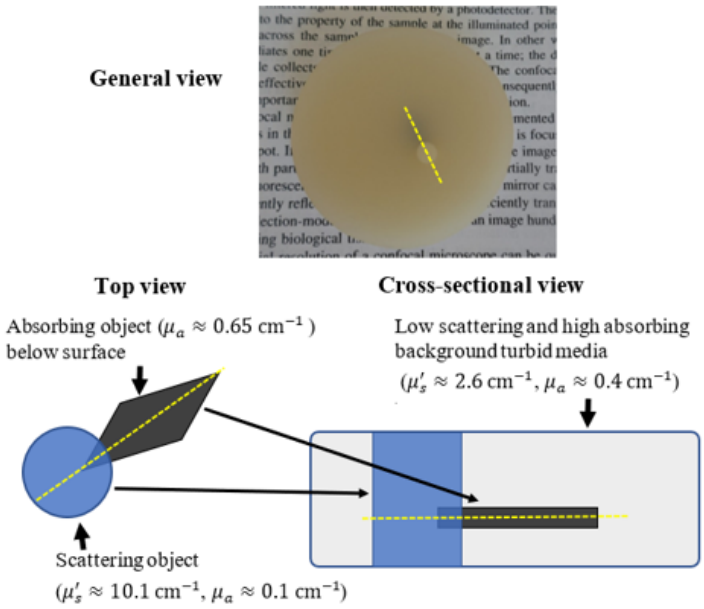

Figure 4.9: Heterogeneous turbid media phantom. (Top) Photograph of the slab and (bottom) schematic diagram of the heterogeneities of the sample. The yellow dashed line indicates the orientation of the absorption inclusion.

For this first sample, the diffuse reflectance, diffuse transmittance, and collimated transmittance images are shown in Figs. 4.10(a)-(c), respectively, while the computed maps of the corresponding reduced scattering coefficient, absorption coefficient, and scattering anisotropy are shown in Figs. 4.10(d)-(f), respectively. For this sample, the reduced scattering coefficient map is shown instead of the scattering coefficient map for better comparison with the values previously provided by OIR. For comparison with the known bulk properties, the properties of the different regions of the sample are discussed. A qualitative distinction of the absorption object can be made in the absorption coefficient map (Fig. 4.10(d)). The absorption object shows a higher absorption coefficient value ($\mu_a \approx 0.65\,\mathrm{cm}^{-1}$) in contrast to the background medium. As expected the absorbing fragment does not produce a significant variation in the scattering properties due to its thinness. For the scattering object, the average value of the reduced scattering coefficient of about $10.1\,\mathrm{cm}^{-1}$, and the absorption coefficient of about $0.09\,\mathrm{cm}^{-1}$, show good agreement with the measured OIR values. The anisotropy parameter of about 0.31 also shows that the higher nanoparticle concentration not only leads to a higher scattering coefficient, but also to a more isotropic scattering. In the background turbid medium, the absorption and scattering parameters are $\mu_a \approx 0.42\,\mathrm{cm}^{-1}$ and $\mu_s' \approx 2.2\,\mathrm{cm}^{-1}$. Note that these results reproduce the qualitative behavior, but do not match the OIR values. However, since OIR is based on the diffusion theory (which assumes $\mu_s' \gg \mu_a$), the OIR values for the background turbid medium are not expected to be completely accurate.

In a second set of experiments, we imaged a 0.85 cm thick slice of a cherry. The area imaged in Figs. 4.11(a)-(c) corresponds to the mesocarp layer, i.e., the central part of the fruit. In this layer, and due to the contrast of the optical parameters,

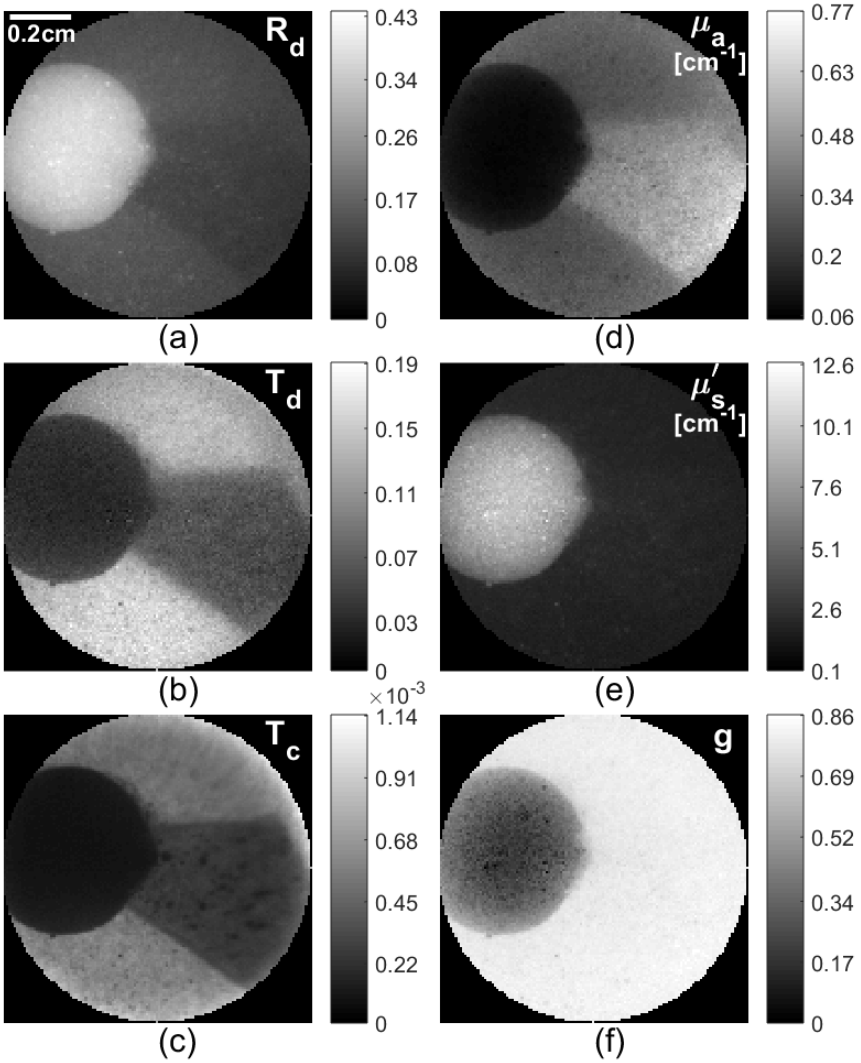

Figure 4.10: (a) Diffuse reflectance, (b) diffuse transmittance, (c) collimated transmittance, (d) absorption coefficient, (e) reduced scattering coefficient, and (f) anisotropy factor maps of the heterogeneous turbid media phantom. Each image is plotted within the minimum and maximum pixel value to highlight the spatial variations of the measured parameters.

two different tissues or parts can be distinguished. On the one hand, we have the parenchyma, which is the bulk or ground tissue of the fruit. This tissue is made of larger cells with a relatively thin cell wall. The computed optical property maps (Figs. 4.11(d)-(f)) show average values of $\mu_a \approx 0.5\,\mathrm{cm}^{-1}$, $\mu_s' \approx 7.2\,\mathrm{cm}^{-1}$, and $g \approx 0.92$ for this tissue. On the other hand, we have the vascular tissue, which is responsible for transporting fluids and nutrients to the cells of the parenchyma. This tissue has a higher scattering coefficient ($\mu_s' \approx 9.1\,\mathrm{cm}^{-1}$) and a lower absorption coefficient ($\mu_a \approx 0.26\,\mathrm{cm}^{-1}$) and anisotropy ($g \approx 0.76$).

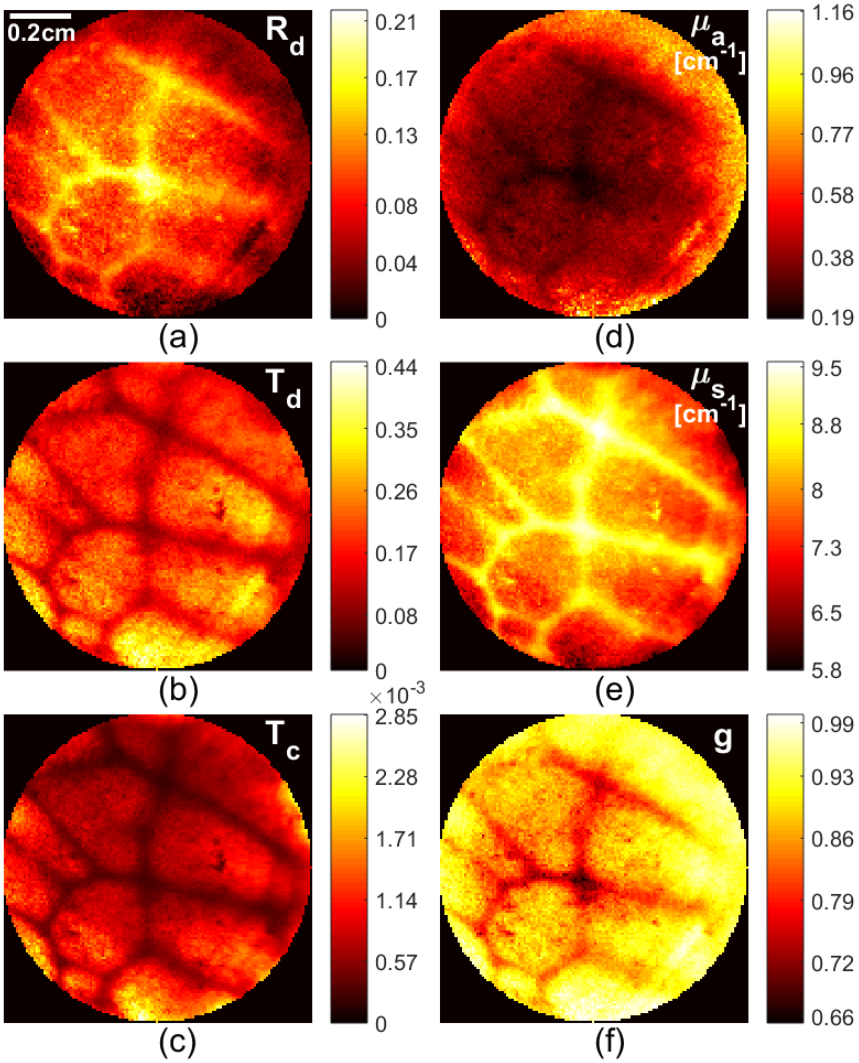

Figure 4.11: (a) Diffuse reflectance, (b) diffuse transmittance, (c) collimated transmittance, (d) absorption coefficient, (e) scattering coefficient, and (f) anisotropy factor maps for the slice of a cherry. Each image is plotted within the minimum and maximum pixel value to highlight the spatial variations of the measured parameters.

In this section we have presented a DOI system that allows us to image the scattering coefficient, absorption coefficient, and the scattering anisotropy. The imaging system uses a singe-pixel detection approach where the bucket detectors are composed by integrating spheres and photodiodes. The system in question was tested with a heterogeneous turbid media phantom, and latter used to distinguish and characterize different tissues in a slice of an organic sample (a cherry). To compute

the optical parameters we used a relatively simple light transport model, the KM model. By using this model it was not our aim to provide a completely accurate characterization, but rather to separate absorption from scattering optical properties, and to demonstrate imaging with integrating spheres. Besides, the KM provides no depth information and, therefore, the determined properties are averaged over the whole depth of the sample. Depth information could be provided via a multiple view approach. Additionally, a multispectral characterization could be performed by simply swapping the photodiodes for spectrometers.

The method based on the KM model is limited to thin samples that allow the measurement of transmitted light, and the results have limited accuracy due to the limited accuracy of the model itself. To overcome these two limitations, i.e. to measure thick samples in a reflection geometry and to perform a more accurate quantitative characterization, an SPI-based SFDI system is developed in the next section.

4.4 Single-pixel spatial frequency domain imaging

In this section we want to develop an SFDI system based on the SPI technique, i.e. the imaging function is achieved by using an DMD and a bucket detector. This would make it easy to perform multispectral imaging, use CS [241, 242], or even use time-resolved detectors to image the optical properties through measurements in both the spatial frequency and temporal domains [208,243]. In SFDI, sinusoidal light patterns are projected onto the turbid medium and the diffuse reflected light distribution is imaged with a conventional camera. The simplest way to implement SPI in SFDI is to replace the conventional camera by a structured detection SPC, i.e., to replace the camera by a DMD and a bucket detector [233, 241, 242, 244, 245]. This results in the need to use two DMDs, one for projecting the sinusoidal patterns and another for sampling the space [244, 245], or to use a single DMD in the detection stage while using a preprinted sinusoidal patterned mask in the illumination [242]. The first case results in a more complex and expensive hardware configuration. And the latter case results in a less flexible setup because the printed pattern has to be chosen in advance. While the SPI technique can be advantageous in these configurations, for example to perform multispectral imaging or to reduce measurement data by CS, a smarter idea would be to use the DMD already present in the optical system to project the sinusoidal patterns for frequency domain sampling and also to perform the base scan for SPI. This eliminates the need for a second DMD, truly reducing hardware requirements. The aim of the work explained in this section is to develop a single-pixel SFDI (SP-SFDI) system where a single DMD is used to modulate simultaneously the sinusoidal pattern for the spatial frequency sampling and the spatial sampling patterns in order to achieve spatial resolution throught the SPI technique. This simplifies detection to the point where it is simply replaced by a bucket detector.

In the case of the KM model-based imaging system, the use of integrating spheres was justified by the need to collect all diffusely reflected and transmitted light. In this case, the use of the integrating sphere as a detector was to achieve a higher NA

and therefore to detect a higher percentage of the total diffusely reflected light. This idea is illustrated in Fig. 4.12, where the percentage of total diffusely reflected light is plotted against the NA of the detection system. Detection with an integrating sphere (which ideally has NA = 1) detects 100% of the diffusely reflected light, while a detection system with NA = 0.22 would detect less than 9% of the reflected light.

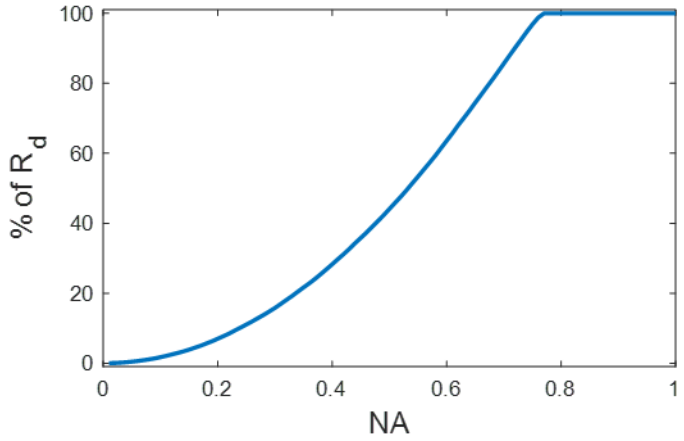

Figure 4.12: Plot of the percentage of diffuse reflected light as a function of the numerical aperture (NA) of the detection system. The total amount of diffuse reflected light and its angular distribution is computed with a MC simulation for a semi-infinite medium ($\mu_s = 100\,\mathrm{cm}^{-1}$, $\mu_a = 0.1\,\mathrm{cm}^{-1}$, $g = 0.9$, and $n = 1.3$) for 100000 photon packets. Note the saturation of the curve at NA = 0.8, which corresponds to the critical angle of total reflection of light inside the medium.

The proposed experimental system is shown schematically in Fig. 4.13. A broad beam from a collimated deep red (660 nm) LED light source (M660L4, Thorlabs) impinges onto the DMD (V-7000, Vialux). The DMD simultaneously displays the sine pattern and samples the scene with the set of sampling patterns. The spatial sampling patterns implemented on the DMD are the circular two-dimensional scrambled Walsh-Hadamard basis functions, as explained in section 2.3. The circular area of these patterns allows us to image the largest area through the circular ports of the integrating sphere. The final masks are constructed by overlapping these circular scrambled Walsh-Hadamard patterns with the binarized sinusoidal pattern. An example of these doubly modulated masks is shown in Fig. 4.14. These masks are projected through a $4-f$ unit magnification optical system onto the turbid media sample located at the exit port of an integrating sphere (IS236A, Thorlabs). A wide-core multimode fiber attached to the sphere directs the light to an avalanche photodetector (APD440A, Thorlabs), which measures the intensity signal for the set of sampling patterns.

The digital processing step consists of image reconstruction via inverse transform, demodulation, reference sample calibration, and interpolation using a LUT computed with the HMC model described in section 4.1.4. This LUT is computed with MTF values determined for a wide range of optical properties ($\mu_s' \in [1, 30]\,\mathrm{cm}^{-1}$, $\mu_a \in [0, 2]\,\mathrm{cm}^{-1}$, and $g = 0.9$), and cubic interpolation using the *griddata* method is used in Matlab to interpolate between table values.

To test absorption and scattering separability, we characterized the same het-

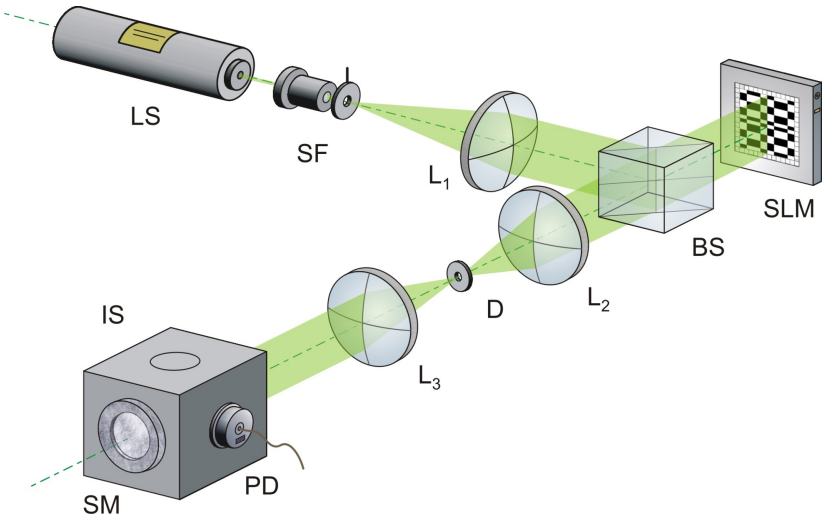

Figure 4.13: Schematic of the experimental setup of the SP-SFDI system. A light source illuminates the SLM (in this case a DMD). The SLM modulates both, the sinusoidal spatial frequency sampling pattern and the set of spatial sampling patterns. The doubly modulated light is projected by means of a $4-f$ relay system onto the sample located at the exit port of the integrating sphere. A bucket detector, like a photodiode, is attached to the integrating sphere and measures a signal proportional to the diffuse light reflected by the sample.

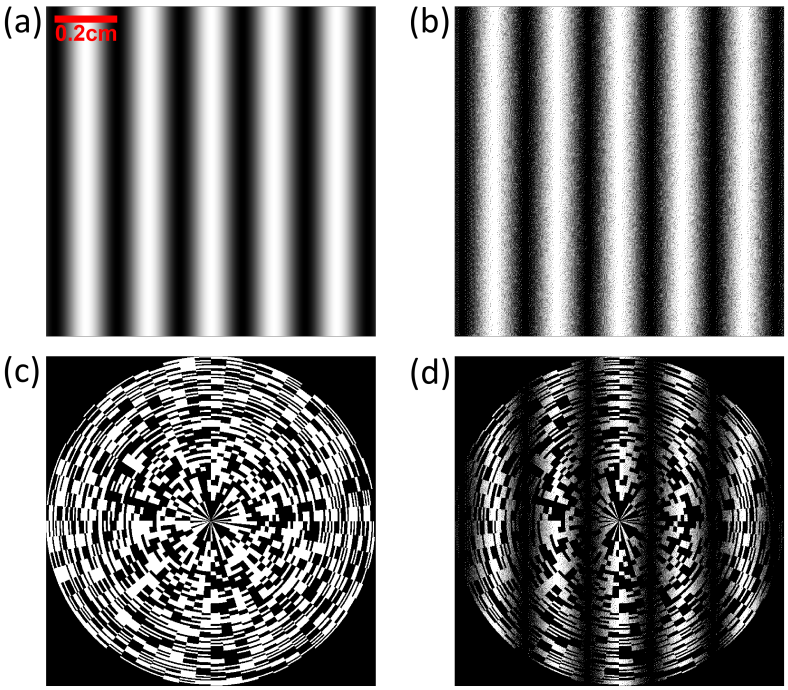

Figure 4.14: Example of the construction of a mask for our SP-SFDI system: (a) grayscale sinusoidal function of spatial frequency $f = 5\,\mathrm{cm}^{-1}$, (b) binarized version of the sinusoidal pattern by dithering based on the Floyd-Steinberg algorithm, (c) example of a scrambled and circular Walsh-Hadamard function, and (d) final mask obtained by overlaying (b) and (c).

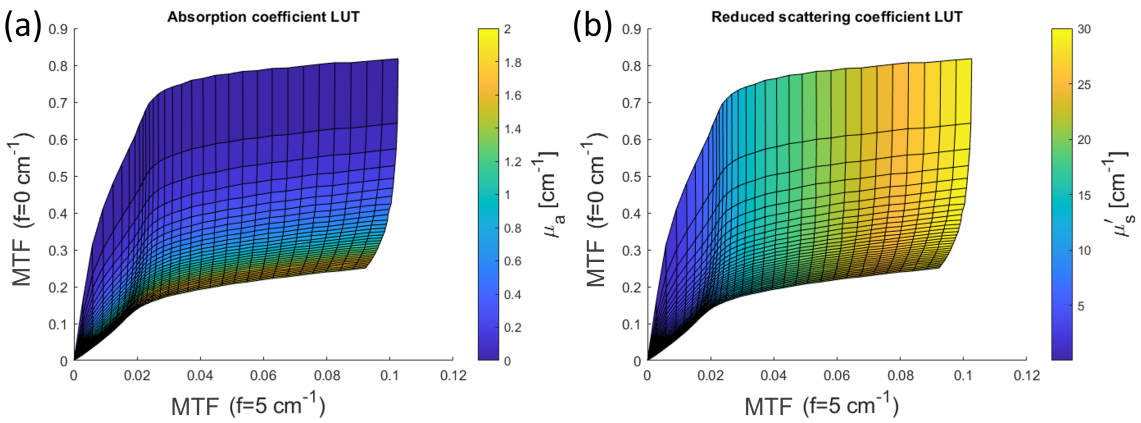

Figure 4.15: Representation as surface plots of the LUTs for interpolation of the absorption (a) and reduced scattering coefficient (b) in the SP-SFDI experiment.

erogeneous epoxy slab as in the previous section. We used the standard procedure of illuminating with only a single frequency sinusoidal pattern ($f = 5\,\mathrm{cm}^{-1}$ in this case) with three different phase offsets, and used 2×4096 scrambled circular Walsh-Hadamard patterns (again the factor 2 comes from using complementary patterns) to reconstruct images of 64×64 radial and angular section pixels of the reduced scattering and absorption coefficients. These results are shown in Fig. 4.16. The imaged area is centered on the absorption inclusion (the piece of neutral density filter). For the background, the approximate values of the absorption and reduced scattering coefficients are $0.45\,\mathrm{cm}^{-1}$ and $5\,\mathrm{cm}^{-1}$, respectively. The high scattering inclusion is characterized by $\mu_a \approx 0.1\,\mathrm{cm}^{-1}$ and $\mu_s' \approx 11\,\mathrm{cm}^{-1}$. Finally, the absorption inclusion region has the values $\mu_a \approx 0.6\,\mathrm{cm}^{-1}$ and $\mu_s' \approx 3\,\mathrm{cm}^{-1}$.

It is noticeable that the absorption map follows the same qualitative and quantitative behavior as determined with the system based on the KM model. However, the largest discrepancies are found in the scattering map. While the reduced scattering coefficient seems to be slightly overestimated in the background and in the region of the scattering inclusion, in the region of the absorption inclusion its value is much lower than the background, which differs from the characterization with the KM method. It can be argued that this effect is caused by the choice of a transport model for a semi-infinite medium for determining the LUT, while the sample being imaged is relatively thin; or by the fact that the volume occupied by the neutral density filter reduces the depth averaged value of the scattering coefficient. However, the most reasonable explanation seems to be an imperfect decoupling of the scattering coefficient from the absorption coefficient. The latter idea is supported by the fact that the reduced scattering map is similar to the absorption map but inverted, i.e. high scattering where the absorption is low and vice versa, and that this effect also occurred with other samples.

The explanation for this is that since we are not projecting a pure sinusoidal function, but its superposition with our Walsh-Hadamard functions, the physical convolution operation with the PSF of the turbid medium does not properly extract the amplitude modulation at the AC frequency (M_{AC}), while the DC amplitude modulation appears to be unaffected. Therefore, by not having the correct value of the MTF at the AC frequency, the scattering contribution is not properly decoupled

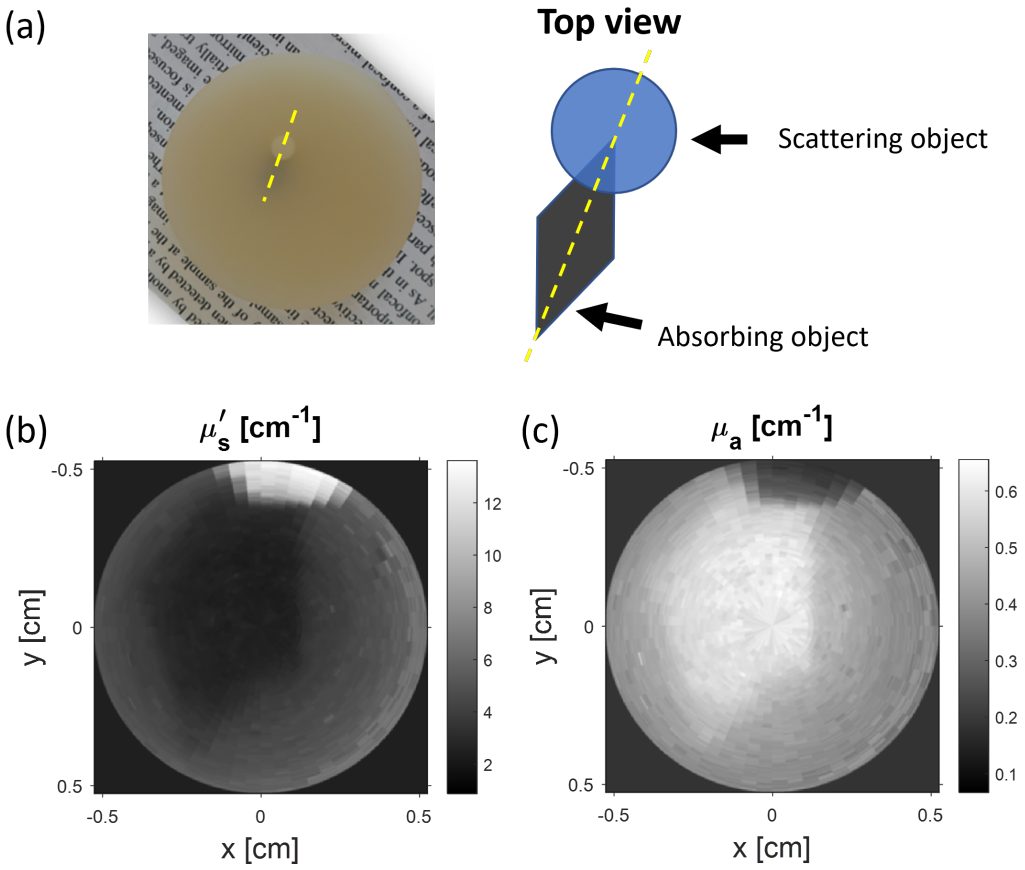

Figure 4.16: Scheme showing the orientation of the inclusions (a) and maps of the reduced scattering coefficient (b) and absorption coefficient (c) of the heterogeneous turbid media phantom obtained with the proposed SP-SFDI system.

from the absorption. This can be visualized by a horizontal line in the LUT shown in Figure 4.7. The height of this line is given by $MTF(f_{DC})$, and since $MTF(f_{AC})$ is not properly determined, it can lie anywhere along this horizontal line. Since the absorption coefficient contour lines are practically horizontal, this uncertainty in $MTF(f_{AC})$ has almost no effect on the value of the absorption coefficient. However, this uncertainty prevents the correct estimation of μ_s'. A solution to this problem has not yet been found. However, current work is devoted to finding another approach to perform DOI or SFDI with structured illumination and bucket detection. The two most promising ideas are briefly presented below.

The first idea is to exploit the rich spatial frequency information that is obtained by interrogating the turbid medium with square wave functions that exhibit many Fourier frequencies, such as the Walsh-Hadamard functions, and that is encoded in the spatially integrated intensity of the diffuse reflected light. In this sense, a set of patterns is projected onto the turbid medium and an intensity value is obtained for each one of these patterns. This set of patterns does not necessarily have to be a basis of functions. The formulation of the problem is based on the general procedure of image reconstruction in diffuse optical tomography (DOT) [146, 246]. The forward model is generated by applying a perturbation method to the time-independent diffusion equation for inhomogeneous media. Essentially, the spatially resolved optical properties ($\mu_a(\vec{r})$ and $\mu_s'(\vec{r})$, or equivalently $\mu_a(\vec{r})$ and $D(\vec{r})$), are expressed as a constant background value ($\mu_{a,0}$, and $\mu_{s,0}'$ or D_0) and a small spatially varying perturbation due to the heterogeneities relative to the background ($\delta\mu_a(\vec{r})$ and $\delta\mu_s'(\vec{r})$ or $\delta D(\vec{r})$). That is

$$\begin{aligned} \mu_a(\vec{r}) &= \mu_{a,0} + \delta\mu_a(\vec{r}), \\ \mu_s'(\vec{r}) = \mu_{s,0}' + \delta\mu_s'(\vec{r}) \quad \text{or} \quad D(\vec{r}) &= D_0 + \delta D(\vec{r}). \end{aligned} \tag{4.66}$$

Also the fluence rate can be expressed as

$$\Phi(\vec{r};\vec{r}') = \Phi_0(\vec{r};\vec{r}') + \Phi_{SC}(\vec{r};\vec{r}'), \tag{4.67}$$

where $\Phi_0(\vec{r};\vec{r}')$ represents the unperturbed fluence rate in a homogeneous medium that has the background optical properties, and $\Phi_{SC}(\vec{r};\vec{r}')$ represents the differential fluence rate due to the heterogeneities.

With the relations given by Eqs. (4.66) and (4.67) and some approximation (like the Born or Rytov approximation), the diffusion equation can be separated into two differential equations, one for the homogeneous part and another one for the perturbation. These differential equations can be solved using the Green's function method for any source function $S(\vec{r},\vec{r}')$ defined by the projected pattern. This yields the fluence rate in response to any perturbation $\delta\mu_a(\vec{r})$ and $\delta\mu_s'(\vec{r})$ or $\delta D(\vec{r})$ and constitutes the forward model. The inversion method can be implemented as minimization of the quadratic differences between the estimated fluence rates with the forward model and the measured reflectance values for the set of sampling masks using one of the gradient descent methods described in section 2.2.

The other idea is inspired by motionless optical scanning holography (MOSH) [247–249]. MOSH can be seen as a SPI technique in which the illumination patterns are Fresnel zone plates (FZPs). By measuring the integrated reflected or transmitted light from a three-dimensional object when illuminated by FZPs with different

displacements, an image or hologram of the object's convolution with the FZP is reconstructed. The object at any axial distance is obtained by deconvolution, which is equivalent to backpropagation since the FZP is equivalent to the free space propagation impulse response.

This idea can be applied to SP-SFDI by using some kind of pattern that has circular symmetry and whose convolution with the PSF of the scattering medium extracts its MTF evaluated at a single frequency. The equivalent of a single frequency sine function in polar coordinates is the zero-order Bessel function $J_0(2\pi f\rho)$[8]. Convolving $J_0(2\pi f\rho)$ with the PSF of a homogeneous medium ($PSF(\rho)$) yields a light distribution with the same modulation but with an amplitude given by the medium's MTF at frequency f, i.e., $PSF(\rho) \otimes J_0(2\pi f\rho) = MTF(f)J_0(2\pi f\rho)$.

The procedure in the MOSH-inspired SP-SFDI system consists in projecting onto the turbid medium a zero-order Bessel function modulated light pattern with a lateral displacement $\vec{\rho}'$, and to measure the integrated intensity, which is given by

$$\begin{aligned} I(\vec{\rho}') &= \int_S PSF(\rho) \otimes J_0(2\pi f\|\vec{\rho} - \vec{\rho}'\|)\, d\vec{\rho} \\ &= \int_S MTF(f) J_0(2\pi f\|\vec{\rho} - \vec{\rho}'\|)\, d\vec{\rho}. \end{aligned} \tag{4.68}$$

If we now assume that the MTF has some degree of spatial variation[9] ($MTF(f) \rightarrow MTF(\vec{\rho}; f)$), then $I(\vec{\rho}')$ can be interpreted as the image of the convolution of the MTF map and $J_0(2\pi f\rho)$, i.e.,

$$I(\vec{\rho}) = MTF(\vec{\rho}; f) \otimes J_0(2\pi f\rho). \tag{4.69}$$

Although this result seems promising, it is not very useful because the convolution with the zero-order Bessel function contains information about only one ring in the spectra of the MTF map, and a single ring in its spectra is generally not sufficient to reconstruct the image. A radial frequency sweep could possibly be the answer to sampling the whole spatial frequency space of the MTF map. Once the image of the MTF is reconstructed, the rest of the data processing follows the same steps (calibration and LUT interpolation) as in the standard SFDI procedure.

4.5 General remarks for the chapter

Two DOI systems have been described in this chapter. The first is based on a rather simple idea, which is to use the SPI technique to reconstruct images of reflectance and transmittance from integrating sphere measurements. The KM model is then used to obtain values of the three transport parameters for each pixel. Because of the transmittance measurements, this imaging system is limited to thin samples. Therefore, efforts were made to find a system in reflection geometry, resulting in the second DOI system described in this chapter. This imaging system is based on SFDI and a structured illumination SPC, rather than simply replacing the conventional camera used in standard SFDI setups with a structured detection SPC. This

[8]The two-dimensional Fourier transform of the zero-order Bessel function $J_0(2\pi f\rho)$ yields a ring in the spectra corresponding to a single radial frequency f.

[9]This is similar to the standard SFDI, which makes the theoretical assumption of a homogeneous medium, but then considers a spatially varying MTF value.

reduces the hardware requirements, since the SLM was already needed to project the sinusoidal patterns. An LUT interpolation method is used to extract the optical properties. These LUTs were calculated using a custom HMC simulation.

Both of these systems measure light with integrating spheres. In the case of the KM model-based imaging system, this is a requirement of the model, since the total diffuse reflectance and transmittance must be measured. In the case of the SP-SFDI system, the use of the integrating sphere allows a higher fraction of diffusely reflected light to be collected. Although its use converts the system to a contact method, it has the advantage of being insensitive to ambient light, since it is blocked by the integrating sphere. Possible applications of this setup could be imaging of skin lesions, moles, etc.

Although this originally proposed SP-SFDI system did not provide accurate values for the scattering coefficient map, two possible alternative solutions have been proposed. However, it is important to note that the two proposed ideas must be taken with a grain of salt, as they have not yet been experimentally verified.

Chapter 5

Conclusion

In recent years, the joint design of optical hardware and software for imaging applications, namely computational imaging, has enabled new imaging systems that are faster, cheaper, smarter, and not bound by the limitations of traditional cameras. Among these computational imaging techniques, SPI systems stand out as perfect candidates for imaging under special conditions or for obtaining multidimensional information. This is due to the simple detectors used in SPI, which make it possible to work in low-light conditions, in almost the entire electromagnetic spectrum, or to measure additional information such as spectra and time. However, this technique is not without its drawbacks, namely the sequential nature of the measurement, which creates a trade-off between acquisition speed and spatial resolution. Typically, a longer acquisition is required for relatively high-resolution images, while a faster acquisition results in low-resolution images. There are several ways to approach this problem. For example, an adaptive approach samples at high resolution only those regions of the scene where there is relevant information, CS techniques reduce the measurements (and thus the acquisition time) by playing with the sparsity and compressibility of the images in some function bases, and recently DF has also been used to increase the resolution of SPI systems by merging them with conventional high-resolution cameras. The last two are discussed and applied in several experiments in this dissertation.

Throughout this dissertation, we investigated the implementation of SPI techniques in two major biomedical imaging modalities: fluorescence imaging and DOI. The goal is to develop systems that are faster, more compact, simpler, and capable of measuring multidimensional information.

In the field of fluorescence imaging, we performed multispectral time-resolved imaging by combining different multidimensional SPCs and conventional cameras with gradient descent minimization based DF algorithms. Three contributions resulted from this idea. In the first one, two low spatial resolution (32×32 pixels) images from a multispectral (with 16 spectral channels) and a time-resolved SPC (with 256 time bins) were fused with a high resolution (512×512 pixels) CMOS camera image. The DF approach allowed to reconstruct a 4D hypercube of size $512 \times 512 \times 16 \times 256$ (512×512 pixels with 16 spectral bands and 256 time bins), which is about 8.5 Gb of data, from only about 4 Mb of the three acquired data sets combined. This gives us a measurement to reconstruction ratio of only 0.0005 (which

corresponds to a compression ratio of about 99.95%). In addition, the improvement could also be seen in terms of acquisition speed, as a SPC-only imaging system, i.e. without the conventional camera, could also provide a 512×512 pixel image, but would ultimately take 256 times longer to acquire the measurements. This system was used to image a macroscopic sample and to distinguish different fluorophores based on their spectral and temporal signature.

In the second contribution, DF was applied in a microscopy setup to merge low spatial resolution 4D datasets (of size $32 \times 32 \times 16 \times 256$) from a SPC with 256×256 pixel images from a CCD camera. Two samples were imaged with this setup: some fluorescent beads and HEK cells stained with fluorescent dye and treated with P3HT nanoparticles. SPC datasets were acquired with CS, and the results indicate that the SPC 4D dataset can be compressed up to compression ratios of $80-90\%$ without much loss in the quality of the final reconstructed hypercube with DF.

Both systems mentioned above generate very large reconstructed datasets (up to several giga-voxels). Therefore, in the last contribution on fluorescence imaging, a multi-exponential model-driven DF algorithm was developed to perform FLIM with the aforementioned experimental systems. By directly retrieving the concentrations and decay rates (or lifetimes) of the fluorophores, we were able to drastically reduce the size of the reconstructed hypercubes, instead of reconstructing all the temporal information and then performing a fit. For example, the temporal dimension of the macroscopic fluorescence imaging system sample can be described by a combination of only three different fluorophores. Thus, by directly reconstructing the lifetime images in high spatial resolution, we were able to reduce the size of the reconstructed hypercube by a factor of 36.6 compared to a $128 \times 128 \times 16 \times 256$ hypercube. We have shown that the proposed approach works well for samples such as those from the macroscopy system (with good SNR and with spatially separated fluorophores). However, the multi-exponential decay fitting does not succeed to separate the contribution of different fluorophores for microscopy samples with lower SNRs and where different fluorophores overlap spatially.

Two contributions are presented in the area of DOI. In the first one, we demonstrate for the first time imaging with integrating spheres and perform reconstruction of the three transport parameters μ_a, μ_s and g with the non-spatially resolved KM model. This system takes advantage of the ability of SPI systems to perform imaging with simple detectors, such as the integrating spheres with photodiodes. This system is useful for relatively thin samples that can be *sandwiched* between the two integrating spheres used to measure reflectance and transmittance simultaneously, and has been validated by imaging the absorption and scattering properties of turbid media phantom and a slice of an organic sample (a cherry).

To overcome the limitations of the previous system due to the accuracy of the KM model and the experimental requirement of thin samples, in the second contribution we developed a reflection geometry imaging system based on the SFDI technique. By building this system on a structured illumination SPC, we were able to simplify the optical setup by replacing the camera used in standard SFDI or the second DMD used in structured detection SPI-based SFDI systems. The detection system is simplified to the point where it is replaced by an integrating sphere with a photodiode as a bucket detector. Spatial resolution is achieved by using a single DMD to

simultaneously modulate the sine pattern for spatial frequency sampling and the spatial sampling masks for spatial resolution. Circular scrambled Walsh-Hadamard functions were used to match the circular apertures of our integrating sphere and to ensure minimal spatial frequency interference between the SPI masks and the sinusoidal pattern. This system was used to characterize the turbid media phantom slab, and the results indicate that while the spatially resolved absorption coefficient is well estimated, the reduced scattering coefficient image suffers from incomplete decoupling from the absorption image.

Beyond the work presented in this dissertation, the next few lines outline several future ideas, improvements and modifications to the fluorescence imaging systems and the SP-SFDI system.

As mentioned in section 3.6, the fusion of the different datasets could be optimized by merging datasets that do not only share the spatial dimension, but perhaps also the temporal and spectral dimension, e.g. by using RGB or few time-framed images.

While DF is applied in this work to combine 2D spatial-spectral-temporal information, the technique can be applied to any system consisting of multiple specialized cameras, and thus the addition of polarization, phase or depth information could be useful for bioimaging.

In the FLIM approach, the DF algorithm with the multi-exponential decay fitting could be refined by adding prior terms to the objective function to impose additional constraints on the solutions. Also, in the case of the noisy temporal trace of the microscopy dataset, denoising could be applied to the dataset before it is fed into the DF algorithm.

Regarding the SP-SFDI, two possible alternative solutions have been introduced: one based on sampling the scene with square wave patterns and then using a perturbation method approach to set up the inversion method, and another idea based on scanning the turbid medium with a zero order Bessel function modulated light pattern. In addition, the developed system is the first step to develop a multispectral system, which is achieved by using a spectrally resolved detector, such as a spectrometer; and to perform tomography by exploiting the penetration depth dependence on the spatial frequency of spatially modulated illumination.

Finally, seemingly unrelated, the two directions of work (fluorescence imaging and DOI) could be combined to obtain an imaging system that characterizes both the optical properties (absorption and scattering) of a sample and the signal of fluorescent markers. Such a system could be used to assess the metabolic state (oxygenation, blood oxygen saturation, hemoglobin concentration, etc.) and perfusion of a biological tissue and therefore be of great clinical interest.

Appendix A

Insights about the integration operators used in the data fusion algorithm

While the different operators ($\mathbf{S}$, $\mathbf{T}$, and $\mathbf{R}_L$) defined for our data fusion algorithm operate on different dimensions, they share a common feature: they integrate completely (or partially, in the case of the spatial downsampling operator) over a given dimension. Next, we will show some examples of these operators. For simplicity, we assume a one-dimensional image with only four entries or pixels:

$$\mathbf{x} = \begin{pmatrix} x_1 \\ x_2 \\ x_3 \\ x_4 \end{pmatrix}. \tag{A.1}$$

A spatial downsampling operator in matrix form $\mathbf{A}$, that integrates over two adjacent pixels, is written as:

$$\mathbf{A} = \begin{pmatrix} 1 & 1 & 0 & 0 \\ 0 & 0 & 1 & 1 \end{pmatrix}, \tag{A.2}$$

so that

$$\mathbf{Ax} = \begin{pmatrix} 1 & 1 & 0 & 0 \\ 0 & 0 & 1 & 1 \end{pmatrix} \begin{pmatrix} x_1 \\ x_2 \\ x_3 \\ x_4 \end{pmatrix} = \begin{pmatrix} x_1 + x_2 \\ x_3 + x_4 \end{pmatrix} \tag{A.3}$$

An operator $\mathbf{B}$, that integrates over the whole space of $\mathbf{x}$ is simply written as

$$\mathbf{B} = \begin{pmatrix} 1 & 1 & 1 & 1 \end{pmatrix}, \tag{A.4}$$

so that

$$\mathbf{Bx} = \begin{pmatrix} 1 & 1 & 1 & 1 \end{pmatrix} \begin{pmatrix} x_1 \\ x_2 \\ x_3 \\ x_4 \end{pmatrix} = x_1 + x_2 + x_3 + x_4. \tag{A.5}$$

Although they perform simple operations, these matrices become quite large and therefore computationally infeasible for the sizes of images handled in our application. For example, consider an image of 512×512 spatial pixels with no temporal or spectral dimension. To downsample this image to a 32×32 image, the downsampling matrix must have $32^2 \times 512^2$ entries.

For this reason, it is almost always better to work with functions that perform the same operations as the operator in matrix form. For example, in Matlab, the downsampling operation can be performed with the *imresize* function [250], while any of the integration operations can be performed with a sum over all elements in the specified dimension with the *sum* function [251].

Appendix B

Automatic differentiation

Automatic differentiation (AD, also called auto-differentiation, autodiff, algorithmic differentiation or computational differentiation) is a set of techniques to numerically compute the derivative or gradients of a function [252–254]. AD exploits the fact that every calculation performed by a computer, no matter how complicated, executes a sequence of elementary arithmetic operations (summation, subtraction, multiplication or division) and elementary functions (exponentials, logarithms, cosines, etc.). Therefore, derivatives of any order can be computed automatically by applying the chain rule repeatedly to these operations and functions.

It differs from symbolic differentiation and numerical differentiation (the method of finite differences) in the sense that it uses symbolic rules for differentiation (which are more accurate than finite difference approximations because they do not introduce round-off errors due to the discretization) but, unlike a purely symbolic approach, it evaluates those symbolic expressions at particular numeric values, rather than carrying out large symbolic expressions. Also, both of these classical methods (symbolic and numerical differentiation) are slow at computing derivatives of functions of many variables, which is the case for gradient-based optimization problems. Therefore it is widely used in deep learning, particularly for training deep learning models without needing to compute derivatives analytically (and especially for the case of non-differentiable or non-linear activation functions).

Appendix C

Diffusion theory contribution to the reflectance computed with the hybrid Monte Carlo method

The diffuse reflectance response to any source function $S(\vec{\rho}, z)$ in a homogeneous semi-infinite turbid medium can be computed as the convolution with the impulse response given by Eq. (4.37):

$$R_{DT}(\rho, \phi) = \int_0^{\infty} \int_0^{2\pi} \int_0^{\infty} S(\rho', \phi', z')\, R_{d,\infty/2}(\rho, \phi;\, \rho', \phi', z')\rho'\, d\rho' d\phi' dz', \qquad \text{(C.1)}$$

where cylindrical coordinates were used so that $\vec{\rho} = (\rho, \phi)$, and $d\vec{r} = d\vec{\rho}dz = \rho d\rho d\phi dz$, with ϕ being the azimuthal angle.

Since $S(\vec{\rho}, z)$ is an isotropic source distribution generated by an infinitely narrow beam normally incident at the origin of the coordinates, it has rotational symmetry about the z-axis, and thus so does $R_{DT}(\rho, \phi)$. Therefore $R_{DT}(\rho, \phi)$ can be expressed as a function of the radial variable by integrating over the entire azimuthal angle:

$$\begin{aligned} R_{DT}(\rho) &= \int_0^{2\pi} R_{DT}(\rho, \phi)\, d\phi = 2\pi R_{DT}(\rho, \phi = 0) = \\ &= \int_0^{\infty} \int_0^{\infty} S(\rho', z')\, I(\rho;\, \rho', z')\rho'\, d\rho' dz', \end{aligned} \qquad \text{(C.2)}$$

where we also took $S(\rho', \phi', z')$ out of the integral over the azimuthal angle and substituted it by its radial-only dependent function ($S(\rho, z) = 2\pi S(\rho, \phi = 0, z)$), and where we defined $I(\rho; \rho', z')$ as the following integral:

$$I(\rho; \rho', z') = \int_0^{2\pi} R_{d,\infty/2}(\rho, \phi = 0;\, \rho', \phi', z')\, d\phi', \qquad \text{(C.3)}$$

Next, we discretize Eq. (C.2) to obtain the contribution of S to diffuse reflectance computed by the hybrid Monte Carlo model:

$$R_{DT}[\rho_i] = \rho_i \Delta\rho \sum_{j,k} S[\rho'_j, z'_k]\, I[\rho_i; \rho'_j, z'_k], \qquad \text{(C.4)}$$

where we divided $S[\rho'_j, z'_k]$ by the volume element $\Delta V[\rho'_j] = 2\pi\rho'_j \Delta\rho\Delta z$ to obtain a source density function, and multiplied the entire expression by the surface area

element $\Delta S[\rho_i] = 2\pi\rho_i\Delta\rho$ to obtain absolute reflectance, rather than reflectance per unit area.

Appendix D

Deriving the MTF from the amplitude modulation of the response of a linear and translation invariant system to a sinusoidal input

Assume we have a one-dimensional system, which is linear and translation invariant, characterized by a PSF or impulse-response, $PSF(x)$. The response of this system to any input function is given by the convolution with the impulse response. The response to a sinusoidal function of frequency f is

$$F(x;f) = PSF(x) \otimes \cos(2\pi f x). \tag{D.1}$$

Next we rewrite the PSF as the inverse Fourier transform of the MTF

$$PSF(x) = \int_{-\infty}^{+\infty} MTF(u) \exp(i2\pi u x)\, du, \tag{D.2}$$

and the cosine as

$$\cos(2\pi f x) = \frac{1}{2}\left[\exp(i2\pi f x) + \exp(-i2\pi f x)\right]. \tag{D.3}$$

Substituting Eqs. (D.2) and (D.3) into Eq. (D.1) yields:

$$F(x;f) = \frac{1}{2}\left[MTF(f)\exp(i2\pi f x) + MTF(-f)\exp(-i2\pi f x)\right]. \tag{D.4}$$

Finally, as the PSF is an even function its Fourier transform will also be an even function ($MTF(-f) = MTF(f)$), and hence:

$$F(x;f) = MTF(f)\cos(2\pi f x). \tag{D.5}$$

This completes the proof that the convolution of a sinusoidal function with the PSF yields a sinusoidal response with an amplitude given by the value of the MTF evaluated at the frequency of modulation.

Appendix E

List of most used acronyms

BPAE	bovine pulmonary artery endothelial
CCD	charge-coupled device
CMOS	complementary metal-oxide-semiconductor
CR	compression ratio
CS	compressive sensing
DF	data fusion
DMD	digital micromirror device
DOI	diffuse optical imaging
DOT	diffuse optical tomography
FLIM	fluorescence lifetime imaging
FOV	field of view
FWHT	fast Walsh-Hadamard transform
HMC	hybrid Monte Carlo
KM	Kubelka-Munk
LUT	lookup table
MC	Monte Carlo
MFP	mean free path
MSE	mean squared error
MTF	modulation transfer function
OIR	oblique incidence reflectometry
PSF	point spread function
PMT	photomultiplier tube
PSNR	peak signal-to-noise ratio
ROI	region of interest
RTE	radiative transport equation
SFDI	spatial frequency domain imaging
SLM	sptail light modulator
SNR	signal-to-noise ratio
SPC	single-pixel camera
SPI	single-pixel imaging

SP-SFDI	single-pixel spatial frequency domain imaging
SVD	singular value decomposition
TCSPC	time-correlated single-photon counting
TMFP	transport mean free path
TV	total variation

Bibliography

[1] S. K. Nayar. Computational cameras: Redefining the image. *Computer*, 39:30–38, 2006.

[2] J. N. Mait, G. W. Euliss, and R. A. Athale. Computational imaging. *Advances in Optics and Photonics*, 10(2):409–483, 2018.

[3] G. Zheng, R. Horstmeyer, and C. Yang. Wide-field, high-resolution fourier ptychographic microscopy. *Nature Photonics*, 7(9):739–745, 2013.

[4] L. Tian, Z. Liu, L. H. Yeh, M. Chen, J. Zhong, and L. Waller. Computational illumination for high-speed in vitro fourier ptychographic microscopy. *Optica*, 2(10):904–911, 2015.

[5] R. Heintzmann and T. Huser. Super-resolution structured illumination microscopy. *Chemical Reviews*, 117(23):13890–13908, 2017.

[6] G. Vicidomini, P. Bianchini, and A. Diaspro. Sted super-resolved microscopy. *Nature Methods*, 15(3):173–182, 2018.

[7] Y. Park, C. Depeursinge, and G. Popescu. Quantitative phase imaging in biomedicine. *Nature Photonics*, 12(10):578–589, 2018.

[8] M. E. Gehm, R. John, D. J. Brady, R. M. Willett, and T. J. Schulz. Single-shot compressive spectral imaging with a dual-disperser architecture. *Optics Express*, 15(21):14013–14027, 2007.

[9] X. Lin, Y. Liu, J. Wu, and Q. Dai. Spatial-spectral encoded compressive hyperspectral imaging. *ACM Transactions on Graphics (TOG)*, 33(6):1–11, 2014.

[10] A. Orth, M. J. Tomaszewski, R. N. Ghosh, and E. Schonbrun. Gigapixel multispectral microscopy. *Optica*, 2(7):654–662, 2015.

[11] T. H. Tsai and D. J. Brady. Coded aperture snapshot spectral polarization imaging. *Applied Optics*, 52(10):2153–2161, 2013.

[12] P. Llull, X. Liao, X. Yuan, J. Yang, D. Kittle, L. Carin, G. Sapiro, and D. J. Brady. Coded aperture compressive temporal imaging. *Optics Express*, 21(9):10526–10545, 2013.

[13] L. Waller and L. Tian. Machine learning for 3d microscopy. *Nature*, 523(7561):416–417, 2015.

[14] L. Tian and L. Waller. 3d intensity and phase imaging from light field measurements in an led array microscope. *Optica*, 2(2):104–111, 2015.

[15] A. Levin, R. Fergus, F. Durand, and W. T. Freeman. Image and depth from a conventional camera with a coded aperture. *ACM Transactions on Graphics (TOG)*, 26(3):70–es, 2007.

[16] R. Prevedel, Y. G. Yoon, M. Hoffmann, N. Pak, G. Wetzstein, S. Kato, T. Schrödel, R. Raskar, M. Zimmer, E. S. Boyden, et al. Simultaneous whole-animal 3d imaging of neuronal activity using light-field microscopy. *Nature Methods*, 11(7):727–730, 2014.

[17] E. Berrocal, S. G. Pettersson, and E. Kristensson. High-contrast imaging through scattering media using structured illumination and fourier filtering. *Optics Letters*, 41(23):5612–5615, 2016.

[18] J. Bertolotti, E. G. Van Putten, C. Blum, A. Lagendijk, W. L. Vos, and A. P. Mosk. Non-invasive imaging through opaque scattering layers. *Nature*, 491(7423):232–234, 2012.

[19] S. Gigan. Optical microscopy aims deep. *Nature Photonics*, 11(1):14–16, 2017.

[20] A. P. Mosk, A. Langendijk, G. Lerosey, and M. Fink. Controlling waves in space and time for imaging and focusing in complex media. *Nature Photonics*, 6(1):283–292, 2012.

[21] D. Faccio, A. Velten, and G. Wetzstein. Non-line-of-sight imaging. *Nature Reviews Physics*, 2(6):318–327, 2020.

[22] V. Boominathan, J. T. Robinson, L. Waller, and A. Veeraraghavan. Recent advances in lensless imaging. *Optica*, 9(1):1–16, 2022.

[23] N. Antipa, G. Kuo, R. Heckel, B. Mildenhall, E. Bostan, R. Ng, and L. Waller. Diffusercam: lensless single-exposure 3d imaging. *Optica*, 5(1):1–9, 2018.

[24] I. Robinson and R. Harder. Coherent x-ray diffraction imaging of strain at the nanoscale. *Nature Materials*, 8(4):291–298, 2009.

[25] M. P. Edgar, G. M. Gibson, R. W. Bowman, B. Sun, N. Radwell, K. J. Mitchell, S. S. Welsh, and M. J. Padgett. Simultaneous real-time visible and infrared video with single-pixel detectors. *Scientific Reports*, 5(10669):2998–3005, 2015.

[26] G. M. Gibson, B. Sun, M. P. Edgar, D. B. Phillips, N. Hempler, G. T. Maker, G. P. A. Malcolm, and M. J. Padgett. Real-time imaging of methane gas leaks using a single-pixel camera. *Optics Express*, 25(4):2998–3005, 2017.

[27] A. Buades, B. Coll, and J. Morel. A review of image denoising algorithms, with a new one. *Multiscale Modeling and Simulation: A SIAM Interdisciplinary Journal*, 2(4):490–530, 2005.

[28] L. Fan, F. Zhang, H. Fan, and C. Zhang. Brief review of image denoising techniques. *Visual Computing for Industry, Biomedicine, and Art*, 2(7):1–12, 2019.

[29] Computational photography: From selfies to black holes. https://vas3k.com/blog/computational_photography/index.html. Accessed: 2023-05-30.

[30] A. Neumaier. Solving ill-conditioned and singular linear systems: A tutorial on regularization. *SIAM Review*, 40(3):636–666, 1998.

[31] S. Boyd and L. Vandenberghe. *Convex Optimisation*. Cambridge University Press, 2004.

[32] M. Bertero and M. Boccacci. *Introduction to Inverse Problems in Imaging*. IOP Publishing Ltd, 1998.

[33] C. R. Vogel. *Computational Methods for Inverse Problems*. SIAM, 2002.

[34] E. K. P. Chong and S. H. Zak. *An Introduction to Optimization*. John Wiley & Sons, 2011.

[35] B. T. Polyak. *Introduction to Optimization*. Optimization Software, 1987.

[36] S. R. Arridge. Optimisation and inverse problems in imaging. http://www0.cs.ucl.ac.uk/staff/s.arridge/teaching/optimisation/GV08_notes.pdf, April 2023. Accessed: 2023-05-31.

[37] P. Wolfe. Convergence conditions for ascent methods. *SIAM Review*, 11(2):226–235, 1969.

[38] P. Wolfe. Convergence conditions for ascent methods. ii: Some corrections. *SIAM Review*, 13(2):185–188, 1971.

[39] S. Yang. Descent method. steepest descent and conjugate gradient. https://towardsdatascience.com/descent-method-steepest-descent-and-conjugate-gradient-math-explained-78601d8df3ce. Accessed: 2023-05-31.

[40] S. Ruder. An overview of gradient descent optimization algorithms. https://www.ruder.io/optimizing-gradient-descent/. Accessed: 2023-05-31.

[41] S. Ruder. An overview of gradient descent optimization algorithms, 2017. arXiv:1609.04747v2.

[42] N. Qian. On the momentum term in gradient descent learning algorithms. *Neural Networks*, 12(1):145–151, 1999.

[43] R. Bhat. Gradient descent with momentum. https://towardsdatascience.com/gradient-descent-with-momentum-59420f626c8f. Accessed: 2023-05-31.

[44] Y. Nesterov. A method for solving the convex programming problem with convergence rate $\mathcal{O}(1/k^2)$. *Dokl. Akad. Nauk. SSSR (translated as Soviet. Math. Docl.)*, 269:543–547, 1983.

[45] M. R. Hestenes and E. Stiefel. Methods of conjugate gradients for solving linear systems. *Journal of Research of the National Bureau of Standards*, 49(6):409–436, 1952.

[46] J. R. Shewchuk. An introduction to the conjugate gradient method without the agonizing pain. https://www.cs.cmu.edu/~quake-papers/painless-conjugate-gradient.pdf, 1994. Accessed: 2023-05-31.

[47] R. Fletcher and C. M. Reeves. Function minimization by conjugate gradients. *The Computer Journal*, 7(2):149–154, 1964.

[48] E. Polak and G. Ribière. Note sur la convergence de méthodes de directions conjuguées. *Revue Française d'Automatique, Informatique, Recherche Opérationnelle*, 3(1):35–43, 1969.

[49] K. Levenberg. A method for the solution of certain non-linear problems in least squares. *Quarterly of Applied Mathematics*, 2(2):164–168, 1944.

[50] D. Marquardt. An algorithm for least-squares estimation of nonlinear parameters. *SIAM Journal on Applied Mathematics*, 11(2):431–441, 1963.

[51] A. N. Tikhonov. On the solution of ill-posed problems and the method of regularization. *Doklady Akademii Nauk SSSR*, 151(3):501–504, 1963.

[52] A. Oppermann. Regularization in deep learning — l1, l2, and dropout. https://towardsdatascience.com/regularization-in-deep-learning-l1-l2-and-dropout-377e75acc036. Accessed: 2023-06-05.

[53] Gradient of the tv norm of an image. https://math.stackexchange.com/questions/1612017/gradient-of-the-tv-norm-of-an-image. Accessed: 2023-06-26.

[54] E. Y. Sidky, C. M. Kao, and X. Pan. Accurate image reconstruction from few-views and limited-angle data in divergent-beam ct, 2009. arXiv:0904.4495.

[55] S. Boyd, L. Xiao, and A. Mutapcic. Subgradient methods. https://web.stanford.edu/class/ee392o/subgrad_method.pdf, October 2003. Accessed: 2023-06-05.

[56] A. Beck and M. Teboulle. A fast iterative shrinkage-thresholding algorithm for linear inverse problems. *SIAM Journal on Imaging Sciences*, 2(1):183–202, 2009.

[57] S. Boyd, N. Parikh, E. Chu, B. Peleato, and J. Eckstein. Distributed optimization and statistical learning via the alternating direction method of multipliers. *Foundations and Trends in Machine Learning*, 3(1):1–122, 2010.

[58] N. Parikh and S. Boyd. Proximal algorithms. *Foundations and Trends in Optimization*, 1(3):123–231, 2013.

[59] I. Daubechies, M. Defrise, and C. De Mol. An iterative thresholding algorithm for linear inverse problem with a sparsity constraint. *Comm. Pure Appl. Math.*, 57(11):1413—-1457, 2004.

[60] M. P. Edgar, G. M. Gibson, and M. J. Padgett. Principles and prospects for single-pixel imaging. *Nature Photonics*, 13:13–20, 2019.

[61] G. M. Gibson, S. D. Johnson, and M. J. Padgett. Single-pixel imaging 12 years on: a review. *Optics Express*, 28(19):28190–28208, 2020.

[62] C. Scotté, F. Galland, and H. Rigneault. Photon-noise: is a single-pixel camera better than point scanning? a signal-to-noise ratio analysis for hadamard and cosine positive modulation. *Journal of Physics: Photonics*, 5(3):035003, 2023.

[63] Y. YJauregui-Sánchez, P. Clemente, P. Latorre-Carmona, E. Tajahuerce, and J. Lancis. Signal-to-noise ratio of single-pixel cameras based on photodiodes. *Applied Optics*, 57(7):B67–B73, 2018.

[64] ViALUX GmbH. *ALP-4.3 Controller Suite: Application Programming Interface*, September 2019.

[65] Boston Micromachines Corporation. *Hex Class Deformable Mirrors*, June 2023. `https://bostonmicromachines.com/wp-content/uploads/2023/Sell%20Sheets/Hex_Class-DM_2023.pdf`.

[66] F. Soldevila, E. Salvador-Balaguer, P. Clemente, E. Tajahuerce, and L. Lancis. High-resolution adaptive imaging with a single photodiode. *Scientific Reports*, 5(14300):1–9, 2015.

[67] D. B. Phillips, M. J. Sun, J. M. Taylor, M. P. Edgar, S. M. Barnett, G. M. Gibson, and M. J. Padgett. Adaptive foveated single-pixel imaging with dynamic supersampling. *Science Advances*, 3(4):e1601782, 2017.

[68] N. Radwell, K. J. Mitchell, G. M. Gibson, M. P. Edgar, R. Bowman, and M. J. Padgett. Single-pixel infrared and visible microscope. *Optica*, 1(5):285–289, 2014.

[69] J. Zhang, Q. Wang, J. Dai, and W. Cai. Demonstration of a cost-effective single-pixel uv camera for flame chemiluminescence imaging. *Applied Optics*, 58(19):5248–5256, 2019.

[70] R. H. Dicke. Scatter-hole cameras for x-rays and gamma rays. *The Astrophysical Journal*, 153:L101, 1968.

[71] J. Greenberg, K. Krishnamurthy, and D. Brady. Compressive single-pixel snapshot x-ray diffraction imaging. *Optics Letters*, 39(1):111–114, 2014.

[72] S. Chen. X-ray ghost images could cut radiation doses. *Science*, 359(6383):1452–1452, 2018.

[73] A. Schori and S. Shwartz. X-ray ghost imaging with a laboratory source. *Optics Express*, 25(13):14822–14828, 2017.

[74] S. Li, F. Cropp, K. Kabra, T. J. Lane, G. Wetzstein, P. Musumeci, and D. Ratner. Electron ghost imaging. *Physical Review Letters*, 121(11):114801, 2018.

[75] A. M. Kingston, G. R. Myers, D. Pelliccia, F. Salvemini, J. J. Bevitt, U. Garbe, and D. M. Paganin. Neutron ghost imaging. *Physical Review A*, 101(5):053844, 2020.

[76] Y. H. He, Y. Y. Huang, Z. R. Zeng, Y. F. Li, J. H. Tan, L. M. Chen, L. A. Wu, M. F. Li, B. G. Quan, S. L. Wang, et al. Single-pixel imaging with neutrons. *Science Bulletin*, 66(2):133–138, 2021.

[77] W. L. Chan, K. Charan, D. Takhar, K. F. Kelly, R. G. Baraniuk, and D. M. Mittleman. A single-pixel terahertz imaging system based on compressed sensing. *Applied Physics Letters*, 93(12):121105, 2008.

[78] C. Li, J. Grant, J. Wang, and D. R. S. Cumming. A nipkow disk integrated with fresnel lenses for terahertz single pixel imaging. *Optics Express*, 21(21):24452–24459, 2013.

[79] C. M. Watts, D. Shrekenhamer, J. Montoya, G. Lipworth, J. Hunt, T. Sleasman, S. Krishna, D. R. Smith, and W. J. Padilla. Terahertz compressive imaging with metamaterial spatial light modulators. *Nature Photonics*, 8(8):605–609, 2014.

[80] P. A. Morris, R. S. Aspden, J. E. C. Bell, R. W. Boyd, and M. J. Padgett. Imaging with a small number of photons. *Nature Communications*, 6(5913):1–6, 2015.

[81] B. Lochocki, A. Gambín, S. Manzanera, E. Irles, E. Tajahuerce, J. Lancis, and P. Artal. Single pixel camera ophthalmoscope. *Optica*, 3(10):1056–1059, 2016.

[82] Z. Li, J. Suo, X. Hu, C. Deng, J. Fan, and Q. Dai. Efficient single-pixel multispectral imaging via non-mechanical spatio-spectral modulation. *Scientific Reports*, 7(1):41435, 2017.

[83] F. Rousset, N. Ducros, F. Peyrin, G. Valentini, C. D'andrea, and A. Farina. Time-resolved multispectral imaging based on an adaptive single-pixel camera. *Optics Express*, 26(8):10550–10558, 2018.

[84] V. Kravets, P. Kondrashov, and A. Stern. Compressive ultraspectral imaging using multiscale structured illumination. *Applied Optics*, 58(22):F32–F39, 2019.

[85] F. Soldevila, E. Irles, V. Durán, P. Clemente, M. Fernández-Alonso, E. Tajahuerce, and J. Lancis. Single-pixel polarimetric imaging spectrometer by compressive sensing. *Applied Physics B*, 113:551–558, 2013.

[86] Z. Zhang, S. Liu, J. Peng, M. Yao, G. Zheng, and J. Zhong. Simultaneous spatial, spectral, and 3d compressive imaging via efficient fourier single-pixel measurements. *Optica*, 5(3):315–319, 2018.

[87] K. Shibuya, T. Minamikawa, Y. Mizutani, H. Yamamoto, K. Minoshima, T. Yasui, and T. Iwata. Scan-less hyperspectral dual-comb single-pixel-imaging in both amplitude and phase. *Optics Express*, 25(18):21947–21957, 2017.

[88] V. Durán, P. Clemente, M. Fernández-Alonso, E. Tajahuerce, and J. Lancis. Single-pixel polarimetric imaging. *Optics Letters*, 37(5):824–826, 2012.

[89] S. S. Welsh, M. P. Edgar, R. Bowman, B. Sun, and M. J. Padgett. Near video-rate linear stokes imaging with single-pixel detectors. *Journal of Optics*, 17(2):025705, 2015.

[90] E. Salvador-Balaguer, P. Clemente, E. Tajahuerce, F. Pla, and J. Lancis. Full-color stereoscopic imaging with a single-pixel photodetector. *Journal of Display Technology*, 12(4):417–422, 2015.

[91] E. Salvador-Balaguer, P. Latorre-Carmona, C. Chabert, F. Pla, J. Lancis, and E. Tajahuerce. Low-cost single-pixel 3d imaging by using an led array. *Optics Express*, 26(12):15623–15631, 2018.

[92] L. Martínez-León, P. Clemente, Y. Mori, V. Climent, J. Lancis, and E. Tajahuerce. Single-pixel digital holography with phase-encoded illumination. *Optics Express*, 25(5):4975–4984, 2017.

[93] H. González, L. Martínez-León, F. Soldevila, M. Araiza-Esquivel, J. Lancis, and E. Tajahuerce. High sampling rate single-pixel digital holography system employing a dmd and phase-encoded patterns. *Optics Express*, 26(16):20342–20350, 2018.

[94] F. Soldevila, V. Durán, P. Clemente, J. Lancis, and E. Tajahuerce. Phase imaging by spatial wavefront sampling. *Optica*, 5(2):164–174, 2018.

[95] H. González, L. Martínez-León, F. Soldevila, M. Araiza-Esquivel, J. Lancis, and E. Tajahuerce. High sampling rate single-pixel digital holography system employing a dmd and phase-encoded patterns. *Optics Express*, 26(16):20342–20350, 2018.

[96] S. Augustin, T. Szollmann, P. Jung, and H. Wilhelm. Huebers. Breaking imaging limits using dithering masks in 0.35 terahertz single-pixel imaging, 2017. arXiv:1711.02995.

[97] Z. Zhang, X. Wang, G. Zheng, and J. Zhong. Fast fourier single-pixel imaging via binary illumination. *Scientific Reports*, 7(1):12029, 2017.

[98] M. F. Duarte, M. A. Davenport, D. Takhar, J. N. Laska, T. Sun, K. F. Kelly, and R. G. Baraniuk. Single-pixel imaging via compressive sampling. *IEEE Signal Processing Magazine*, 25(2):83–91, 2008.

[99] You. A. Geadah and M. J. G. Corinthios. Natural, dyadic, and sequency order algorithms and processors for the walsh-hadamard transform. *IEEE Transactions on Computers*, 26(05):435–442, 1977.

[100] F. Soldevila, P. Clemente, E. Tajahuerce, N. Uribe-Patarroyo, P. Andrés, and J. Lancis. Computational imaging with a balanced detector. *Scientific Reports*, 6(29181):1–10, 2016.

[101] L. Wang and Y. Feng. "compressed sensing of hyperspectral images based on scrambled block hadamard ensemble. *Journal of Electronic Imaging*, 25(6):063021–1–9, 2016.

[102] B. Rauer, H. B. de Aguiar, L. Bourdieu, and S. Gigan. Scattering correcting wavefront shaping for three-photon microscopy. *Optics Letters*, 47(23):6233–6236, 2022.

[103] G. Wang, H. Deng, M. Ma, and X. Zhong. Polar coordinate fourier single-pixel imaging. *Optics Letters*, 48(3):743–746, 2023.

[104] A. J. M. Lenz, P. Clemente, V. Climent, J. Lancis, and E. Tajahuerce. Spatial frequency domain imaging with a bucket detector. In *Tissue Optics and Photonics II*, volume 12147, page 121470A. International Society for Optics and Photonics, SPIE, 2022.

[105] C. M. Gómez-Sarabia, L. Ledesma-Carrillo, and J. Ojeda-Castañeda. Reducing field depth: annular hadamard masks. *Applied Optics*, 59(22):6632–6637, 2020.

[106] L. Ledesma-Carrillo, C. M. Gómez-Sarabia, M. Torres-Cisneros, R. Guzmán-Cabrera, C. Guzmán-Cano, and J. Ojeda-Castañeda. Hadamard circular masks: high focal depth with high throughput. *Optics Express*, 25(15):17004–17020, 2017.

[107] E. J Candes, J. K. Romberg, and T. Tao. Stable signal recovery from incomplete and inaccurate measurements. *Communications on Pure and Applied Mathematics*, 59(8):1207–1223, 2006.

[108] D. L. Donoho. Compressed sensing. *IEEE Transactions on Information Theory*, 52(4):1289–1306, 2006.

[109] R. G. Baraniuk. Compressive sensing [lecture notes]. *IEEE Signal Processing Magazine*, 24(4):118–121, 2007.

[110] Emmanuel J Candès and Michael B Wakin. An introduction to compressive sampling. *IEEE Signal Processing Magazine*, 25(2):21–30, 2008.

[111] R. Aravind, G. L. Cash, and J. P. Worth. On implementing the jpeg still-picture compression algorithm. In *Visual Communications and Image Processing IV*, volume 1199, pages 799–809. SPIE, 1989.

[112] E. J. Candes and T. Tao. Near-optimal signal recovery from random projections: Universal encoding strategies? *IEEE Transactions on Information Theory*, 52(12):5406–5425, 2006.

[113] E. J. Candes and J. Romberg. Sparsity and incoherence in compressive sampling. *Inverse Problems*, 23(3):969, 2007.

[114] R. T. Rockafellar. *Convex Analysis*. Princeton University Press, 1970.

[115] S. Becker, J. Bobin, and E. J. Candès. Nesta: A fast and accurate first-order method for sparse recovery. *SIAM Journal Imaging Sciences*, 4:1–39, 2009.

[116] J. Romberg. Imaging via compressive sampling. *IEEE Signal Processing Magazine*, 25(2):14–20, 2008.

[117] M. A. T. Figueiredo, R. D. Nowak, and S. J. Wright. Gradient projection for sparse reconstruction: Application to compressed sensing and other inverse problems. *IEEE Journal of Selected Topics in Signal Processing*, 1(4):586–597, 2007.

[118] E. van den Berg and M. P. Friedlander. Probing the pareto frontier for basis pursuit solutions. *SIAM Journal on Scientific Computing*, 31(2):890–912, 2008.

[119] E. van den Berg and M. P. Friedlander. SPGL1: A solver for large-scale sparse reconstruction. `https://friedlander.io/spgl1`, December 2019. Accessed: 2023-06-20.

[120] E. Candès and J. Romberg. l1-magic: Recovery of sparse signals via convex programming. https://candes.su.domains/software/l1magic/downloads/l1magic.pdf, October 2005. Accessed: 2023-06-20.

[121] l1-magic. https://candes.su.domains/software/l1magic/downloads/l1magic.pdf. Accessed: 2023-06-20.

[122] C. Li, W. Yin, H. Jiang, and Y. Zhang. An efficient augmented lagrangian method with applications to total variation minimization. *Computational Optimization and Applications*, 56:507–530, 2013.

[123] S. Becker. Nesta. a fast and accurate first-order method for sparse recovery. https://candes.su.domains/software/nesta/, June 2011. Accessed: 2023-06-20.

[124] Y. Sher. Review of algorithms for compressive sensing of images, 2019. arXiv:1908.01642.

[125] Y. Nesterov. Smooth minimization of non-smooth functions. *Mathematical Programming*, 103:127–152, 2005.

[126] D. L. Hall and J. Llinas. An introduction to multisensor data fusion. *Proceedings of the IEEE*, 85(1):6–23, 1997.

[127] B. Khaleghi, A. Khamis, F. O. Karray, and S. N. Razavi. Multisensor data fusion: A review of the state-of-the-art. *Information Fusion*, 14(1):28–44, 2013.

[128] Z. Omar and T. Stathaki. Image fusion: An overview. In *2014 5th International Conference on Intelligent Systems, Modelling and Simulation*, pages 306–310. IEEE, 2014.

[129] R. S. Blum, Z. Xue, and Z. Zhang. An overview of image fusion. *Multi-Sensor Image Fusion and Its Applications*, pages 1–36, 2018.

[130] Y. Zhang. Understanding image fusion. *Photogrammetric Engineering and Remote Sensing*, 70(6):657–661, 2004.

[131] J. Zhang. Multi-source remote sensing data fusion: status and trends. *International Journal of Image and Data Fusion*, 1(1):5–24, 2010.

[132] C. Pohl and J. Van Genderen. *Remote sensing image fusion: A practical guide*. Crc Press, 2016.

[133] P. Ghamisi, B. Rasti, N. Yokoya, Q. Wang, B. Hofle, L. Bruzzone, F. Bovolo, M. Chi, K. Anders, R. Gloaguen, et al. Multisource and multitemporal data fusion in remote sensing: A comprehensive review of the state of the art. *IEEE Geoscience and Remote Sensing Magazine*, 7(1):6–39, 2019.

[134] A. P. James and B. V. Dasarathy. Medical image fusion: A survey of the state of the art. *Information Fusion*, 19:4–19, 2014.

[135] M. J. Gooding, K. Rajpoot, S. Mitchell, P. Chamberlain, S. H. Kennedy, and J. A. Noble. Investigation into the fusion of multiple 4-d fetal echocardiography images to improve image quality. *Ultrasound in Medicine & Biology*, 36(6):957–966, 2010.

[136] J. B. A. Maintz and M. A. Viergever. A survey of medical image registration. *Medical Image Analysis*, 2(1):1–36, 1998.

[137] J. Du, W. Li, K. Lu, and B. Xiao. An overview of multi-modal medical image fusion. *Neurocomputing*, 215:3–20, 2016.

[138] M. L. Kessler. Image registration and data fusion in radiation therapy. *The British Journal of Radiology*, 79(1):S99–S108, 2006.

[139] C. Smith. Two microscopes are better than one. *Nature*, 492:293–297, 2012.

[140] R. Van de Plas, J. Yang, J. Spraggins, and R. M. Caprioli. Image fusion of mass spectrometry and microscopy: a multimodality paradigm for molecular tissue mapping. *Nature Methods*, 12(4):366–372, 2015.

[141] V. Joshi, N. Rajamani, T. Katsuki, N. Prathapaneni, and L. V. Subramaniam. Information fusion based learning for frugal traffic state sensing. In *Twenty-Third International Joint Conference on Artificial Intelligence*, 2013.

[142] R. Sander. A practical dive into data fusion for self-driving cars. `https://towardsdatascience.com/a-practical-dive-into-data-fusion-for-self-driving-cars-7af71949133d`. Accessed: 2023-06-22.

[143] M. Crider. Why do some smartphones use multiple cameras? `https://www.howtogeek.com/349408/why-do-some-smartphones-use-multiple-cameras/`. Accessed: 2023-06-22.

[144] S. Ral. Sensor fusion for l3 and beyond. `https://www.pathpartnertech.com/sensor-fusion-for-l3-and-beyond/`. Accessed: 2023-06-22.

[145] V. V. Tuchin. *Tissue Optics: Light Scattering Methods and Instruments for Medical Diagnostics*. SPIE Press, 2015.

[146] L. V. Wang and H. I. Wu. *Biomedical Optics: Principles and Imaging*. John Wiley & Sons, 2012.

[147] J. R. Lorenzo. *Principles of diffuse light propagation: light propagation in tissues with applications in biology and medicine*. World Scientific, 2012.

[148] J. R. Lakowics. *Principles of Fluorescence Spectroscopy*. Kluwer Academic/-Plenum, 1999.

[149] H. Qian, M. E. Cousins, E. H. Horak, A. Wakefield, M. D. Liptak, and I. Aprahamian. Suppression of kasha's rule as a mechanism for fluorescent molecular rotors and aggregation-induced emission. *Nature Chemistry*, 9(1):83–87, 2017.

[150] J. R. Lakowicz. *Principles of fluorescence spectroscopy*. Springer, 2006.

[151] C. Donate-Buendia, R. Torres-Mendieta, A. Pyatenko, E. Falomir, M. Fernandez-Alonso, and G. Mínguez-Vega. Fabrication by laser irradiation in a continuous flow jet of carbon quantum dots for fluorescence imaging. *ACS Omega*, 3(3):2735–2742, 2018.

[152] D. Lapotko, E. Lukianova, M. Potapnev, O. Aleinikova, and A. Oraevsky. Method of laser activated nano-thermolysis for elimination of tumor cells. *Cancer Letters*, 239(1):36–45, 2006.

[153] R Ackroyd, C. Kelty, N. Brown, and M. Reed. The history of photodetection and photodynamic therapy. *Photochemistry and Photobiology*, 74(5):656–669, 2001.

[154] V. V. Tuchin. *Handbook of photonics for biomedical science*. CRC Press, 2010.

[155] B. Valeur and M. N. Berberan-Santos. *Molecular fluorescence: principles and applications*. John Wiley & Sons, 2012.

[156] X. Liu, D. Lin, W. Becker, J. Niu, B. Yu, L. Liu, and J. Qu. Fast fluorescence lifetime imaging techniques: A review on challenge and development. *Journal of Innovative Optical Health Sciences*, 12(05):1930003, 2019.

[157] A. Grinvald and I. Z. Steinberg. On the analysis of fluorescence decay kinetics by the method of least-squares. *Analytical Biochemistry*, 59(2):583–598, 1974.

[158] D. R. James and W. R. Ware. A fallacy in the interpretation of fluorescence decay parameters. *Chemical Physics Letters*, 120(4-5):455–459, 1985.

[159] P. J. Verveer, A. Squire, and P. I. H. Bastiaens. Global analysis of fluorescence lifetime imaging microscopy data. *Biophysical Journal*, 78(4):2127–2137, 2000.

[160] J. R. Lakowicz and B. P. Maliwal. Construction and performance of a variable-frequency phase-modulation fluorometer. *Biophysical Chemistry*, 21(1):61–78, 1985.

[161] E. Gratton and M. Limkeman. A continuously variable frequency cross-correlation phase fluorometer with picosecond resolution. *Biophysical Journal*, 44(3):315–324, 1983.

[162] J. Philip and K. Carlsson. Theoretical investigation of the signal-to-noise ratio in fluorescence lifetime imaging. *Journal of the Optical Society of America A*, 20(2):368–379, 2003.

[163] S. P. Chan, Z. J. Fuller, J. N. Demas, and B. A. DeGraff. Optimized gating scheme for rapid lifetime determinations of single-exponential luminescence lifetimes. *Analytical Chemistry*, 73(18):4486–4490, 2001.

[164] P. N. Prasad. *Introduction to biophotonics*. John Wiley & Sons, 2004.

[165] R. M. Ballew and J. N. Demas. Error analysis of the rapid lifetime determination method for single exponential decays with a non-zero baseline. *Analytica Chimica Acta*, 245:121–127, 1991.

[166] K. K. Sharman, A. Periasamy, H. Ashworth, and J. N. Demas. Error analysis of the rapid lifetime determination method for double-exponential decays and new windowing schemes. *Analytical Chemistry*, 71(5):947–952, 1999.

[167] T. W. J. Gadella. *FRET and FLIM techniques*. Elsevier, 2011.

[168] W. Becker. *Advanced time-correlated single photon counting techniques*. Springer, 2005.

[169] E. P. Buurman, R. Sanders, A. Draaijer, H. C. Gerritsen, J. J. F. Van Veen, P. M. Houpt, and Y. K. Levine. Fluorescence lifetime imaging using a confocal laser scanning microscope. *Scanning*, 14(3):155–159, 1992.

[170] Guide to streak cameras. https://www.hamamatsu.com/content/dam/hamamatsu-photonics/sites/documents/99_SALES_LIBRARY/sys/SHSS0006E_STREAK.pdf. Accessed: 2023-08-25.

[171] C. Bruschini, H. Homulle, I. M. Antolovic, S. Burri, and E. Charbon. Single-photon avalanche diode imagers in biophotonics: review and outlook. *Light: Science & Applications*, 8(87), 2019.

[172] J. A. Richardson, L. A. Grant, and R. K. Henderson. Low dark count single-photon avalanche diode structure compatible with standard nanometer scale cmos technology. *IEEE Photonics Technology Letters*, 21(14):1020–1022, 2009.

[173] R. K. Henderson, N. Johnston, H. Chen, D. D. U. Li, G. Hungerford, R. Hirsch, D. McLoskey, P. Yip, and D. J. S. Birch. A 192×128 time correlated single photon counting imager in 40nm cmos technology. In *ESSCIRC 2018 - IEEE 44th European Solid State Circuits Conference (ESSCIRC)*, pages 54–57, 2018.

[174] C. Callenberg, A. Lyons, D. Brok, A. Fatima, A. Turpin, V. Zickus, L. Machesky, J. Whitelaw, D. Faccio, and M. B. Hullin. Super-resolution time-resolved imaging using computational sensor fusion. *Scientific Reports*, 11(1):1689, 2021.

[175] Q. Pian, R. Yao, N. Sinsuebphon, and X. Intes. Compressive hyperspectral time-resolved wide-field fluorescence lifetime imaging. *Nature Photonics*, 11(7):411–414, 2017.

[176] C. T. Rueden and K. W. Eliceiri. Visualization approaches for multidimensional biological image data. *BioTechniques*, 43(S1):S31–S36, 2007.

[177] F. Soldevila, A. J. M. Lenz, A. Ghezzi, A. Farina, C. D'Andrea, and E. Tajahuerce. Giga-voxel multidimensional fluorescence imaging combining single-pixel detection and data fusion. *Optics Letters*, 46(17):4312–4315, 2021.

[178] A. Ghezzi, A. J. M. Lenz, F. Soldevila, E. Tajahuerce, V. Vurro, A. Bassi, G. Valentini, A. Farina, and C. D'Andrea. Computational based time-resolved multispectral fluorescence microscopy. *APL Photonics*, 8(4), 2023.

[179] A. Fatima, J. Whitelaw, V. Zickus, E. McGhee, R. Insall, L. Machesky, A. Turpin, and D. Faccio. Enhanced-resolution fluorescence lifetime imaging from multiple sensor data fusion. page CW1B.3, 2020.

[180] F. Soldevila, A. Lenz, A. Ghezzi, A. Farina, C. D'Andrea, and E. Tajahuerce. Single-pixel based data fusion algorithm for spectral-temporal-spatial reconstruction. https://github.com/cbasedlf/SinglePixelDataFusion4D. Accessed: 2023-08-26.

[181] Matlab: Image registration. https://www.mathworks.com/discovery/image-registration.html. Accessed: 2023-11-19.

[182] F. Soldevila, A. Lenz, A. Ghezzi, A. Farina, C. D'Andrea, and E. Tajahuerce. Data fusion recovery. https://opticapublishing.figshare.com/articles/media/Data_fusion_recovery/14778216. Accessed: 2023-08-26.

[183] F. Benfenati and G. Lanzani. Clinical translation of nanoparticles for neural stimulation. *Nature Reviews Materials*, 6(1):1–4, 2021.

[184] H. Altug, S.H. Oh, S. A Maier, and J. Homola. Advances and applications of nanophotonic biosensors. *Nature Nanotechnology*, 17(1):5–16, 2022.

[185] A. C. Anselmo and Sa. Mitragotri. Nanoparticles in the clinic. *Bioengineering & Translational Medicine*, 1(1):10–29, 2016.

[186] K. M. Mullen and I. H. M. Stokkum. The variable projection algorithm in time-resolved spectroscopy, microscopy and mass spectrometry applications. *Numerical Algorithms*, 51:319–340, 2009.

[187] D. P. O'Leary and B. W. Rust. Variable projection for nonlinear least squares problems. *Computational Optimization and Applications*, 54:579–593, 2013.

[188] A. Volpato, L. Bolzonello, E. Meneghin, and E. Collini. Global analysis of coherence and population dynamics in 2d electronic spectroscopy. *Optics Express*, 24(21):24773–24785, 2016.

[189] F. Martelli, B. Tiziano, S. Del Bianco, L. André, K. Alwin, et al. Light propagation through biological tissue and other diffusive media: Theory, solutions, and validations. SPIE, 2022.

[190] L. C. Henyey and J. L. Greenstein. Diffuse radiation in the galaxy. *The Astrophysical Journal*, 93:70–83, 1940.

[191] C. Dunsby and P. M. W. French. Techniques for depth-resolved imaging through turbid media including coherence-gated imaging. *Journal of Physics D: Applied Physics*, 36(14):207–227, 2003.

[192] S. A. Prahl. *The Adding-Doubling Method*, pages 101–129. 1995.

[193] J. H. Joseph, W. J. Wiscombe, and J. A. Weinman. The delta-eddington approximation for radiative flux transfer. *Journal of Atmospheric Sciences*, 33(12):2452–2459, 1976.

[194] P. Kubelka and F. Munk. Ein beitrag zur optik der farbanstriche. *Zeitschrift für Technische Physik*, 12:593–601, 1931.

[195] P. Kubelka. New contributions to the optics of intensely light-scattering materials. part i. *Journal of the Optical Society of America*, 38(5):448–457, 1948.

[196] P. Kubelka. New contributions to the optics of intensely light-scattering materials. part ii: Nonhomogeneous layers. *Journal of the Optical Society of America*, 44(4):330–335, 1954.

[197] V. Džimbeg-Malčić, Ž. Barbarić-Mikočević, and K. Itrić. Kubelka-Munk theory in describing optical properties of paper (I). *Technical Gazette*, 18(I):117–124, 2011.

[198] V. Džimbeg-Malčić, Ž. Barbarić-Mikočević, and K. Itrić. Kubelka-Munk theory in describing optical properties of paper (II). *Technical Gazette*, 19(1):191–196, 2012.

[199] A Roy, R. Ramasubramaniam, and H. A. Gaonkar. Empirical relationship between kubelka–munk and radiative transfer coefficients for extracting optical parameters of tissues in diffusive and nondiffusive regimes. *Journal of Biomedical Optics*, 17(11):115006–115006, 2012.

[200] L. F. Gate. Comparison of the photon diffusion model and kubelka-munk equation with the exact solution of the radiative transport equation. *Applied Optics*, 13(2):236–238, 1974.

[201] B. J. Brinkworth. Interpretation of the kubelka-munk coefficients in reflection theory. *Applied Optics*, 11(6):1434–1435, 1972.

[202] K Klier. Absorption and scattering in plane parallel turbid media. *Journal Optical Society of America*, 62(7):882–885, 1972.

[203] M. J. C. van Gemert, S. L. Jacques, H. J. C. M. Sterenborg, and W. M. Star. Skin optics. *IEEE Transactions on Biomedical Engineering*, 36:1146–1154, 1989.

[204] W. F. Cheong, S. A. Prahl, and A. J. Welch. A review of the optical properties of biological tissues. *IEEE Journal of Quantum Electronics*, 26(12):2166–2185, 1990.

[205] M. H. Niemz. *Laser-tissue interactions. Fundamentals and Applications*, volume 322. Springer, 2007.

[206] J. W. Pickering, C. J. M. Moes, H. J. C. M. Sterenborg, S. A. Prahl, and M. J. C. van Gemert. Two integrating spheres with an intervening scattering sample. *Journal of the Optical Society of America A*, 9(4):621–631, 1992.

[207] D. A. Boas, D. H. Brooks, E. L. Miller, C. A. DiMarzio, M. Kilmer, R. J. Gaudette, and Q. Zhang. Imaging the body with diffuse optical tomography. *IEEE Signal Processing Magazine*, 18(6):57–75, 2001.

[208] T. D. O'Sullivan, A. E. Cerussi, D. J. Cuccia, and B. J. Tromberg. Diffuse optical imaging using spatially and temporally modulated light. *Journal of Biomedical Optics*, 17(7):071311–071311, 2012.

[209] R. Watté, N. N. Do Trong, B. Aernouts, C. Erkinbaev, J. De Baerdemaeker, B. Nicolaï, and W. Saeys. Metamodeling approach for efficient estimation of optical properties of turbid media from spatially resolved diffuse reflectance measurements. *Optics Express*, 21(26):32630–32642, 2013.

[210] D. J. Cuccia, F. Bevilacqua, A. J. Durkin, F. R. Ayers, and B. J. Tromberg. Quantitation and mapping of tissue optical properties using modulated imaging. *Journal of Biomedical Optics*, 14(2):024012–024012, 2009.

[211] I. Lux and L. Koblinger. *Particle Transport Methods: Neutron and Photon Calculations*. CRC Press, 1991.

[212] V. Ntziachristos. Going deeper than microscopy: the optical imaging frontier in biology. *Nature Methods*, 7(8):603–614, 2010.

[213] R. Splinter. *Handbook of Physics in Medicine and Biology*. CRC Press, 2010.

[214] R. Weissleder and M. J. Pittet. Imaging in the era of molecular oncology. *Nature*, 452:580–589, 2008.

[215] L. Wang, P. P. Ho, C. Liu, G. Zhang, and R. R. Alfano. Ballistic 2-d imaging through scattering walls using an ultrafast optical kerr gate. *Science*, 253(5021):769–771, 1991.

[216] Y. Jauregui-Sánchez, P. Clemente, J.s Lancis, and E. Tajahuerce. Single-pixel imaging with fourier filtering: application to vision through scattering media. *Optics Letters*, 44(3):679–682, 2019.

[217] N. K. Soni, R. V. Vinu, and R. K. Singh. Polarization modulation for imaging behind the scattering medium. *Optics Letters*, 41(5):906–909, 2016.

[218] MP Rowe, EN Pugh, J Scott Tyo, and N Engheta. Polarization-difference imaging: a biologically inspired technique for observation through scattering media. *Optics Letters*, 20(6):608–610, 1995.

[219] E. Leith, C. Chen, H. Chen, Y. Chen, D. Dilworth, J. Lopez, J. Rudd, P. C. Sun, J. Valdmanis, and G. Vossler. Imaging through scattering media with holography. *Journal of the Optical Society of America A*, 9(7):1148–1153, 1992.

[220] M. Gu. *Principles of three dimensional imaging in confocal microscopes*. World Scientific, 1996.

[221] W. Denk, J. H. Strickler, and W. W. Webb. Two-photon laser scanning fluorescence microscopy. *Science*, 248(4951):73–76, 1990.

[222] S. M. Popoff, G. Lerosey, R. Carminati, M. Fink, A. C. Boccara, and S. Gigan. Measuring the transmission matrix in optics: An approach to the study and control of light propagation in disordered media. *Physical Review Letters*, 104:100601, 2010.

[223] I. M. Vellekoop and A. P. Mosk. Focusing coherent light through opaque strongly scattering media. *Optics Letters*, 32(16):2309–2311, 2007.

[224] Z. Yaqoob, D. Psaltis, M. S. Feld, and C. Yang. Optical phase conjugation for turbidity suppression in biological samples. *Nature Photonics*, 2(2):110–115, 2008.

[225] A. P. Gibson, J. C. Hebden, and S. R. Arridge. Recent advances in diffuse optical imaging. *Physics in Medicine & Biology*, 50(4):1–43, 2005.

[226] T. Durduran, R. Choe, W. B. Baker, and A. G. Yodh. Diffuse optics for tissue monitoring and tomography. *Reports on Progress in Physics*, 73(7):076701, 2010.

[227] A. Gibson and H. Dehghani. Diffuse optical imaging. *Philosophical Transactions of the Royal Society A: Mathematical, Physical and Engineering Sciences*, 367(1900):3055–3072, 2009.

[228] Prerana, R. S. Mangalpady, and P. P. Bishnu. Method to determine the optical properties of turbid media. *Applied Optics*, 47(17):3216–3220, 2008.

[229] S. Gioux, A. Mazhar, and D. J. Cuccia. Spatial frequency domain imaging in 2019: principles, applications, and perspectives. *Journal of Biomedical Optics*, 24(7):071613–071613, 2019.

[230] I. Nissilä, T. Noponen, J. Heino, T. Kajava, and T. Katila. Diffuse optical imaging. *Advances in Electromagnetic Fields in Living Systems*, pages 77–129, 2005.

[231] T. J. Farrell, M. S. Patterson, and B. Wilson. A diffusion theory model of spatially resolved, steady-state diffuse reflectance for the noninvasive determination of tissue optical properties in vivo. *Medical Physics*, 19(4):879–888, 1992.

[232] R. F. Bonner, R. Nossal, S. Havlin, and G. H. Weiss. Model for photon migration in turbid biological media. *Journal of the Optical Society of America A*, 4(3):423–432, 1987.

[233] J. P. Angelo, S. J. Chen, M. Ochoa, U. Sunar, S. Gioux, and X. Intes. Review of structured light in diffuse optical imaging. *Journal of Biomedical Optics*, 24(7):071602–071602, 2019.

[234] D. J. Cuccia, F. Bevilacqua, A. J. Durkin, and B. J. Tromberg. Modulated imaging: quantitative analysis and tomography of turbid media in the spatial-frequency domain. *Optics Letters*, 30(11):1354–1356, 2005.

[235] L. O. Svaasand, T. Spott, J. B. Fishkin, T. H. Pham, B. J. Tromberg, and M. W. Berns. Reflectance measurements of layered media with diffuse photon-density waves: a potential tool for evaluating deep burns and subcutaneous lesions. *Physics in Medicine & Biology*, 44:801 – 813, 1999.

[236] A. J. M. Lenz, P. Clemente, V. Climent, J. Lancis, and E. Tajahuerce. Imaging the optical properties of turbid media with single-pixel detection based on the kubelka–munk model. *Optics Letters*, 44(19):4797–4800, 2019.

[237] E. Tajahuerce, V. Durán, P. Clemente, E. Irles, F. Soldevila, P. Andrés, and J. Lancis. Image transmission through dynamic scattering media by single-pixel photodetection. *Optics Express*, 22(14):16945–16955, 2014.

[238] Y. auregui Sánchez, A. J. M. Lenz, P. Clemente, J. Lancis, and E. Tajahuerce. Vision through turbid media by fourier filtering and single-pixel detection. In *Unconventional Optical Imaging*, volume 10677, page 1067715. SPIE, 2018.

[239] Scott Prahl. Optical phantoms. `https://omlc.org/classroom/phantom/`. Accessed: 2023-11-22.

[240] S. P. Lin, L. Wang, S. L. Jacques, and F. K. Tittel. Measurement of tissue optical properties by the use of oblique-incidence optical fiber reflectometry. *Applied Optics*, 36(1):136–143, 1997.

[241] B. O. L. Mellors, A. Bentley, A. M. Spear, C. R. Howle, and H. Dehghani. Applications of compressive sensing in spatial frequency domain imaging. *Journal of Biomedical Optics*, 25(11):112904–112904, 2020.

[242] M. Torabzadeh, I. Y. Park, R. A. Bartels, A. J. Durkin, and B. J. Tromberg. Compressed single pixel imaging in the spatial frequency domain. *Journal of Biomedical Optics*, 22(3):030501–030501, 2017.

[243] A. Bassi, C. D'Andrea, G. Valentini, R. Cubeddu, and S. Arridge. Temporal propagation of spatial information in turbid media. *Optics Letters*, 33(23):2836–2838, 2008.

[244] S. Bélanger, M. Abran, X. Intes, C. Casanova, and F. Lesage. Real-time diffuse optical tomography based on structured illumination. *Journal of Biomedical Optics*, 15(1):016006–016006, 2010.

[245] E. Aguénounon, F. Dadouche, W. Uhring, N. Ducros, and S. Gioux. Single snapshot imaging of optical properties using a single-pixel camera: a simulation study. *Journal of Biomedical Optics*, 24(7):071612–071612, 2019.

[246] S. R. Arridge. Optical tomography in medical imaging. *Inverse Problems*, 15(2):R41, 1999.

[247] N. Yoneda, Y. Saita, and T. Nomura. Motionless optical scanning holography. *Optics Letters*, 45(12):3184–3187, 2020.

[248] N. Yoneda, Y. Saita, and T. Nomura. Three-dimensional fluorescence imaging through dynamic scattering media by motionless optical scanning holography. *Applied Physics Letters*, 119(16), 2021.

[249] N. Yoneda, O. Matoba, Y. Saita, and T. Nomura. Quantitative phase imaging based on motionless optical scanning holography. *Optics Letters*, 48(20):5273–5276, 2023.

[250] Matlab function: imresize - resize image. `https://www.mathworks.com/help/matlab/ref/imresize.html`. Accessed: 2023-11-18.

[251] Matlab function: sum - sum of array elements. `https://www.mathworks.com/help/matlab/ref/sum.html`. Accessed: 2023-11-18.

[252] A. G. Baydin, B. A. Pearlmutter, A. A. Radul, and J. M. Siskind. Automatic differentiation in machine learning: a survey. *Journal of Marchine Learning Research*, 18:1–43, 2018.

[253] R. D. Neidinger. Introduction to automatic differentiation and matlab object-oriented programming. *SIAM Review*, 52(3):545–563, 2010.

[254] Automatic differentiation background. `https://www.mathworks.com/help/deeplearning/ug/deep-learning-with-automatic-differentiation-in-matlab.html`. Accessed: 2023-11-23.